



Renan de Melo Correia Lima

**Effect of the microstructure on the
mechanical properties of a
Complex-Phase (CP) Advanced
High Strength Steel (AHSS)**

Tese de Doutorado

Thesis presented to the Programa de Pós-Graduação em Engenharia de Materiais e de Processos Químicos e Metalúrgicos da PUC-Rio in partial fulfillment of the requirements for the degree of Doutor em Ciências - Engenharia Química e de Materiais.

Advisor: Prof. Fernando Cosme Rizzo Assunção
Co-Advisor: Amy J. Clarke

Rio de Janeiro
August 2021



Renan de Melo Correia Lima

**Effect of the microstructure on the
mechanical properties of a
Complex-Phase (CP) Advanced
High Strength Steel (AHSS)**

Thesis presented to the Programa de Pós-Graduação em Engenharia de Materiais e de Processos Químicos e Metalúrgicos da PUC-Rio in partial fulfillment of the requirements for the degree of Doutor em Ciências - Engenharia Química e de Materiais. Approved by the Examination Committee:

Prof. Fernando Cosme Rizzo Assunção

Advisor

Departamento de Engenharia Química e de Materiais – PUC-RIO

Prof^a. Amy J. Clarke

Co-Advisor

Metallurgical And Materials Engineering – Colorado School of Mines

Prof. André Luiz Vasconcellos da Costa e Silva

Departamento de Engenharia Metalúrgica – UFF-Volta Redonda

Prof^a. Andersan dos Santos Paula

Departamento de Engenharia de Materiais - SE8 - IME

Prof^a. Amanda Lemette Teixeira Brandão

Departamento de Engenharia de Materiais – PUC-RIO

Prof. Sidnei Paciornik

Departamento de Engenharia de Materiais – PUC-RIO

Todos os direitos reservados. É proibida a reprodução total ou parcial do trabalho sem a autorização da universidade, da autora e do orientador.

Renan de Melo Correia Lima

Formado em Tecnologia em Construção Naval no Centro Universitário Estadual da Zona Oeste (UEZO) em 2014. Fez Mestrado em Ciência dos Materiais no Instituto Militar de Engenharia (IME) em 2017. Trabalhou no desenvolvimento de aços avançados de alta resistência da classe complex-phase em parceria com a companhia siderúrgica nacional (CSN) entre 2018 e 2021. Parte da pesquisa sendo conduzida na Colorado School of Mines entre 2019 e 2020.

Ficha Catalográfica

Lima, Renan de Melo Correia

Effect of the microstructure on the mechanical properties of a Complex-Phase (CP) Advanced High Strength Steel (AHSS) / Renan de Melo Correia Lima ; advisor: Fernando Cosme Rizzo Assunção. – 2021.

174 f. : il. color. ; 30 cm

Tese (doutorado)–Pontifícia Universidade Católica do Rio de Janeiro, Departamento de Engenharia Química e de Materiais, 2021.

Inclui bibliografia

CDD: 620.11

To my parents and professors, for
their trust in myself, sometimes higher
than mine

Acknowledgements

During the more than 4 years this thesis took to be written, help has come from several sides. Therefore, it is hard to appropriately thank everyone involved. Here, I want to express my thanks:

First to my advisor, Professor Fernando Rizzo, for all the help and patience that he gave me during this research, including times when the orientation needed to be repeated several times. His guidance made me a better researcher.

My international advisors Professors Amy Clarke and Kester Clarke, who received me at MINES, opened their laboratories and helped me take important decisions and analyze the data.

The CSN's Researcher Flávia Tolomelli, who brought me the problem to study, the theme to develop, and the solution to present. Without her and CSN, this thesis could neither begin, much less finish.

To Pos-doc Julio Spadotto, for his constant help on electron microscopy analysis, especially during the pandemic.

To PUC-Rio DEQM faculty, staff, and students. They taught and helped me, from the basic aspects of materials engineering, to advanced concepts of image processing and machine learning. Any e-mail I have sent had a positive reply; no question went unanswered. Professor Sidnei Paciornik gave a lot of orientations for the image analyses. Professor Omar Pandoli, for all the AFM characterization. To Carmem Façanha, whose help was essential during CAPES-PrInt process. To Valter Rocha, Marcia Pradanoff, Yuri Santos, Isabel Ramos, Antonio Costa, among others.

To Colorado School of Mines faculty, staff, and students especially to Professor John Speer, Karen Abt, Jonah Klemm-Toole, Nelson Delfino, Larissa Costa, Ricardo Gomes, among others.

The INT researchers Robson, and Gerson, for their help and support during the microstructural characterization and hardness measurements.

To Professor Hélio Goldenstein, and his Pos-doc Dany Centeno, for allowing me to use their dilatometer, which was essential for my thesis.

At IME, my thanks to Gabriel Onofre, and Talita Gama, both who helped me during EBSD and X Ray diffraction analyses. To Professor Leila Rosa, who encouraged me to go to PUC for a Ph.D.

To the research centers that had their doors open for me: The Centro Brasileiro de Pesquisas Físicas (CBPF); Instituto Nacional de Tecnologia (INT); Instituto Militar de Engenharia (IME); Universidade de São Paulo (USP); and Colorado School of Mines (MINES).

The CAPES-Print Program that founded my stay in the Colorado School of Mines.

This study was financed in part by the Advanced Steel Processing and Products Research Center (ASPPRC), during my stay at MINES.

This study was financed in part by the Coordenação de Aperfeiçoamento de Pessoal de Nível Superior - Brasil (CAPES) - Finance Code 001;

This study was financed in part by the Conselho Nacional de Desenvolvimento Científico e Tecnológico (CNPq);

This study was financed in part by the Fundação de Amparo à Pesquisa do Estado do Rio de Janeiro (FAPERJ).

Finally, to my family and friends. They were with me, during the good, and the bad moments.

Abstract

Lima, Renan de Melo Correia; Rizzo, Fernando Cosme (Advisor). **Effect of the microstructure on the mechanical properties of a Complex-Phase (CP) Advanced High Strength Steel (AHSS)**. Rio de Janeiro, 2021. Tese de Doutorado – Departamento de Engenharia Química de Materiais e Processos Metalúrgicos, Pontifícia Universidade Católica do Rio de Janeiro.

The demand for safer and fuel-efficient vehicles leads the automotive industry to seek new and stronger materials. The steel industry, threatened by the aluminum competition, reacted with new and higher strength steels. Among the possible steels, the Advanced High Strength Steels (AHSS) can be highlighted. These steels can be divided into 3 generations, each one possessing advantages and challenges. The first generation includes more economical alloying and processing strategies, usually with a ferritic/martensitic microstructure. The second generation contains the more expensive, higher alloyed ferritic/austenitic stainless steels, using TWinning Induced Plasticity (TWIP). Between these two classes, a third generation is growing, based on more inexpensive compositions but with more complex processing, such as Quenching and Partitioning (Q&P). There is not only a single path to success, because of that, all three generations receive their fair amount of attention and research. Trying to fulfill part of the industry demand, the Companhia Siderúrgica Nacional (CSN) is conducting research on the first generation of AHSS steels. Among the first generation steels, Dual-Phase (DP) are the most used. However, DP steels present some problems, such as void nucleation during deformation, which is a limiting factor on their mechanical properties. Therefore, their replacement by Complex-Phase (CP) steels, with higher bainite amounts, and less prone to void nucleation, is welcome. The complex phase steels processing involves a sequence of hot-rolling and cold rolling steps, followed by a heat treatment. In the present thesis, the production of a CP1200 steel in an

industrial hot dip galvanizing line was studied. The starting point was an industrial CP1100 steel. Samples of this cold rolled steel were analyzed by quenching dilatometry to obtain the CCT curve. Using the dilatometric data, a new heat treatment was proposed and done at CSN facilities, successfully producing a CP 1200 steel. Tension, hardness, bending and hole expansion tests were performed to measure the mechanical properties of the new steel. The microstructural characterization was done using light optical microscopy (LOM), scanning electron microscopy (SEM), atomic force microscopy (AFM), electron backscattering diffraction (EBSD) and transmission electron microscopy (TEM); neural networks and digital image processing were used to quantify the obtained micrographs. The increase in tension and yielding strengths was explained based on the higher amounts of bainite as well as of bainite-ferrite and bainite-martensite interfaces, found to be less prone to void nucleation.

Keywords

AHSS; Complex-Phase Steel; CP1200; Phase Transformation; Microstructural Characterization.

Resumo

Lima, Renan de Melo Correia; Rizzo, Fernando Cosme (Orientador). **Efeito da microestrutura nas propriedades mecânicas de um aço avançado de alta resistência (AHSS) da classe Complex-Phase (CP)**. Rio de Janeiro, 2021. Tese de Doutorado – Departamento de Engenharia Química de Materiais e Processos Metalúrgicos, Pontifícia Universidade Católica do Rio de Janeiro.

A demanda por veículos mais seguros e com baixo consumo de combustível vem levando a indústria automotiva a buscar novos materiais. A indústria do aço, ameaçada pela competitividade da indústria do alumínio, reagiu com uma série de novos aços de alta resistência. Dentre estes aços, os Aços Avançados de Alta Resistência (AHSS) podem ser destacados. Esses aços podem ser divididos em 3 gerações, cada uma delas com suas vantagens e desafios. A primeira geração tem os aços mais baratos, geralmente com microestrutura ferrítica/martensítica. A segunda geração possui os aços inoxidáveis austeníticos/ferríticos, com composição mais cara devido ao maior teor de liga, muitos deles apresentando efeito de plasticidade induzida por maclagem (TWIP). Entre essas duas gerações, uma terceira vem se sobressaindo, baseada em aços de composição mais barata, porém com processamento mais complexo, como os aços de tempera e partição (Quenching and Partitioning - Q&P). Como não existe apenas um único caminho para o sucesso, todas as três gerações vêm recebendo bastante atenção e pesquisa. Buscando atender parte da demanda do setor, a Companhia Siderúrgica Nacional (CSN), vem aprimorando seu portfólio de aços AHSS de primeira geração. Entre os aços de primeira geração, os mais utilizados hoje são os Dual-Phase (DP). No entanto, os aços DP apresentam alguns problemas, como a nucleação de vazios durante a deformação, o que é um fator limitante para suas propriedades mecânicas. Sua substituição por aços Complex-Phase (CP), com maiores quantidades de bainita e menos propensos a nucleação de vazio, vem sendo proposta. O processamento de aços de fase complexa

envolve uma sequência de etapas de laminação a quente e a frio, seguidas de um tratamento térmico. Na presente tese, foi estudada a produção de um aço CP1200 em uma linha industrial de galvanização por imersão a quente. O ponto de partida foi um aço CP1100. Amostras deste aço laminado a frio foram analisadas por dilatometria de forma a se obter a curva CCT. Utilizando os dados dilatométricos, um novo tratamento térmico foi proposto e realizado nas instalações da CSN, produzindo com sucesso um aço CP 1200. Ensaios de tração, dureza, dobramento e expansão de buraco foram realizados para medir as propriedades mecânicas do novo aço. A caracterização microestrutural foi realizada por meio de microscopia óptica (MO), microscopia eletrônica de varredura (MEV), microscopia de força atômica (MFA), difração de elétrons retroespalhados (EBSD) e microscopia eletrônica de transmissão (MET); a quantificação das micrografias foi realizada usando processamento digital de imagem e redes neurais. O aumento da propriedade mecânica foi atribuído ao aumento na fração de bainita, bem como de interfaces bainita-ferrita e bainita-martensita, que são menos suscetíveis a nucleação de vazios.

Palavras-Chave

AHSS; Complex-Phase Steel; CP1200; Transformação de Fases; Caracterização Microestrutural.

Table of Contents

Abstract	7
Resumo	9
List of figures	14
Table Index	26
Symbols and Abbreviations Index	28
1 Introduction	31
2 Goals	37
3 Literature Review	38
3.1. Microstructural evolution of steels	38
3.1.1. Bainite transformation	39
3.2. First Generation Advanced High Strength Steels	43
3.2.1. Dual-Phase Steel	43
3.2.2. Complex-Phase Steel	49
3.2.3. Alloying in AHSS	51
3.3. Dilatometry Methods	55
3.4. EBSD	56
3.4.1. EBSD Based Metallography	57
3.5. AFM	64
3.6. Machine Learning and Neural Networks	67
4 Experimental Methods	70
4.1. Material	70
4.1.1. Samples Identification (ID)	70
4.2. Production Process and Treatment	71
4.3. Dilatometry	72

4.4.	Mechanical Properties	73
4.5.	Metallography	75
4.5.1.	Light Optical Microscopy	75
4.6.	Atomic Force Microscopy (AFM)	76
4.7.	Scanning electron microscopy / EBSD	77
4.7.1.	EBSD Sample Preparation	78
4.7.2.	EBSD Data Cleaning	80
4.7.3.	EBSD Processing, Analysis and Segmentation	83
4.8.	Transmission Electron Microscopy	90
4.9.	Focused Ion Beam	90
4.10.	Image analysis	91
4.10.1.	Interface Segmentation	95
4.10.2.	Grain Size Measurements	98
5	Results	103
5.1.	Cold Rolled Steel	103
5.1.1.	Microstructure	103
5.2.	Calculations	106
5.3.	Dilatometry	107
5.3.1.	CCT curve	107
5.3.2.	Heat Treatments	109
5.3.3.	CP1100	114
5.3.4.	CP1200	116
5.4.	Hardness	118
5.4.1.	CCT Curve	118
5.4.2.	Heat Treatments	119
5.4.3.	CP1100/CP1200	120
5.5.	CP1200 Mechanical Properties	120
5.6.	LOM/SEM	121
5.6.1.	Prior Austenite Grain Size	121
5.6.2.	Austenitization Measurement	123
5.6.3.	CCT	124
5.6.4.	Heat Treatments	129
5.6.5.	CP1100	133

5.6.6.	CP1200	134
5.7.	AFM	135
5.7.1.	CP1100	135
5.7.2.	CP1200	138
5.8.	EBSD	140
5.8.1.	CCT Curve	140
5.8.2.	CP1100	142
5.8.3.	CP1200	144
5.9.	TEM	146
5.10.	Interface Quantification	150
5.10.1.	CP1100	150
5.10.2.	CP1200	152
6	Discussion	154
6.1.	Mechanical Properties	154
6.2.	Dilatometry	155
6.3.	Microconstituents	156
7	Conclusion	160
8	Suggestions for Future Work	162
8.1.	Gleeble	162
8.2.	Salt Pots	162
8.3.	X-Ray Tomography	162
8.4.	Mössbauer Effect	163
8.5.	Modelling of Phase Transformation	163
9	Bibliography	164

List of figures

- Figure 1.1 Steels classification according to the mechanical properties with the curve of theoretical values of combinations of ferritic/martensitic and austenitic/martensitic microstructures, adapted from Speer and associates [4]. 33
- Figure 1.2 Schematic design of the 2016 Chevrolet Cruze body structure the fraction of materials used on it. Cyan Mild Steel, Blue High Strength Steel, Pink Advanced High Strength Steel, Magenta Press Hardened Steel, Green Aluminum. Adapted from World Auto Steel [9]. 35
- Figure 3.1 Phase transformation diagram of Fe-C. 39
- Figure 3.2 Three possible paths through the bainite curve. Reproduced from Habreken and Economopoulos, 1967. 41
- Figure 3.3 Examples of bainite morphology. A – Granular bainite; B – Upper bainite; C – Degenerated Upper Bainite; D – Lower Bainite; E – Degenerated Lower Bainite. Adapted from Zajac *et al.* 2005 [12]. 42
- Figure 3.4 Lower bainite according to Tomita and Okabayashi. A – schematic design of the plate formed. B – Transmission electron microscopy image of a bainitic region. Adapted from Tomita and Okabayashi 1985 [17]. 43
- Figure 3.5 Processing of DP steels through hot rolling, reproduced from Kuziak *et al.* [3]. 45
- Figure 3.6 Processing of DP steel through cold rolling, reproduced from Kuziak *et al.* [3]. 46
- Figure 3.7 Thermomechanical processing used to obtain an ultrafine DP steel, adapted from Mazaheri *et al.* [30]. 47
- Figure 3.8 Void nucleation in a broken DP tensile specimen. Reproduced from Sarwar and Priestner [27]. 48

- Figure 3.9 Void nucleation within martensitic bands. Reproduced from Tasan et al. [34]. Upper figures present the undeformed condition, lower ones are the deformed states seen by digital image correlation, the heat map indicates the microscale strain field. White arrows point to nucleated voids in the microstructure. 48
- Figure 3.10 Schematic design of a CP treatment with isothermal bainite transformation. 50
- Figure 3.11 Schematic design of a CP treatment with continuous cooling transformation followed by isothermal transformation. 51
- Figure 3.12 Backscatter Kikuchi pattern from the CP1100 steel ferritic region, showing a (001) zone axis reflection. A – Obtained pattern. B – Obtained pattern plus simulation. 56
- Figure 3.13 Backscatter Kikuchi pattern indexing example. A – Kikuchi pattern. B – Kikuchi pattern mis-indexed as martensite. C – Kikuchi pattern indexed as ferrite. 57
- Figure 3.14 Example of phase identification of the CP1100, red ferrite, blue austenite, green cementite, orange martensite, and black zero solutions. A – Incorrect identification due to the martensite and cementite patterns additions. B – Identification with ferrite and austenite patterns. 57
- Figure 3.15 Dislocation density as a function of the transformation temperature. Reproduced from Garcia *et al.* [91]. 59
- Figure 3.16 Histogram of a HSLA steel IQ and its deconvolution. Reproduced from Garcia *et al.* [91]. 59
- Figure 3.17 IQ histogram for the DP590 and DP780 adapted from Garcia et al. DP590 has 66.8% of recrystallized ferrite, 14.6% of unrecrystallized ferrite, and 18.6% of martensite. As for the DP780, it has 55.4%, 14.7 and 29.6% respectively [91]. 60
- Figure 3.18 IQ histogram and its deconvolution of TRIP steel. Adapted from Garcia *et al.* [91]. 60
- Figure 3.19 Frequency of the aspect ratio. Adapted from Zhao *et al.* [92]. 61

Figure 3.20 Grain average misorientation angle distribution. Adapted from Zhao <i>et al.</i> [92].	61
Figure 3.21 EBSD and EPMA combined method threshold using the carbon concentration, IQ, and KAM line scans. Adapted from Bleck <i>et al.</i> [73].	62
Figure 3.22 Segmented image using the EBSD, EPMA combined method. Adapted from [73].	63
Figure 3.23 Variation of the dislocation density near the martensite-ferrite interface. Reproduced from Kadkhodapour <i>et al.</i> 2011 [93].	64
Figure 3.24 EBSD and SIMS analysis of Q&P steel. A – shows that the green area identified as martensite is indexed as ferrite. B – SIMS map showing the carbon concentration. Reproduced from De Moor and Speer [18].	64
Figure 3.25 Original diagram of the atomic force microscope. Reproduced from McClelland and associates [94].	65
Figure 3.26 Modern diagram of an atomic force microscope. Reproduced from Ros-Yáñez <i>et al.</i> [95]	65
Figure 3.27 Example of AFM characterization of a nital etched TRIP steel, published by Yáñez <i>et al.</i> [95]. 1,9 and 14 are ferritic regions, 2 is a bainite region.	66
Figure 3.28 Representation of the perception as a function of 3 different inputs and a binary response. Reproduced from Rosenblatt 1957 [103].	68
Figure 3.29 Graphic representation of a neural network. The data flows from the inputs to a final output following the path of the arrows. Adapted from Glassner 2018 [109].	69
Figure 4.1 Schematic design of the CP treatment	71
Figure 4.2 A schematic drawing of the dilatometric samples (dimensions in millimeters, mm)	72
Figure 4.3 Example of the Ac1 and Ac3 determination using the derivative curve.	73
Figure 4.4 Bending test design. Private communication [110].	73

- Figure 4.5 Hole expansion test schematics. Private communication [110] 74
- Figure 4.6 Difference between the Nital and the Nital + sodium metabisulphite etched regions on the CP840A500 seen by SEM. A – Interface of the two etchings. B- Nital etched region. C – Nital + sodium metabisulphite etched region. 75
- Figure 4.7 Example of surface roughness analyses sampling on an AFM image, numbers mark measured regions 76
- Figure 4.8 Example of the effects from background correction. A – image without correction. B – Corrected image. Blue arrows point two regions that would be incorrectly segmented without the background correction. 77
- Figure 4.9 LOM of the prepared samples. A – polished 0.25 μm . B – Polished at 0.02 μm . C – etched at 0.5 % Nital for 2s. 79
- Figure 4.10 Secondary electron image of a EBSD polished sample with channeling contrast. Green arrows point to SiO_2 residue over the sample surface. 80
- Figure 4.11 Example of the effect of cleaning on a fast obtained Band Contrast + IPF + Grain boundary map. A – 78% hit rate non cleaned map. B – 98.4% cleaned map. 81
- Figure 4.12 Example of cleaning on a KAM + GOS + Grain boundary map. A – 78% hit rate non cleaned map. B – 98.4% cleaned map. 81
- Figure 4.13 Example of the cleaning process step by step. A – Non-cleaned original image. B – Auto-cleanup with band contrast void exclusion image. C – Zero solution removal algorithm using three neighbors. D – 10 iterate zero solution removal using three neighbors, black arrow in zoomed region shows a misinterpretation of the results. 82
- Figure 4.14 Pattern quality maps and their respectively histograms. A – Band Contrast. B – Band Slope. C – Band Contrast + Band Slope. 84
- Figure 4.15 Example of a grain misidentification. A – Incorrect identification. B – Correct identification. 84

- Figure 4.16 Example of segmentation of ferrite and bainite using the FIJI software and the KAM+GOS map. A – KAM map. B – GOS map. C – KAM + GOS map. D – Gray scale of the KAM + GOS map. Black arrows point to bainite regions. 86
- Figure 4.17 Histogram of the 8 bits converted image. Blue arrow shows the martensite peak, red arrow the ferrite one and green the bainite. 86
- Figure 4.18 Line scan done over the EBSD map of the CP1100 steel. The segmented image was a red ferrite, green bainite, black martensite and blue austenite. The blue dashed line is the BC, the black solid line is the KAM and the yellow dashed line is the GOS. 88
- Figure 4.19 Example of misidentification of the microstructure in AZtecCrystal. A through D presents different segmentation results for the same EBSD map. 89
- Figure 4.20 Window of AZtecCrystal software. Black arrows point selected maps used for segmentation, as seen in zoomed area. Yellow arrow shows the protect phase FCC. Green arrow shows the quantification results. 89
- Figure 4.21 Liftout process. A – ROI with a platinum deposition. B – Probe in the corner of the ROI. C – Lift of the lamella. D – Welding of the lamella to the Cu grid. E – Beginning of the thinning process. F – Thinning process after a few minutes. G – Last steps of the thinning process. H – Polished lamella. I – Final thickness of the lamella. 91
- Figure 4.22 Example of the pre-processing. A) Original image; B) Image with enhanced contrast 92
- Figure 4.23 WEKA plugin window. 92
- Figure 4.24 Examples of marked regions. 93
- 4.25 Example of the improving segmentation process. A – Close look on a region with a single training process. B – Same region after 3 training were done. C – Region after 5 training were done. 94
- Figure 4.26 Example of miss segmentation in an image without preprocessing. A – Original image. B – Wrongly segmented image. 94

- Figure 4.27 Threshold interface and segmented regions. A – Software interface. B – Brown region. C – White region. D – Black region. 95
- Figure 4.28 Segmented EBSD map of the CP1200 steel. Red ferrite (45.9%), green bainite (35.2%), black martensite (18.7%) and blue retained austenite (0.2%). 96
- Figure 4.29 Example of the steps to separate the segmented microconstituents. A – Color threshold. B – 8 bits conversion. C – Threshold. 96
- Figure 4.30 Example of the noise cleaning and interface segmentation. A – Segmented bainite. B – Cleaned segmented bainite. C – Interface of the bainitic grains. The zoomed in area in A and B shows example of noise cleaned, as pointed by the yellow arrow. 97
- Figure 4.31 Color scheme used for the interfaces. 98
- Figure 4.32 CP1200 Colored interfaces following the RGB color scheme. Red ferrite, green bainite, blue martensite and their derived colors. 98
- Figure 4.33 Distribution of grain size on the CP1100 steel obtained using the AZtecCrystal software. A – Ferrite grains. B – Bainite grains. 99
- Figure 4.34 Image of grain size table on AZtecCrystal. 100
- Figure 4.35 Interface of the AZtecCrystal during the grain size analysis. Black arrow points to a highlighted grain in the list and the yellow arrow points to that grain been revealed on the map. 100
- Figure 4.36 Interface of the analyze particles tool from FIJI. 101
- Figure 4.37 Example of grain size measurement on the bainitic microconstituent of the CP1200 done using FIJI software. A – Original segmented bainite. B – Mask of the analyze particles. C – Bainite grain after morphological operation. D – New mask of the analyze particles. 102
- Figure 5.1 SEM secondary electron image of the cold rolled steel. A – 1000X magnification. B – 2000X magnification. C – 5000X magnification. D - 10000X magnification. Yellow arrow shows the ferrite, green arrow shows the perlite. 104

- Figure 5.2 Examples of segmentation from the 2000X magnification microscopy. A – Improper way where cementite was segmented instead of pearlite. B – Correct segmentation of the pearlitic region. 105
- Figure 5.3 WEKA segmentation of the cold rolled steel. A – Original 2000X image. B – Pearlite. C – Ferrite. 105
- Figure 5.4 Cleaned EBSD analysis of the cold rolled steel. A – Band Contrast plus Inverse Pole Figure. B – Inverse Pole figure with high 101 orientation. 106
- Figure 5.5 Continuous cooling transformation curve obtained from dilatometry experimentation. Cooling rate measured in °C/s, rate going from 30 to 0.1 from left to right. 107
- Figure 5.6 Relative change in length versus temperature curves. A – 50 °C/s. B – 30 °C/s. C – 20 °C/s, black arrow shows a small bainite transformation. D – 10 °C/s, black arrows point to martensite and bainite transformation. E – 7.5 °C/s, black arrows point to martensite and bainite transformation. F – 5 °C/s, black arrows point to martensite and bainite transformation. 108
- Figure 5.7 Relative change in length versus temperature curves. A – 2.5 °C/s Close to fully bainitic transformation. B – 1 °C/s, black arrow shows a very small deviation that indicates a ferrite transformation. C – 0.5 °C/s. D – 0.2 °C/s. E – 0.1 °C/s. 109
- Figure 5.8 Dilatometric data for the CP840AXXX treatments. 110
- Figure 5.9 Dilatometric data for the CP820AXXX treatments 111
- Figure 5.10 Dilatometric data for treatments CPXXXA500. 112
- Figure 5.11 Complex-Phase experimental heat treatments. 113
- Figure 5.12 Relative change in length as a function of temperature for treatments 1-6. 114
- Figure 5.13 Treatment used to reproduce the CP1100 thermal cycle in the dilatometer. 115

Figure 5.14 Dilatometric results for the CP1100 treatment. Black arrows point to the relevant deviations of the linearity.	116
Figure 5.15 Dilatometry treatment of CP1200. A – temperature x time curve. B – Relative change in length x temperature curve.	117
Figure 5.16 Closer look at the relative change in length x temperature curve for the CP1200 Steel. A – Linear section with no transformation from 820 to 700 °C. B – Very small ferritic transformation (back arrows) between 680 and 630 °C. C – Continuous cooling transformation of bainite (black arrows) from about 590 until the isothermal hold. D – Martensite start and finish temperature (black arrows) after the isothermal hold.	117
Figure 5.17 Hardness HV10 measurements done on the CCT samples.	118
Figure 5.18 Harness HV10 indentation if the CP800A500.	118
Figure 5.19 Hardness HV10 measures for the treatments.	119
Figure 5.20 Average harness HV10 measurements of the heat treated samples.	119
Figure 5.21 Vilela etching of the 950°C austenitized sample.	122
Figure 5.22 CP1100 and CP1200 Vilela etched microstructure. A – CP1100. B – CP1200.	122
Figure 5.23 Microstructure comparison between the A25 and the A50 samples.	123
Figure 5.24 Austenite content as a function of the intercritical temperature.	123
Figure 5.25 Microstructure of the CCT samples with decrease in cooling temperature seen by LOM at 2000X. A – 30 °C/s. B – 20 °C/s. C – 10 °C/s. D – 7.5 °C/s. E – 5 °C/s. F – 2.5 °C/s. G – 1 °C/s. H – 0.5 °C/s. I – 0.1 °C/s.	124
Figure 5.26 Nital + Metabisulfite etching, microstructure of the CCT samples with decrease in cooling temperature seen by LOM at 1000X. A – 30 °C/s. B – 20 °C/s. C – 10 °C/s. D - 7.5 °C/s. E – 5 °C/s. F – 1 °C/s.	125

- Figure 5.27 Ferrite amount depending on the cooling rate. Polynomial fit with 0.9979 R-square 125
- Figure 5.28 Microstructure of the CCT samples with decrease in cooling temperature seen by secondary electron imaging at 2000X. A – 30 °C/s. B – 20 °C/s. C – 10 °C/s. D - 7.5 °C/s. E – 5 °C/s. F – 2.5 °C/s. G – 1 °C/s. H – 0.5 °C/s. I – 0.1 °C/s. 126
- Figure 5.29 Microstructure of the 30 °C/s cooled sample seen by secondary electron imaging. Black arrows point to some precipitates free microconstituents. 127
- Figure 5.30 Microstructure of the 20 °C/s cooled sample seen by secondary electron imaging. 127
- Figure 5.31 Microstructure of the 7 °C/s cooled sample seen by secondary electron imaging. Black arrow point to an island like microconstituent that presents an incomplete transformation in its interior. 128
- Figure 5.32 Microstructure of the 2.5 °C/s cooled sample. A and B present 2000X magnification images. Black arrows point to an island like microconstituent with an incomplete transformation in its interior. Red Arrows point to bainitic ferrite. 128
- Figure 5.33 Closer view of the 2.5 °C/s cooled samples microstructure. 129
- Figure 5.34 Microstructure of CPXXXA500 steels. 130
- Figure 5.35 2000X magnification of CP840A500, CP830A500, CP820A500 and CP800A500 seen by scanning electron microscopy. Blue arrow point to a more banded morphology, green arrow point to a heterogeneous morphology and black arrow point to a clear martensitic banded microstructure. 131
- Figure 5.36 Large martensitic band in the CP800A500 seen by scanning electron microscopy. A – 5000X image. B – 10000X image. 131
- Figure 5.37 5000X magnification of CP840A500 and CP840A450 seen by scanning electron microscopy. Blue arrows point some larger grains, green arrows point to regions with small precipitates. 132

- Figure 5.38 20000X micrography of the CP800A500 steel seen by scanning electron microscopy. Black arrows point areas more prone to void nucleation, blue arrow to more traditional martensite islands, green arrow to a precipitate-filled microconstituent. 132
- Figure 5.39 LOM 500X image of CP1100. A – Color etched surface. B – WEKA segmented image. 133
- Figure 5.40 Secondary electron imaging of the industrial produced CP1100. A – 2500X. B – 5000X. C – 10000X. D – 20000X, white arrows point to over etching in martensitic/austenitic islands. 134
- Figure 5.41 LOM imaging of the CP1200. A – 500X magnification. B – 1000X magnification with improved contrast. 135
- Figure 5.42 SEM image of CP1200. A – 2000X magnification. B – 5000X magnification. C – 20000X magnification. White arrow points to plate like microstructure, yellow arrows point small second phases in a highly etched grain. 135
- Figure 5.43 Atomic Force Microscopy imaging of the CP1100 steel. A – 60x60 μm map. B – 40x40 μm map. C – 20x20 μm map. D – 10x10 μm map. 136
- Figure 5.44 Regions used for measurement of the height and roughness of the microconstituents. 137
- Figure 5.45 AFM 3D map of the CP1100 steel. 138
- Figure 5.46 Atomic Force Microscopy imaging of the CP1200 steel. A – 60x60 μm map. B – 40x40 μm map. C – 20x20 μm map. D – 10x10 μm map. 139
- Figure 5.47 AFM profile on CP1200 steel. A – AFM image with two profile lines. B – Height following the profile lines. Blue arrow point to martensite height, green arrow to bainite and red arrow to the ferrite. 139
- Figure 5.48 AFM 3D map of the CP1200 steel. Blue arrows points to martensite, green arrows to bainite, red arrows to ferrite and black arrows to precipitates. 140

Figure 5.49 EBSD analysis of the 2.5 °C/s cooled sample with low magnification. A – Band Contrast. B – Band Slope. C – Band contrast plus Band Slope. D – Kernel Average Misorientation. E – Grain Orientation Spread. F – Kernel Average Misorientation plus Grain Orientation Spread.

141

Figure 5.50 EBSD analysis of the 2.5 °C/s cooled sample with a higher magnification. A – Band Contrast. B – Band Slope. C – Band contrast plus Band Slope. D – Kernel Average Misorientation. E – Grain Orientation Spread. F – Kernel Average Misorientation plus Grain Orientation Spread.

141

Figure 5.51 Band contrast map for CP1100. A – Industrial processed. B – Dilatometric treated.

142

Figure 5.52 EBSD/EDS analysis of an industrially produced CP1100. A – Band contrast. B – Carbon EDS map. C – IPF z + Band contrast map. D – Phase ID map. E – KAM map. F – GOS map.

143

Figure 5.53 Fully identified EBSD map of industrially produced CP1100. Magenta ferrite, red bainite, black martensite, white retained austenite.

143

Figure 5.54 EBSD map of dilatometric treated CP1100. A – KAM + GOS. B – Segmented map, red ferrite, green bainite, blue martensite.

144

Figure 5.55 EBSD map for the steel CP1200. A – Band contrast map. B – IPF z map. C – KAM map. D – GOS map. E – KAM + GOS. F – Fully segmented map, red ferrite, green bainite, blue martensite.

145

Figure 5.56 Comparison between the secondary electron image and the Band Contrast. A – SE image with channeling contrast. B – Band Contrast

146

Figure 5.57 TEM imaging of CP1100. A, B and C – show the same region with increasing magnification. D – uses an image processing to reveal smaller details, such as the dislocations.

147

Figure 5.58 TEM image of CP1100. A – Interesting plate like morphology. B – Image enhanced contrast of the same regions reveals a martensitic transformed retained austenite (black arrow).

148

Figure 5.59 Ferrite grain with cementite plates. A – Bright field image of the ferrite grain. B – Dark field image. C – Indexed electron diffraction.	148
Figure 5.60 Bright field TEM image of austenite grain. A – Bright field image. B – Indexed electron diffraction.	149
Figure 5.61 TEM images of CP1200. A – Low magnification image from the whole sample. B – region with plate like precipitates. C – region with transformed retained austenite.	150
Figure 5.62 Interface of the bainite microconstituent of the CP1100 Steel.	151
Figure 5.63 RGB color image of the CP1100 interface. Red ferrite, green bainite, blue martensite and their respective combinations.	151
Figure 5.64 Interface of the bainite microconstituent of the CP1200 Steel.	152
Figure 5.65 RGB color image of the CP1200 interface. Red ferrite, green bainite, blue martensite and their respective combinations.	153
Figure 6.1 Side by side comparison of CP1100 and CP1200 dilatometric data	155
Figure 6.2 EBSD comparison between the CP1100 and CP1200 steel. A – CP1100. B – CP1200. Both images presents red ferrite, green bainite, blue retained austenite and black martensite.	157
Figure 6.3 AFM comparison between the CP1100 and CP1200 microstructures	157
Figure 6.4 Side by side comparison of the segmented interfaces. A – CP1100. B – CP1200.	158

Table Index

Table 1.1 Mechanical Properties and Applications of some of the most used steels in the automotive industry, adapted from Singh 2016 [2].	34
Table 3.1 Several empirical models for bainite start calculation. Fractions in wt.%.	43
Table 3.2 Influence of martensite content on the mechanical properties of DP steels. Adapted from Sarwar and Priestner [27].	44
Table 3.3 Typical composition for Dual-Phase steel (wt.%).	53
Table 3.4 Typical composition for Complex-Phase steel.	54
Table 3.5 Average roughness and height for each microconstituent according to Yáñez <i>et. al.</i> [95]	67
Table 4.1 Chemical composition of steel used in %wp [110].	70
Table 4.2 Mechanical properties of the CP1100 [110].	70
Table 4.3 Examples of samples ID.	71
Table 5.1 Microstructural quantification of cold rolled steel	105
Table 5.2 Bainite start temperature calculation.	106
Table 5.3 List of thermal treatments	109
Table 5.4 Hardness measurements for the CP1100 and CP1200 steels.	120
Table 5.5 Pilot scale tensile test done on CP1200 trials [110].	120
Table 5.6 Tension results for CP1200 measured at the initial, middle, and final regions of a processed plate [110].	121
Table 5.7 Prior Austenite Grain Size	122
Table 5.8 Ferrite quantification as a function of the cooling rate	125
Table 5.9 Quantification of CP1100 LOM images	133

Table 5.10 LOM quantification of the CP1200 microstructure	135
Table 5.11 Measurements done over the AFM image	137
Table 5.12 Sum of all the EBSD map microstructural quantification for the industrial CP1100	144
Table 5.13 EBSD quantification of CP1100 steel	144
Table 5.14 Sum of all the CP1200 EBSD maps microstructural quantification.	146
Table 5.15 Interface quantification for the CP1100	151
Table 5.16 Interface quantification for the CP1200	153
Table 6.1 Comparison between CP1100 and CP1200 mechanical properties	154
Table 6.2 LOM microstructural quantification for the CP1100 and CP1200 steels.	156
Table 6.3 Comparison between the CP1100 and CP1200 microstructural quantification	157
Table 6.4 Average grain size of each microconstituent obtained from EBSD maps.	158
Table 6.5 Comparison between the interface quantification of CP1100 and CP1200	158

Symbols and Abbreviations Index

Aust.SS.	Austenitic Stainless Steel
AHSS	Advanced High Strength Steel
BC	Band Contrast
B _f	Bainite Start
BH	Baking Hardening
BS	Band Slope
B _s	Bainite Finish
CBPF	Centro Brasileiro de Pesquisas Físicas
CCT	Continuous Cooling Transformation
CH	Cold Rolled
CP	Complex-Phase
CI	Confidence Index
CSN	Companhia Siderúrgica Nacional
DP	Dual-Phase
DLB	Degenerated Lower Bainite
DSHT	Dual Stabilization Heat Treatment
DUB	Degenerated Upper Bainite
EBSD	Electron Backscattering Diffraction
EDM	Electrical Discharge Machining
EDS	Energy Dispersion Spectroscopy
EM Lab	Electron Microscopy Laboratory
EPMA	Electron Probe Microanalysis
GAM	Grain Average Misorientation
GB	Granular Bainite
GM	General Motors
GOS	Grain Orientation Spread
HR	Hot Rolling
HSLA	High Strength Low Alloy

ID	Identification
IF	Interstitial Free
INT	Instituto Nacional de Tecnologia
IPF	Inverse Pole Figure
IQ	Image Quality
JMAK	Johnson Mehl Avrami Kolmogov
KAM	Kernel Average Misorientation
L-IP	Lightweight Induced Plasticity
LMD	Laboratório de Microscopia Digital
LOM	Light Optical Microscopy
M	Martensitic
M_f	Martensite Start
M_s	Martensite Finish
PUC	Pontifícia Universidade Católica
Q&P	Quenching and partitioning
SEM	Scanning Electron Microscopy
TEM	Transmission Electron Microscopy
TRIP	Transformation Induced Plasticity
TTT	Time Temperature Transformation
TWIP	Twinning Induced Plasticity
UB	Upper Bainite
UTS	Ultimate Tensile Strength
YS	Yield Strength
α	Ferrite
γ	Austenite

“To reach a port we must sail, sometimes with the wind, and sometimes against it. But we must not drift or lie at anchor”

Oliver Wendell Holmes

1 Introduction

Over the years technological advances have been accentuated and technological innovations can be observed in the market as a whole. The steel industry has seen part of these advances through the emergence of the **Advanced High-Strength Steels (AHSS)**.

Among the many industries and market niches that demand this class of new materials the automotive industry should be highlighted. After all, in the most recent years automotive applications have been the biggest motivator for investment in AHSS steels. This statement is evidenced by the way these steels are introduced in the literature [1]–[6]. The vast majority, not to say all companies in the automotive industry, have in recent years placed emphasis of aspects like safety and environmental impact. In one of the General Motors (GM) commitments you can read:

“Your journey should be safe, clean, and efficient...”

A statement that is not very different from Toyota's:

“There is only one planet Earth. Which is why we developed a line of vehicles that make the best possible use of our natural resources, and why we ensure that our facilities and plants minimize waste and energy while maximizing efficiency.”

The GM CEO Mary T. Barra has directly said:

“I believe the auto industry will change more in the next 5 to 10 years than it has in the last 50”

If you go from company to company looking into their commitments and beliefs they will say something on these lines.

Besides the new safety requirements, another concern is the reduction in vehicle weight. This reduction is a direct link to the increase in strength of several parts of the vehicle. The weight reduction grants the vehicle a higher efficiency when the same engine is in place. Consequently, the amount of CO₂ emitted by miles traveled is reduced.

To fulfill these industrial needs, research in steels and low-density alloys haven been conducted. Some steel companies and metallurgical research groups bet on AHSS steels as the best option.

The AHSS steels can be divided into 3 generations. The first is composed of steels such as Transformation Induced Plasticity (TRIP) steel, a steel with a microstructure consisting of ferrite, bainite, and a high concentration of retained austenite. Martensitic steels (M), consist of martensite or tempered martensite. Dual-Phase (DP) steels, contains ferrite and martensite, and finally Complex-Phase Steels (CP) consist of complex microstructures filled with bainite, ferrite, martensite, and retained austenite [3].

The second generation is composed of steels that generally have superior mechanical properties them the first-generation steels. They are highly alloyed, with a strong presence of retained austenite. In most second-generation steels, the Mn content is higher than 15% and may, in some cases, reach the mark of 25%. This generation is composed of Twinning Induced Plasticity (TWIP), Austenitic Stainless Steels (Aust.SS), and Lightweight Induced Plasticity (L-IP) steels. The major bottlenecks in the production of second generation steels are the difficulty of large-scale manufacturing, due to the high alloy contents and the complexity of the process; and the cost of manufacturing these steels is very high when compared to first generation steels [3].

The third generation AHSS is composed of steels of intermediate properties, also with great potential for application in the automotive industry, but largely still in the process of development. They are steels such as Quenching and Partitioning (Q&P), Quenching-Partitioning-Tempering and Dual Stabilization Heat Treatment (DSHT). These steels have interesting mechanical properties, do not require high alloy contents, and have production processes that allow fine control of their final

microstructures and properties (mainly Q&P). Unfortunately, they demand very fine control of process temperatures, requiring sudden temperature changes, which makes the processing of these steels complex, leaving many steel lines unable to process them.

Many authors have published several steel classifications according to their mechanical properties [7], [8]. One of these classifications can be observed in Figure 1.1. If the steels present in these classifications are analyzed from the point of view of their microconstituents, even if superficially, it is evident that the steels of the curve initiated by interstitial Free (IF) steels and finished in the martensitic steels are basically composed of a combination of ferrite and martensite. It was also proposed that the path to the third generation AHSS would be the combination of a microstructure composed of austenite and martensite, as published by Speer and associates in 2011 [4].

Singh published in 2016 an interesting table containing the main steels used in the automotive industry today. This table was adapted and reproduced in Table 1.1.

For reference, in the world auto steel web site some examples of steel and other materials application in new and old vehicles models can be found. Figure 1.2 shows a schematic design for the 2016 Chevrolet Cruze and the fraction of different materials used in its “body structure” [9].

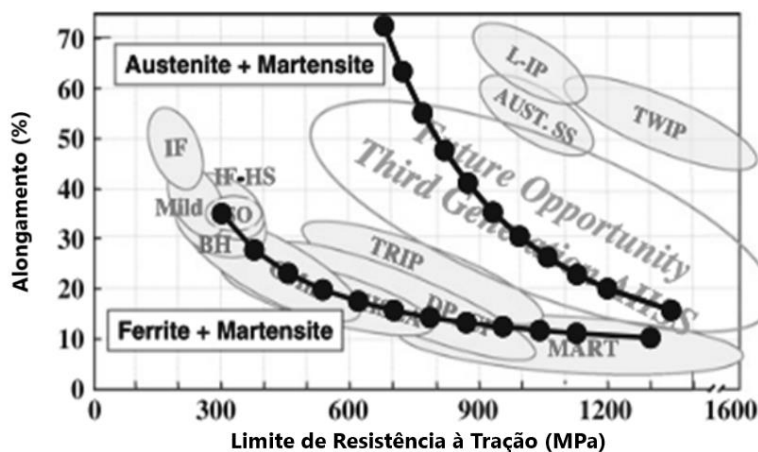


Figure 1.1 Steels classification according to the mechanical properties with the curve of theoretical values of combinations of ferritic/martensitic and austenitic/martensitic microstructures, adapted from Speer and associates [4].

Table 1.1 Mechanical Properties and Applications of some of the most used steels in the automotive industry, adapted from Singh 2016 [2].

Steel	σ_e (Mpa)	UTS (MPa)	EI. %	Application
BH 210/340	210	340	34-39	B
BH 260/370	260	370	29-34	B
CP 700/800	700	800	10-15	B
DP 280/600	280	600	30-34	B
DP 300/500	300	500	30-34	B
DP 350/600	350	600	34-30	A,B,C,W,S
DP 400/700	400	700	19-25	A,B
DP 500/800	500	800	14-20	A,B,C,W
DP 700/1000	700	1000	12-17	B
HSLA 350/450	350	450	23-27	A,B,S
HSLA 490/600	490	600	21-26	W
IF 260/410	260	410	34-38	C
IF 300/420	300	420	29-36	B
M 1250/1520	1250	1520	4-6	A
M 950/1200	950	1200	5-7	A,B
Mild 140/270	140	270	38-44	A,C,F
MnB	1200	1600	4-5	S
TRIP 450/800	450	800	26-32	A,B

A-ancillary parts, B-Body Structure, C-Closures, F-Fuel tank, S-suspension/chassis, W-Wheels

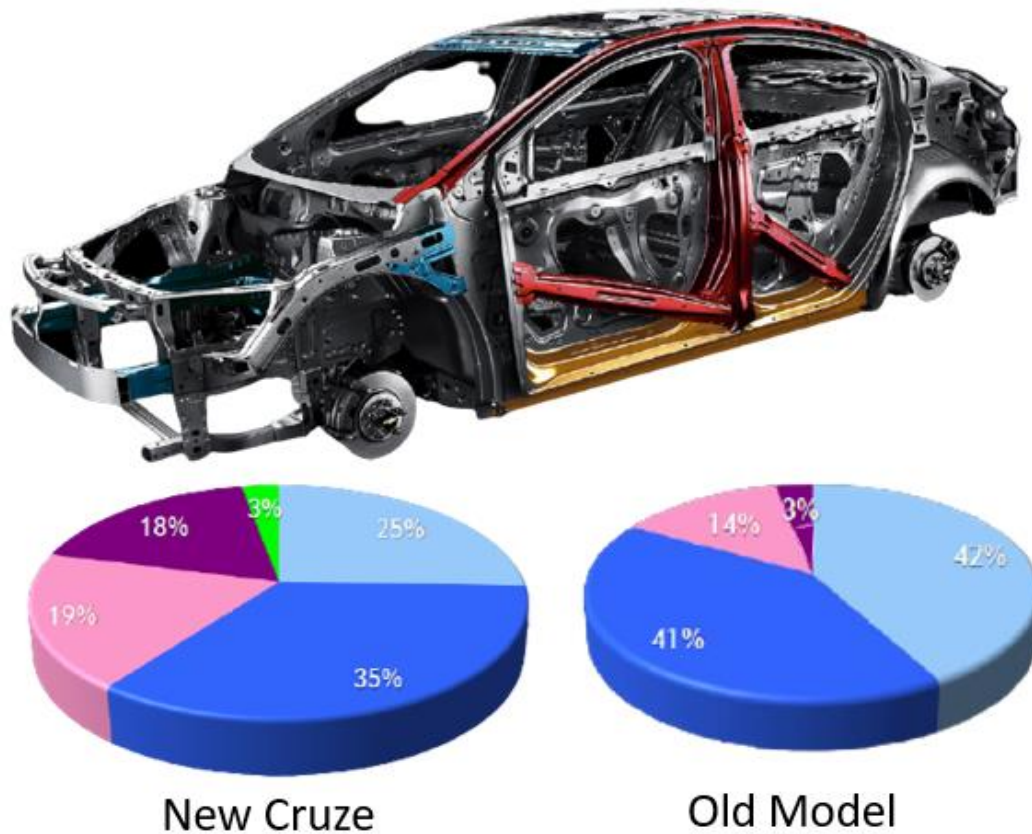


Figure 1.2 Schematic design of the 2016 Chevrolet Cruze body structure the fraction of materials used on it. Cyan Mild Steel, Blue High Strength Steel, Pink Advanced High Strength Steel, Magenta Press Hardened Steel, Green Aluminum. Adapted from World Auto Steel [9].

Among the first generation AHSS steels, the Companhia Siderúrgica Nacional (CSN) has been producing, as the market demands, Dual-Phase and Complex-Phase steels of various mechanical properties. Recently, the company produced a new CP1100 steel and also realized the upcoming demand for CP1200 steels, which are not yet part of its portfolio. The theme of this thesis was decided in order to meet this demand.

The newly produced CP1100 already has a composition that is near the limit of the production line, therefore, the first challenge is to produce the new CP1200 without changing the composition used for the CP1100. This also is necessary to keep the price competitive for the final product, making no changes in the production line, such as new rolling steps.

Knowing that there is a need for a CP1200, let be established that a CP1200 steel needs, by definition, to present more than 1200 MPa of

tension strength, more than 800 MPa of yield stress and at least 8% of total elongation.

There will be two main innovations presented in this current thesis, they are aligned with this industrial challenge as well as with the characterization process. They are the design of a new heat treatment for the CP1100 composition, changing the final microstructural fractions; and the use of image analysis to quantify the interfaces distribution, using this quantification to explain the changes in the mechanical properties.

2 Goals

- Based on the need of the market and our partners at CSN, this thesis aims to obtain a CP1200 steel using thermal treatments that can be reproduced at CSN's hot dip galvanizing line. A CP1200, by definition, should have 1200 MPa of ultimate tensile strength (UTS), more than 800 MPa of yield Strength (YS), and at least 8% of total elongation.
- Characterize and correlate the microstructure of the produced steels with the desired mechanical properties.

3 Literature Review

In this chapter, a review of some basic, but essential, points for the study of CP steels will be provided, including a description of basic microconstituents of steels. The state of the art of CP steels is also presented in this chapter, with the current research focus and the difficulties encountered.

3.1. Microstructural evolution of steels

To understand the microstructural evolution of steels, the first thing to do is to look at its two main elements, iron and carbon. The iron possesses one polymorphic transformation close to 910°C. At this temperature, the α -iron, also called ferrite, turns during heating to γ -iron, also called austenite. The presence of carbon in the chemical composition of the material is what allows the simple iron bar to become steel. The Fe-C phase diagram is one of the most seen in classrooms for the field of engineering and materials science. Through it, one can observe the set of temperatures and compositions that give rise to each stable, or metastable, microstructure of the steels (those between 0.02 and 2% carbon). In addition, some metastable structures can be formed. The more simple and usual transformation has been largely and consistently described in textbooks, but in some cases, complicated transformation as martensitic and bainitic can be harder to understand. In the next few sections, a brief review will be made on bainitic/martensitic phase transformation in steels. Understanding the possible combinations and transformations between these microconstituents is the key to controlling the properties of some steels. In Figure 3.1 one can see part of the Fe-C phase diagram produced in the Thermocalc software.

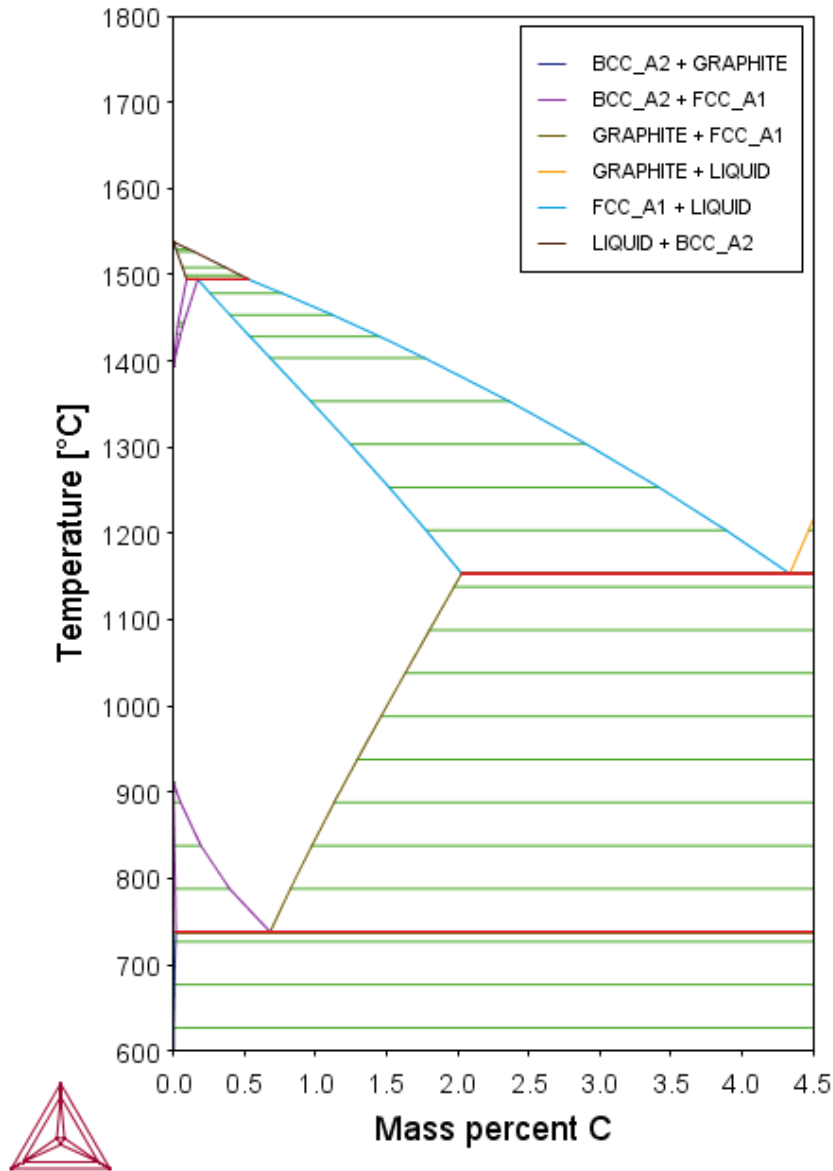


Figure 3.1 Phase transformation diagram of Fe-C.

3.1.1. Bainite transformation

The first description of bainite was provided in the late 20's by Davenport and Bain. They were studying the isothermal transformation below the temperature for fine perlite formation and above that for martensite [10].

Bainitic microstructures can take many different forms. Krauss has written that it can be a mixture of ferrite and cementite in a series of non-

lamellar arrays, mostly in medium- and high-carbon steels, or it may appear as acicular crystals in the presence of martensite [11].

Zajac and associates have generalized the bainite description as the eutectoid austenite decomposition that occurs in a competitive non-lamellar, non-cooperative reaction [12]. Or as Caballero and associates described a “*diffuseness growth of tiny platelets known as sub-units*” [13].

It was Mehl, in 1939, who was the first to distinguish bainite in two different forms, upper and lower bainite. Upper bainite was characterized as a lathlike morphology with habit plane near $\{111\}_\gamma/\{110\}_\alpha$. The lower bainite was characterized as platelike with an irrational habit plane [14]. At that time, temperature thresholds were also used to define upper/lower. As the transformation temperature varies a lot with composition, nowadays the use of that as a threshold would be imprecise.

Mehl’s distinction is applied for isothermally transformed bainite. When we look at continuous cooled bainite, things can get even more confusing. Dilatometric methods can be used for understanding the transformation that occurs during cooling, but as bainite has upper and lower characteristics, different kinds of bainite can show up in the same steel. Bramfitt and Speer have written that even just passing through the bay or nose of the bainitic transformation curve will not produce a single, uniform, constituent that can be termed bainite [14]. That is made even worse by the possible presence of microconstituents such as martensite, ferrite, perlite and even retained austenite.

The different kinds of microstructure formed depend on the supersaturation of carbon, the kinetics of carbon diffusion, the cooling, and the steel composition as a whole. Habreken and Economopoulos [15], back in 1967, had already shown different bainite constituents formed depending on the path through the bainite curve, as reproduced in Figure 3.2. The first kind is an acicular carbide-free morphology that he called granular bainite (I). The second is the upper bainite (II) and the last is the lower bainite (III).

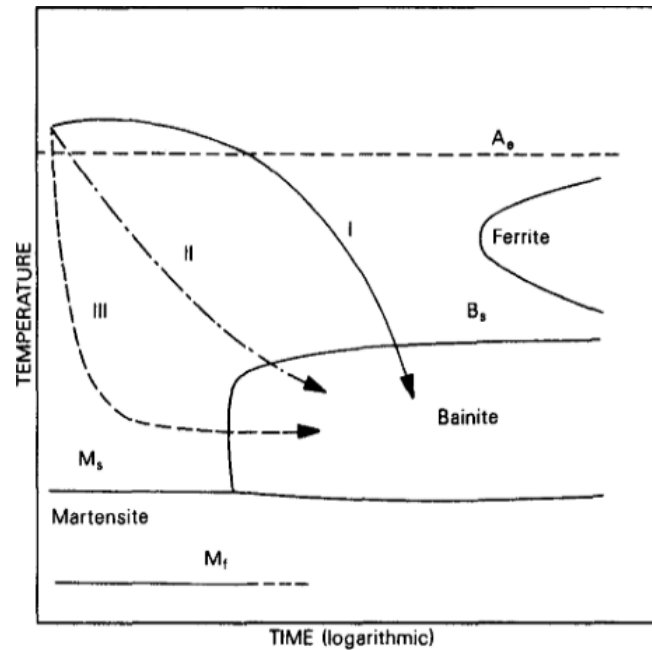


Figure 3.2 Three possible paths through the bainite curve. Reproduced from Habreken and Economopoulos, 1967.

Buchi and associates [16] were the first to suggest that the granular bainite forms because carbon diffuses very fast in the newly formed ferrite/austenite interface. That way there is no time to form the interlath cementite.

More recently bainite was identified by five different morphologies [12], they are:

- Granular Bainite (GB) – irregular shaped and distributed bainitic ferrite with small second phases inside. It is formed in the highest temperature ranges.
- Upper bainite (UB) - it is the lath-like morphology that comes along with interlath cementite precipitates formed in lower temperatures than the GB.
- Degenerated Upper Bainite (DUB) – If carbide precipitation is inhibited for any reason, the regular UB will form with retained austenite or retained austenite/martensite in the place of the carbides.
- Lower Bainite (LB) – In low carbon steels, it will be remarkably similar to the lath-like morphology from the upper bainite, but with precipitation inside the laths. In higher carbon

concentrations, it will show a plate-like morphology with even more precipitation.

- Degenerated Lower Bainite (DLB) – Following the same logic as the DUB it has M/A islands in the place of cementite.

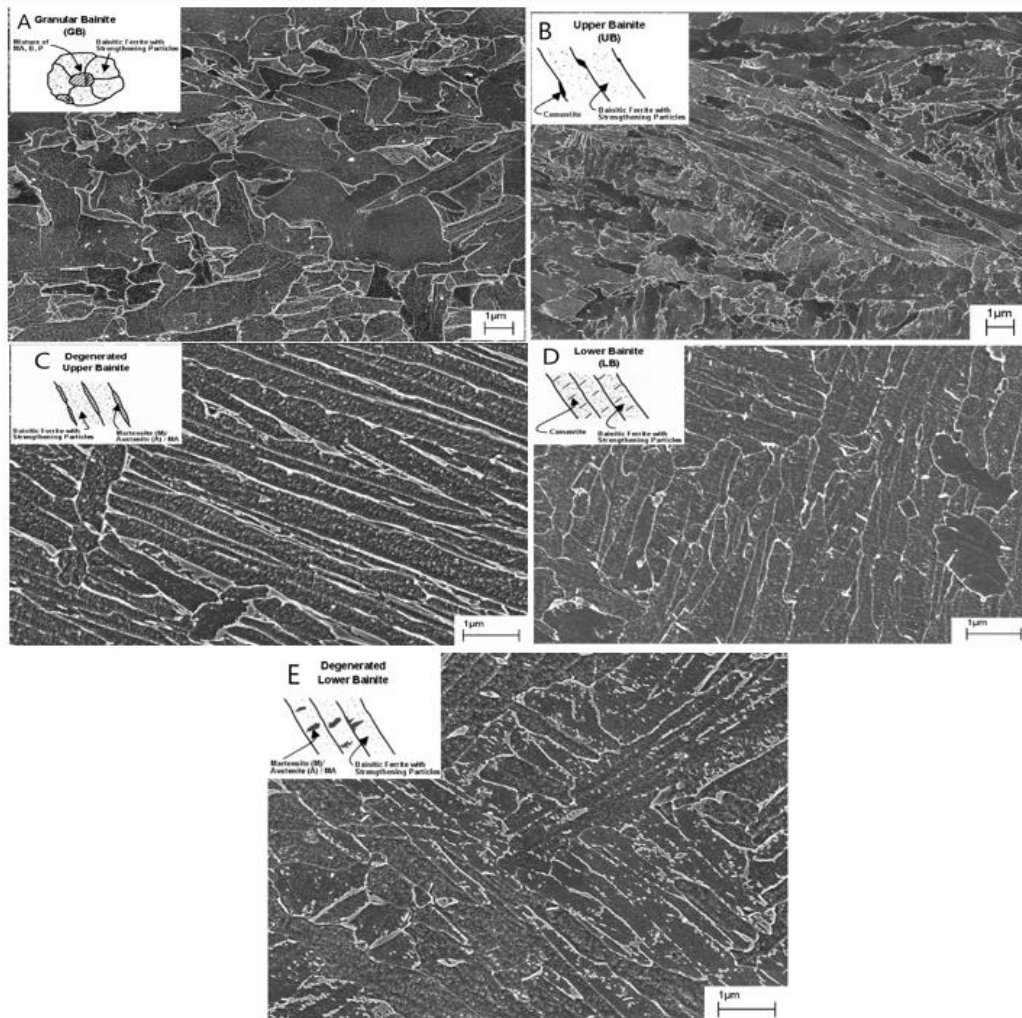


Figure 3.3 Examples of bainite morphology. A – Granular bainite; B – Upper bainite; C – Degenerated Upper Bainite; D – Lower Bainite; E – Degenerated Lower Bainite. Adapted from Zajac *et al.* 2005 [12].

Understanding and trying to control these different morphologies of bainite is, therefore, very important. In ultrahigh strength low alloy steel, Tomita and Okabayashi have reported an increase of more than 250MPa of strength by forming 30% of lower bainite [17]. They reported lower bainite that forms in a plate like morphology, as can be seen in Figure 3.4.

An increase in mechanical properties may not be the only goal for bainite formation. That is because the bainite transformation has been reported as being a “*substantial austenite retention*” mechanism [18]. An effect prominent in TRIP and TRIP-aided bainitic steels.

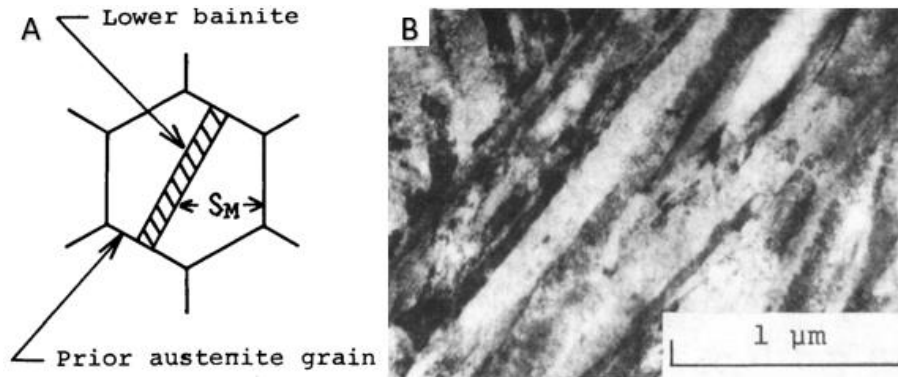


Figure 3.4 Lower bainite according to Tomita and Okabayashi. A – schematic design of the plate formed. B – Transmission electron microscopy image of a bainitic region. Adapted from Tomita and Okabayashi 1985 [17].

One important aspect of the metallurgical process that involves the bainitic transformation is the determination of the temperature at which transformation begins. Several empirical equations have been published on this subject and are presented in Table 3.1.

Table 3.1 Several empirical models for bainite start calculation. Fractions in wt.%.

Model	Equation
Bodnar #2 [19]	719-127C-50Mn-31Ni-27Cr-61Mo
Kirkaldy [20]	656-57.7C-35Mn-75Si-15.3Ni-34Cr-41.2Mo
Kunitake [21]	732-202C-85Mn+216Si-37Ni-47Cr-39Mo
Lee #2 [22]	745-110C-59Mn-39Ni-68Cr-106Mo+17MnNi+6Cr ² +29Mo ²
Li [23]	637-58C-35Mn-15Ni-34Cr-41Mo
Miettinen [20]	537,86-132,17C+138,04Si+34,65Mn+251,53Cr-831,99CSi-7,46CMn
Suehiro [24]	718-425C-42,5Mn

3.2. First Generation Advanced High Strength Steels

3.2.1. Dual-Phase Steel

Dual-Phase (DP) steels are part of the first generation AHSS and represent one of the most prominent [25], and used, in the automotive industry [26]. Some authors consider the first generation steels to be the most used in the automotive industry [1].

They are characterized by their microstructures composed of a ductile ferritic matrix and 20 to 25% of martensite [27], or martensite with traces of austenite reaching fractions of 10 to 40% [3]. According to the literature, dual-phase steels have a tensile strength limit in the range of 500 to 1200 MPa [3]. During the processing of these steels, the transformation of austenite into martensite creates a high density of dislocations with unobstructed mobility in the ferrite grains, that is, without stacking dislocations hindering the movement. The effect of this density of mobile dislocations is that, under low stresses, the steel presents a continuous, although heterogeneous [28], deformation [27]. These steels have been in the market for decades, as early as 1996. Sarwar and Priestner published a study on the influence of the martensite fraction on the mechanical properties of DP steels. Table 3.2, adapted from this publication, presents the data obtained by them [27]. The identification (ID) done in the table follows this pattern: the number on the left is the amount of cold rolling work, the BQ is the iced brine-quenching, HWQ is the hot-water quenching; the number on the right is the intercritical annealing temperature.

Table 3.2 Influence of martensite content on the mechanical properties of DP steels. Adapted from Sarwar and Priestner [27].

ID	Martensite (%)	YS 0.2 (%)	UTS (%)	Uniform Elongation (%)	Total Elongation (%)
0BQ780	55	645/570/600	1012/924/1014	6.39	12
50BQ780	48.9	670	1068	5.87	8.9
0HWQ780	27	360/357/365	703/645/694	5.75	10
50BQ780	32	305/270	691/667	8.09	17.3
0BQ740	30.7	450/495	835/838	5.94	7.29
50BQ740	29.4	525/516	892/871	5.34	8

Although they have been in the market for many years, the development of DP steels has not stopped. Many vehicle parts, already produced with DP steels, can be replaced by parts also made of DP steels, but with greater strengths and thinner thicknesses. Yoshinaga and associates published in 2018 [29] that a part manufactured with DP590 steel, with a thickness of 1.6 mm, could be replaced by a similar one, made with DP1180 steel, with a thickness of 1.2 mm. This replacement would result in a 25% reduction in the weight of the part [29].

The DP steel manufacturing process can take place in two ways. The first consists of hot rolling, followed by the nucleation of ferrite, a quick cooling (fast enough to avoid bainite formation), reaching the M_s , and nucleating martensite from the rest of the austenite. Note that the initial nucleation of ferrite releases carbon that diffuses to austenite, the consequence of which is the reduction of M_s [3]. In Figure 3.5, a cooling scheme can be observed in this manufacturing process.

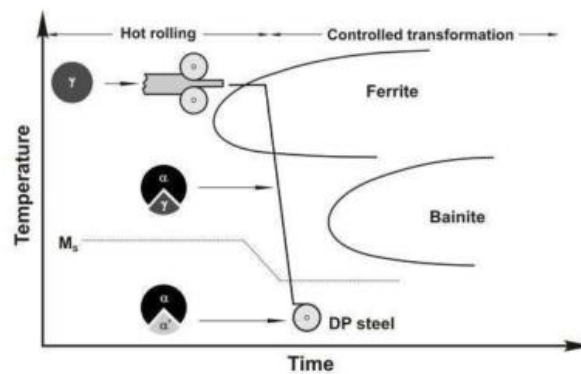


Figure 3.5 Processing of DP steels through hot rolling, reproduced from Kuziak *et al.* [3].

In the second method, after hot rolling, the steel is heated to the intercritical region and then quenched. That way, part of the microstructure is intercritical ferrite. Therefore, after tempering, the steel is predominantly composed of martensite and ferrite, with some occasional precipitates and retained austenite. The proportions between martensite and ferrite depend on the intercritical temperature used and the initial microstructure of the steel. There is also the possibility of some pearlite not completely

decomposed during the intercritical treatment [3]. In Figure 3.6, the last step of this processing can be observed.

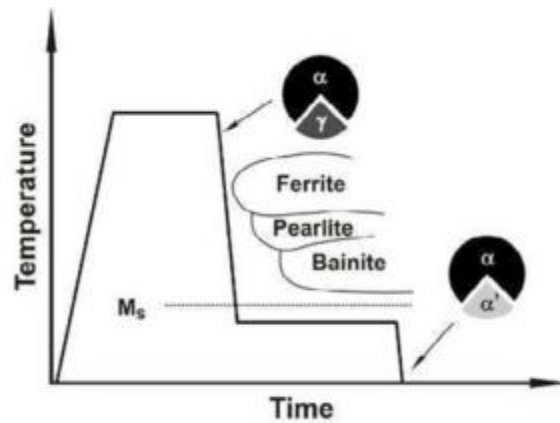


Figure 3.6 Processing of DP steel through cold rolling, reproduced from Kuziak et al. [3].

Besides the two usual methods, some new approaches are trying to achieve higher strengths through new treatments. Mazaheri *et al.* in 2015 used an ultrafine grained strengthening mechanism through a double heat treatment with a cold rolling step between them. It was essentially a hot rolled DP steel that was cold rolled, and heat treated again. That way, there is a competition between the recrystallization and nucleation process, which results in smaller sized grains. The thermomechanical processing used can be seen in Figure 3.7. It needs to be noticed that a steel production like this can no longer be classified as first generation AHSS steel. The complexity and cost of the process, as well as the new properties, would make this a third generation AHSS steel.

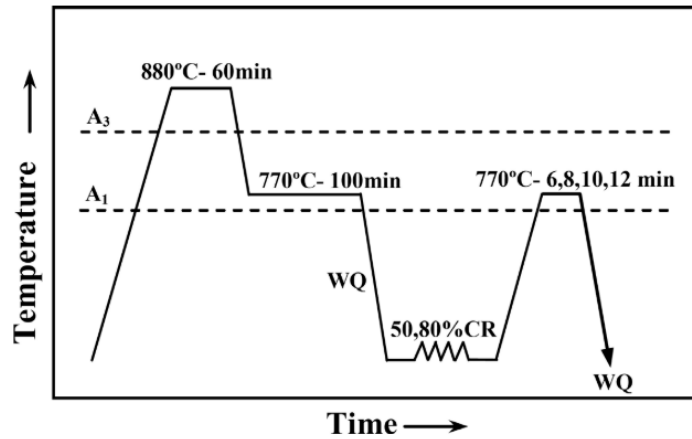


Figure 3.7 Thermomechanical processing used to obtain an ultrafine DP steel, adapted from Mazaheri *et al.* [30].

3.2.1.1. Hole Expansion and Void Nucleation

Two important aspects need to be considered when talking about DP steels. The first one is the hole expansion ratio. Automobile parts, more often than not, need to undergo several bending steps. So, the steel not only needs a high strength, but it also needs a reasonable level of stretch flangeability [31], a property that is usually measured by hole expansion testing [32].

As Fonstein [31] has pointed out, steels like DP, TRIP, and TRIP-aided DP, usually chosen for the automobile industry due to their high strength and elongation, have high sensitivity to edge fracture and low hole expansion ratio [31]. In DP steels the problem can be even worse due to a second important aspect, the void nucleation.

When under stress, DP steels will, due to the high hardness contrast between the martensite and the ferrite, nucleate small voids in the grain boundaries. A small part of the elongation of DP steels comes from these voids, but they excel in crack propagation [33]. Figure 3.8 shows an example of void nucleation in dual phase steels.

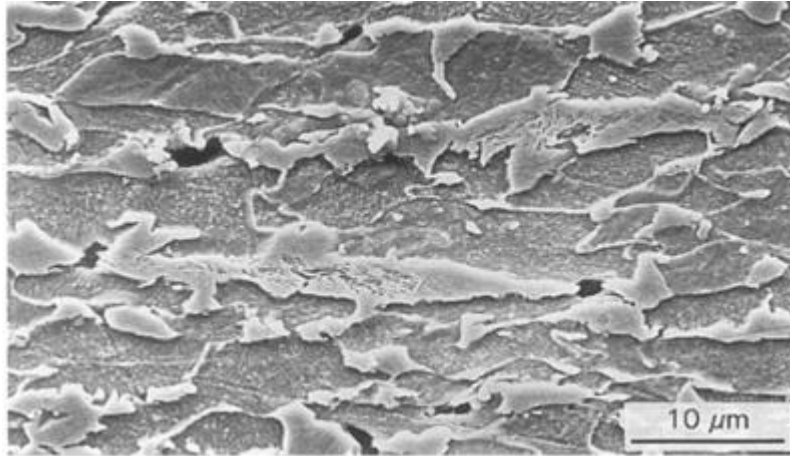


Figure 3.8 Void nucleation in a broken DP tensile specimen. Reproduced from Sarwar and Priestner [27].

The void nucleation problem can be even worse in a banded microstructure. In the treated dual-phase steel, martensite bands can increase the tendency to void nucleation. The small ferritic regions between those bands can lead to void nucleation, as can be seen in Figure 3.9 reproduced from Tasan and associates [34].

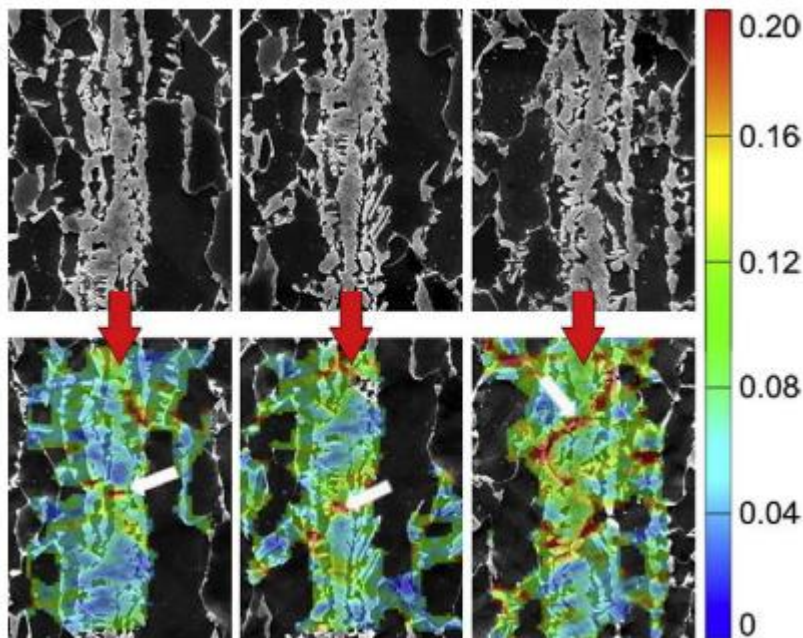


Figure 3.9 Void nucleation within martensitic bands. Reproduced from Tasan et al. [34]. Upper figures present the undeformed condition, lower ones are the deformed states seen by digital image correlation, the heat map indicates the microscale strain field. White arrows point to nucleated voids in the microstructure.

There is a clear goal in the industry to develop new steels that are superior not only to the DP ones but also to TRIP steels, as reported by De Moor and Speer [18]. One viable alternative for the DP, TRIP, and TRIP-aided DP steels is the complex-phase steels.

3.2.2. Complex-Phase Steel

Complex-Phase (CP) steels, often called multiphase steels, are a class of first generation AHSS steels with great potential for application in the automotive industry. These steels are constituted of bainite, ferrite, martensite, and austenite islands [33], [35]–[43]. CP steels have been studied, mainly, as substitutes for DP steels. One reason, as previously mentioned, is that in applications with a sharp corner, DP steels show high sensitivity to edge fracture and can present quick nucleation and growth of voids between their constituent phases. CP steels have already shown superior resistance to damage in this type of application, with reports of CP800 steels, with 800MPa of tensile strength, presenting, in a sharp corner, up to three times more resistance than the competitor of similar mechanical resistance steel DP780 [26]. In comparisons like this, another big difference between a DP and a CP steel with the same UTS limit would be their yield strength, with CP steels presenting a higher YS than DP ones [43].

The greater resistance to void formation of CP steels, when compared to DP steels, can be explained by their bainitic contents. It has also been mentioned that void nucleation is a problem created, due to the high hardness contrast between the martensite and the ferrite. So, the bainite provides a smaller hardness contrast in CP steels, when compared to the DP steels, thereby reducing the tendency for voids to form at the interfaces. Granted, that there are still instances of martensite/ferrite grain boundary and as such, some void nucleation occurs. Martin and associates in 2018 showed that in CP1200 steels, the area occupied by these voids is approximately 0.14%, well below the typical area for DP steels, 2% [33].

Another interesting property of the CP steels is their very high YS / UTS (yield strength / Ultimate Tensile Strength) ratio. This allows these

steels to work under high mechanical or cyclical stresses for long periods without suffering significant fatigue damage or creep failures [1].

In a similar fashion to the DP steels, the CP steels can be produced from a hot-rolling or a cold-rolling process. Due to cold work, the cold-rolled CP steels have smaller grains and a higher UTS when compared to the hot-rolled ones. Considering the high strength demand for the steel investigated in this thesis, only cold-rolled CP steels were used. Some authors have done extensive research in hot-rolled CP steels, and more information can be found in [35], [36], [39].

The CP processing does not differ much from the DP one. It begins with an intercritical soak, during which a ferritic/austenitic microstructure is formed. It is followed by quenching to a bainitic transformation temperature with a short hold a few seconds long. During this hold, some of the austenite will transform to bainite. Then a second quenching takes the steel to room temperature. In this last quenching step, the majority of the remaining austenite will transform to martensite. In Figure 3.10 a schematic treatment can be seen.

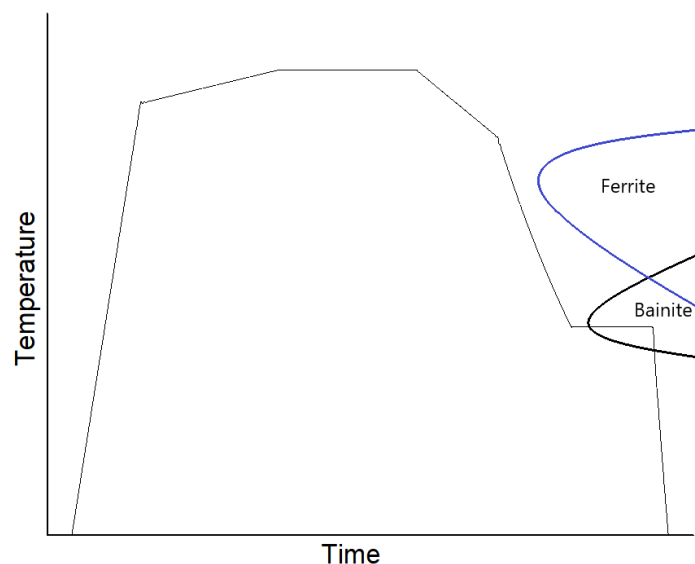


Figure 3.10 Schematic design of a CP treatment with isothermal bainite transformation.

Some variations to this treatment are possible. On an industrial scale, a galvanization step is necessary, so unless the hold temperature is low enough to be done together with the galvanizing, an extra quenching will be

necessary. Other than that, due to the processing lines, isothermal transformation is unlikely. Continuous cooling bainitic transformation followed by isothermal transformation during hold is more viable. Figure 3.11 shows a more realistic processing.

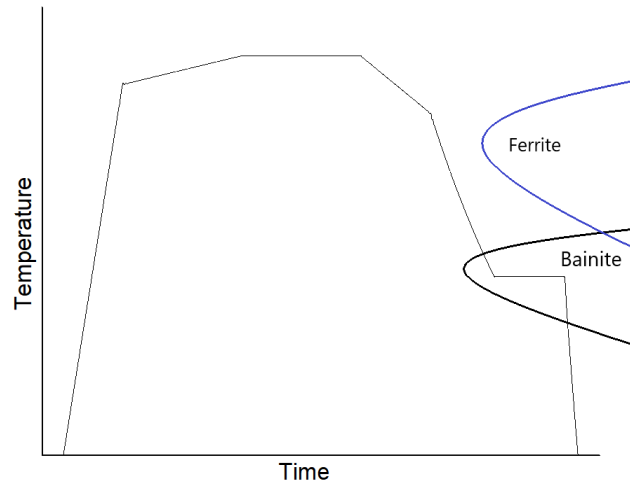


Figure 3.11 Schematic design of a CP treatment with continuous cooling transformation followed by isothermal transformation.

3.2.3. Alloying in AHSS

The analysis of alloying elements is never an easy one. Alloying not only affects the phases and microconstituents formed, but also the speed and path of transformation to said phases. Another important factor is that any alloying element does not have a single effect, but a series of them, some positive, others to the desired properties [44]. Those effects can overlap or not, depending on the different combination of elements. Thus, pointing out the elements that cause a particular effect is a complicated job.

Many effects of microalloying are not studied directly on AHSS steels, but concepts previously established in other steel products, such as HSLA steels for instance, where a lot of the niobium effect on grain size control has been studied [45]–[48]. However, some considerations need to be taken, for example, high amounts of aluminum are added to Q&P steel to increase the amount of retained austenite and the cementite precipitation [18], [49], besides reducing the final density [50]. But, small aluminum content on DP and CP steels is only to reduce the oxidation [43].

Since many aspects of element alloying are well explained in the literature, in this thesis the focus will be given to the effects of elements used in AHSS steels and new findings reported. First, for a reference, typical compositions for some Dual-Phase (Table 3.3) and Complex-Phase (Table 3.4) steels are presented.

C – The main effect of carbon in DP and CP steels is the strengthening of the martensitic phase [25]. Carbon will also affect the CCT diagram, shifting the transformation curves toward longer transformation times [51].

Al – Aluminum has been reported [52] as affecting the fine precipitation, improving the grain refinement results, retarding the cementite precipitation, increasing the carbon content in the austenite, speeding up the kinetics of austenite to bainite transformation, and increases the Ms temperature [52]. But, in lower amount is mostly used to prevent oxidations [43].

Mn – Is added between 1.5 to 3% to increase the strength of ferrite by solid solution, but it also stabilizes the austenite [25].

Mo, Cr – The main effect is to modify the phase fields in the CCT to give enough time to process the complex microstructures [53], retarding the perlite and bainite formation [25], [54].

Si – Facilitates the ferrite formation [25]. Si has some inhibition effect on the cementite precipitation [55]–[57], pushing out the formation to longer times and higher temperatures.

V, Nb, Ti – Both are used for precipitation strengthening and microstructural refinement. That is, Nb, V, and Ti precipitates will limit the size of the austenite during the intercritical or austenitization treatments, therefore reducing the final grain size [25], [53], [58], [59].

B – Boron has been reported as promoting the formation of fine precipitates, grain boundary segregation and for hindering the kinetics of austenite to ferrite transformation [52]. The last effect is very useful for CP treatments.

Table 3.3 Typical composition for Dual-Phase steel (wt.%).

DPXXX [Ref.]	C	Mn	Cr	Si	Mo	P	Al	Nb	Ni	V	Ti	Cu	Cr+Mo	Nb+Ti
600-1000 [27]	0.166	1.03	0.14	0.24	0.04	--	--	--	--	--	--	--	--	--
800-1000 [30]	0.17	1.15	0.95	0.4	--	0.025	--	--	--	--	--	--	--	--
590 [58]	0.051	1.51	--	0.1	--	0.011	0.06	0.02	--	--	--	--	0.5	--
590 [58]	0.06	1.5	--	0.4	--	0.01	0.05	0.02	--	--	--	--	0.48	--
600 [60]	0.08	1.51	0.02	0.1	0.01	0.012	--	0.007	<0.04	<0.004	0.007	0.025	--	--
600 [61]	0.1	1.5	--	0.15	--	--	--	--	--	--	--	--	0.8	--
600 [62]	0.098	0.85	0.73	0.24	<0.005	0.048	0.036	<0.005	0.03	<0.005	0.014	--	--	--
600 [62]	0.08	1	0.4	0.3	--	0.005	<0.03	--	--	--	<0.03	--	--	--
780 [58]	0.06	1.48	--	0.42	--	0.01	0.05	0.04	--	--	--	--	0.48	--
980 [58]	0.151	1.76	--	0.42	--	0.01	0.064	0.024	--	--	--	--	0.83	--
980 [63]	0.15	1.45	--	0.3	--	0.01	0.04	--	--	--	--	--	--	--
980 [64]	0.07	2.5	--	0.1	--	0.01	0.03	--	--	--	--	--	--	--
1000 [65]	0.134	1.449	--	0.197	--	0.012	0.04	--	--	--	--	0.0073	0.035	0.0149
1080 [58]	0.150	1.74	--	0.41	--	0.01	0.072	0.043	--	--	--	--	0.83	--
1200 [66]	0.12	1.6	0.03	0.2	0.2	0.01	0.035	0.001	0.04	0.01	0.03	0.005	--	--
1200 [65]	0.079	4.505	--	0.206	--	0.0096	0.043	--	--	--	--	0.0059	0.0297	0.0380
1400 [66]	0.19	1.2	0.02	0.2	0.2	0.007	0.04	0.002	0.04	0.007	0.03	0.007	--	--

Table 3.4 Typical composition for Complex-Phase steel.

CPXXX [Ref.]	C	Si	Mn	P	Al	V	Cu	N	Ni	Mo	Cr	Nb	S	Ti	Cr+Mo	Ti+Nb
n.d [67]	0.05	0.04	1.88	0.005	0.05	--	--	0.004	--	0.49	--	0.048	--	--	--	--
n.d [68]	0.24	0.27	1.14	0.015	--	--	--	--	--	--	0.17	--	0.001	0.036	--	--
600 [28]	0.10	0.14	1.51	0.009	--	--	--	--	--	--	0.8	--	--	--	--	--
800 [19]	0.05	0.55	1.5	--	--	--	--	--	--	--	0.6	--	--	0.14	--	--
800 [70]	0.16	0.035	2.2*	--	0.05	--	--	--	--	--	--	--	--	--	2.2*	0.005
800 [32]	0.14	0.14	2.5*	0.011	--	--	--	--	--	--	--	--	--	--	2.5*	--
800 [71]	0.13	0.2	2.1	0.008	0.55	0.007	0.010	--	0.02	0.04	0.270	0.2	0.004	0.003	--	--
800 [72]	0.05	0.2	1.8	0.02	0.052	0.009	0.015	--	0.02	0.03	0.02	0.03	0.006	0.1	--	--
800 [73]	0.12	0.25	2	--	--	--	--	--	--	--	0.55	--	--	0.02	--	--
1200 [33]	0.14	0.99	2.71	0.01	0.05	0.01	0.002	0.2	--	--	--	--	--	--	0.16	0.01

*Combined amount of Mn+Cr+Mo. n.d steel class not defined.

3.3. Dilatometry Methods

The concept behind the dilatometry is initially simple. The samples is heated up in a controlled environment and length changes are measured to indicate phase transformations. As the linear coefficient of thermal expansion (Equation 3-1) depends on the atomic structure, phase transformation can be identified by deviation from the linearity during the heating and cooling of a sample [74], [75].

Equation 3-1

$$\alpha_1 = \frac{1}{l_0} \left(\frac{\delta l}{\delta T} \right)_F$$

Where l_0 is the initial length, T is the temperature and F is the constant force applied against the expansion, usually the string strength.

Dilatometry has been extensively used in steel development {REF}. Back in 2002, Mesplont and De Cooman used it to study the effect of boron the both continuous and isothermal austenite decomposition [76], Complex-Phase steel development involves both types of austenite decomposition, as was seen in section 3.2.2.

Zhao and associates did some similar work in calculations pf phase transformation from the dilatation curves [77], with emphasis in the austenite formation.

Grajcar and associates conducted research in advanced high strength bainitic steels using dilatometric as the main technique, back in 2014 [74].

Yang and Bhadeshia used it to study the bainite to austenite transformation during heating in 1989 [78]. They also talked about the uncertainties in the use of dilatometry for the determination of the martensite start temperature in 2007 [79].

3.4. EBSD

Electron Backscattering Diffraction (EBSD) is a very powerful characterization technique that is coupled to a scanning electron microscope. It provides various types of information of crystalline samples, such as phase identification and distribution, individual grain orientation, local texture, and point to point orientation correlations [80]. More advanced use allows the detection of deformation, dislocation densities, and identification of complex microstructures. Recently, in steel applications, it has been used for identifying even the prior austenitic grains in martensitic structures, being also frequently applied to the microstructural characterization of AHSS steels [81]–[85].

The EBSD analysis is based on the acquisition and identification of the Kikuchi patterns (Figure 3.12). Kikuchi patterns were first seen and reported by Nishikawa and Kikuchi in 1928 [86]. The analysis consists of identifying the Kikuchi bands and, from the angle between the bands and indexing of the planes and directions, the structure and orientation of the grains can be determined.

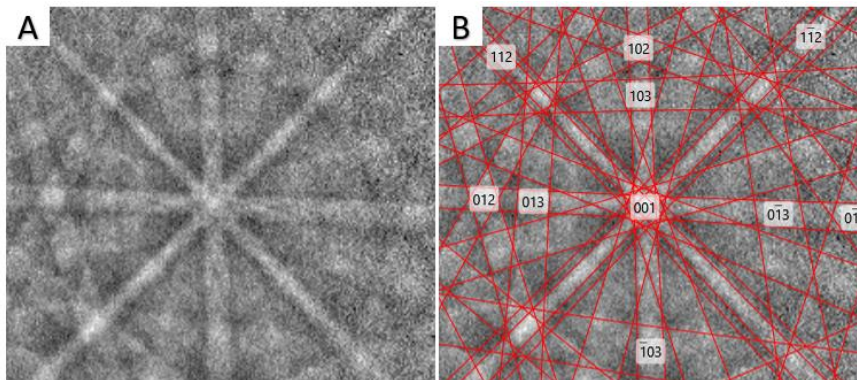


Figure 3.12 Backscatter Kikuchi pattern from the CP1100 steel ferritic region, showing a (001) zone axis reflection. A – Obtained pattern. B – Obtained pattern plus simulation.

Some factors, such as deformation and dislocation density, do affect the quality of the patterns. Therefore, when trying to identify some microconstituents by EBSD, these factors need to be taken into account. For example, Oxford Instruments, an EBSD manufacturer, does not recommend the identification of martensite as a phase during the EBSD

analysis, since the highly deformed martensite cannot be properly indexed. They recommend using only ferrite and then to segment the martensite and bainite using the pattern quality, Kernel Average Misorientation, and Grain Orientation Spread information [87]–[90]. This segmentation process will be detailed in the experimental methods section 4.7.3. Figure 3.13 shows an example of the attempt to identify a martensitic structure by the Kikuchi patterns indexing, and a comparison to the ferrite one. Figure 3.14 shows the phase ID map for this condition.

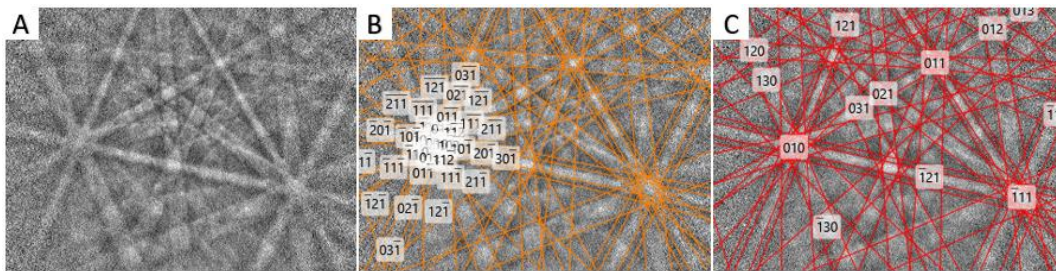


Figure 3.13 Backscatter Kikuchi pattern indexing example. A – Kikuchi pattern. B – Kikuchi pattern mis-indexed as martensite. C – Kikuchi pattern indexed as ferrite.

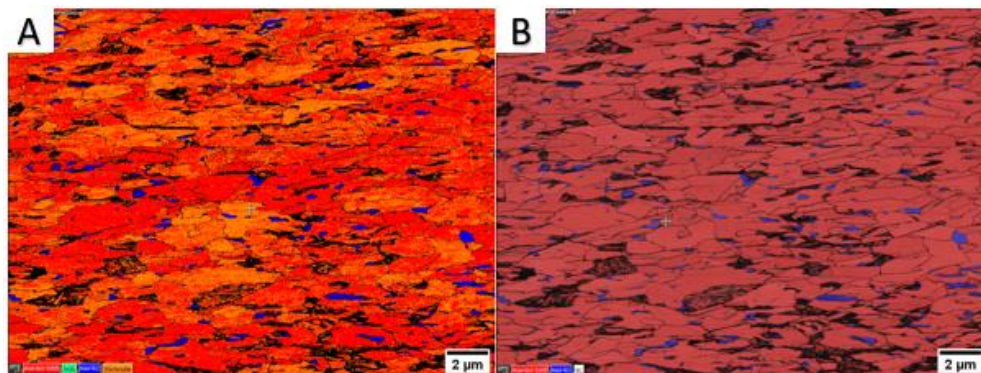


Figure 3.14 Example of phase identification of the CP1100, red ferrite, blue austenite, green cementite, orange martensite, and black zero solutions. A – Incorrect identification due to the martensite and cementite patterns additions. B – Identification with ferrite and austenite patterns.

3.4.1. EBSD Based Metallography

As it was seen, the transition from DP steels to CP ones brings a more convoluted microstructure. One of the biggest problems has become the inability to deconvolute, understand, and mostly quantify the new

microstructures. Conventional methods of metallography are incapable of such a feat. One of the options to solve this problem is the EBSD technique.

Garcia *et al.* [91] wrote about the use of Image Quality (IQ) to identify microconstituents like bainite or martensite, based on their defect concentration. It is expected that phases and microconstituents formed at lower temperatures will have a higher dislocation density, as suggested by Bhadeshia [10]. Figure 3.15 shows the dislocation density as a function of the transformation temperature, according to Garcia *et al.* [91].

The IQ is essentially a measure of the average intensity of the Kikuchi bands when compared to the total intensity of the collected pattern [92]. This IQ is influenced by the elastic distortion of the diffracted electron beam [91]. This distortion becomes worse or more intense in more complex regions and it can be measured using the Confidence Index (CI) [92]. Based on that, the IQ can be used to directly associate different microconstituents of the steel.

Garcia *et al.* [91] collected IQ map and discarded the low IQ grain boundary, keeping the data from the grains. They then measured the histogram of the IQ image. The result was a large peak with an extended base. Mathematical deconvolution methods were then applied to the histogram that provides the quantitative values of the microconstituents. Figure 3.16 shows a peak deconvolution and the authors' identification of the different microconstituents in a HSLA steel [91].

In their work, Garcia and associates also applied this method to a DP steel. They used two different heat treatments to obtain one DP590 and one DP780. Their steel had a final microstructure with intercritical polygonal ferrite, non-polygonal ferrite, bainite and a NbCN phase that did not dissolve completely. By applying the EBSD method, they obtained the results of Figure 3.17. It needs to be noticed that recrystallized ferrite and nucleated ferrite cannot be separated by this method [91].

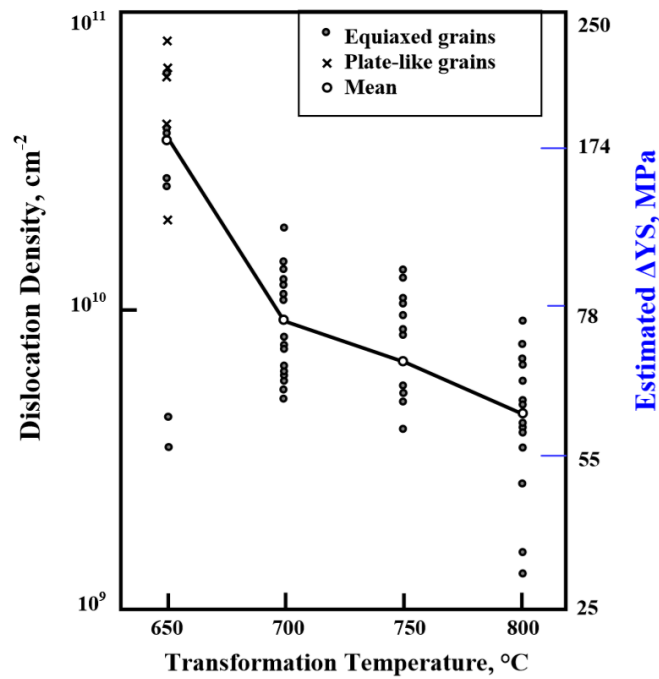


Figure 3.15 Dislocation density as a function of the transformation temperature. Reproduced from Garcia *et al.* [91].

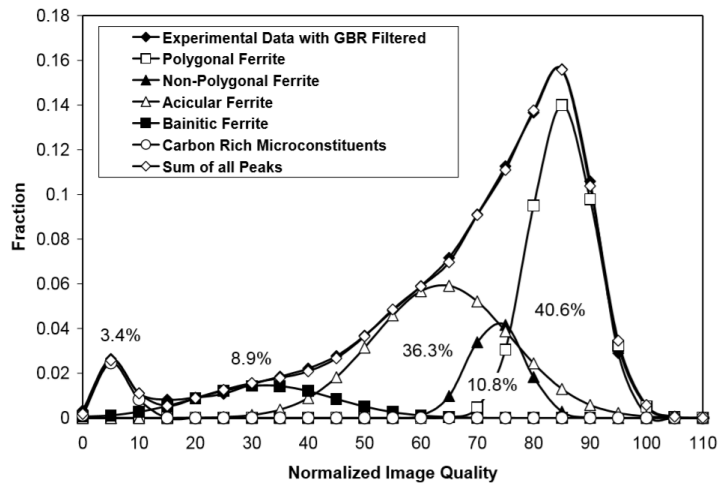


Figure 3.16 Histogram of a HSLA steel IQ and its deconvolution. Reproduced from Garcia *et al.* [91].

The same method was then applied to TRIP steels. The results can be seen in Figure 3.18. In this case, things became a little more complicated, as now they also have a bainitic microstructure as well as retained austenite. As can be seen, the bainitic microstructure has a superposition with both the ferrite and the retained austenite [91].

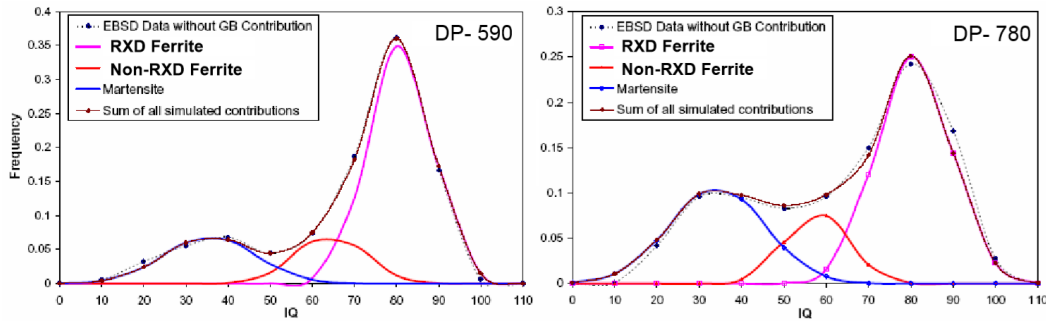


Figure 3.17 IQ histogram for the DP590 and DP780 adapted from Garcia et al. DP590 has 66.8% of recrystallized ferrite, 14.6% of unrecrystallized ferrite, and 18.6% of martensite. As for the DP780, it has 55.4%, 14.7 and 29.6% respectively [91].

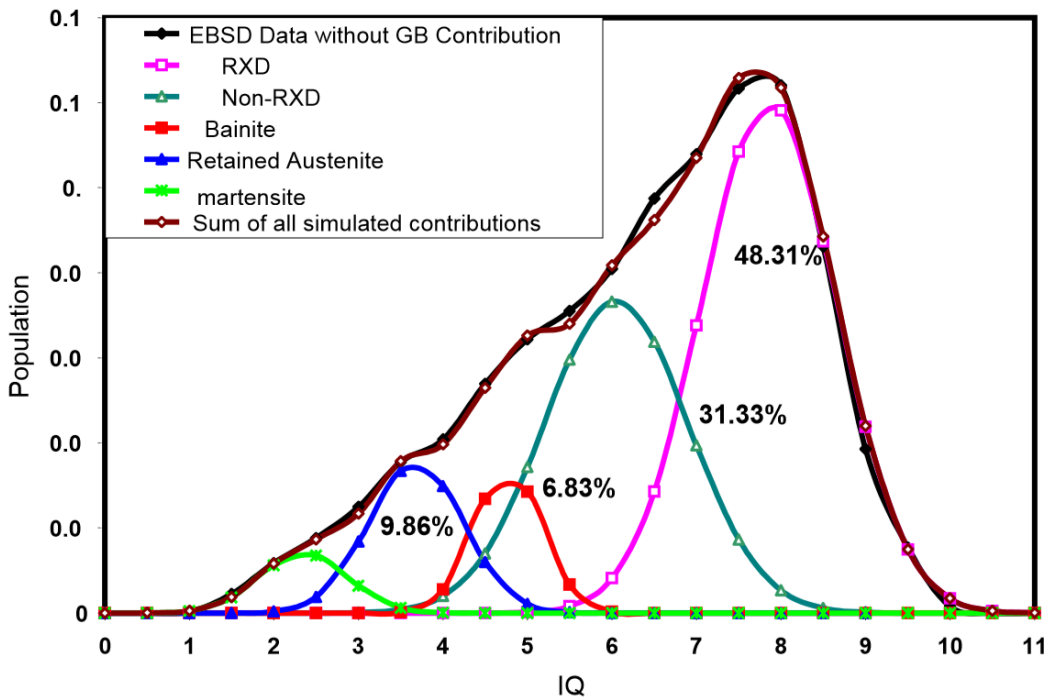


Figure 3.18 IQ histogram and its deconvolution of TRIP steel. Adapted from Garcia *et al.* [91].

By this point, it was already clear that as the microstructure became more and more complex, the peaks will tend to overlap. For CP steels the use of only IQ became unreliable. Zhao and associates [92], for example, used a combination of the Inverse Pole Figure (IPF), the boundary map, and the Grain Average Misorientation (GAM). They first took the distribution of grain aspect and deconvoluted the peak (Figure 3.19) into two peaks of polygonal ferrite and acicular ferrite. They then used the 1.5° to 5° misorientation angle as a threshold between polygonal ferrite and bainitic ferrite laths. The GAM peak was also deconvoluted into polygonal ferrite

and acicular ferrite/bainitic ferrite. Then, they used the mean grain average misorientation to find the threshold between the bainitic ferrite and acicular ferrite grains.

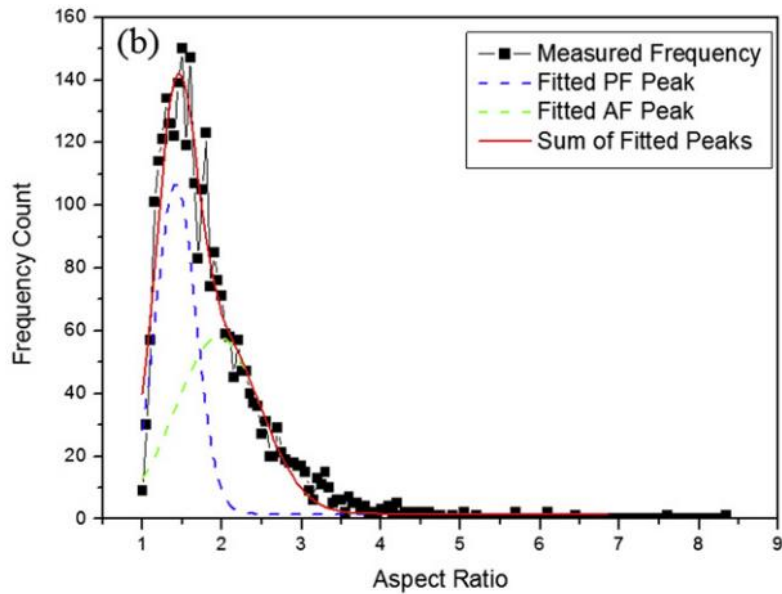


Figure 3.19 Frequency of the aspect ratio. Adapted from Zhao *et al.* [92].

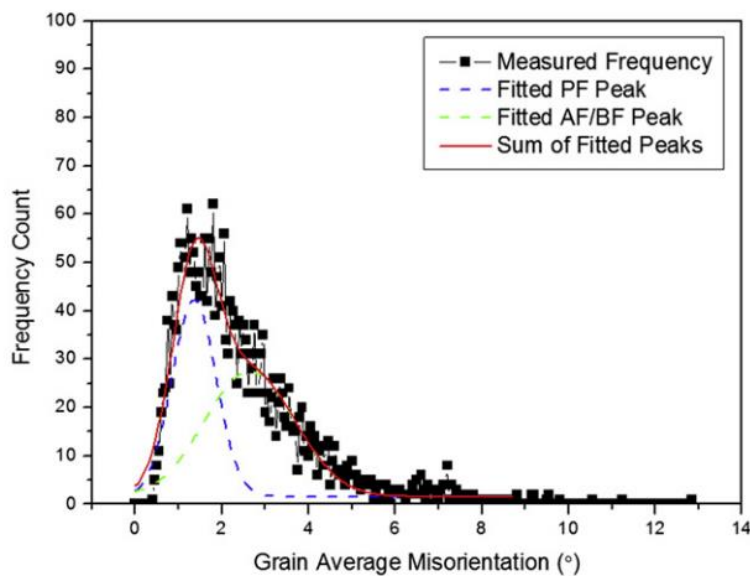


Figure 3.20 Grain average misorientation angle distribution. Adapted from Zhao *et al.* [92].

Bleck and associates [73] have combined the EBSD with electron probe microanalysis (EPMA) in order to identify and quantify a complex-phase microstructure. They used the IQ and the kernel average

misorientation (KAM) obtained in a line scan EBSD analysis together with the carbon concentration obtained from the EPMA line scan in the same region. They identified the retained austenite by its different crystal structure. The ferrite has a high IQ, low KAM, and low carbon concentration. Bainite has a high IQ, average KAM and either low carbon in bainitic ferrite or high carbon peaks in its precipitates. Martensite was identified as low IQ, high KAM, and high carbon concentration. Figure 3.21 shows one of the line scans used to define the thresholds and Figure 3.22 shows a segmented microstructure.

Although the use of KAM, GOS, and Geometrical Necessary Dislocations (GND) to identify the microconstituents in an EBSD map has been growing, the fact that those values are not constant in a single grain needs to be taken into account. One example of that can be seen in Figure 3.23, reproduced from Kadkhodapour et al. [93].

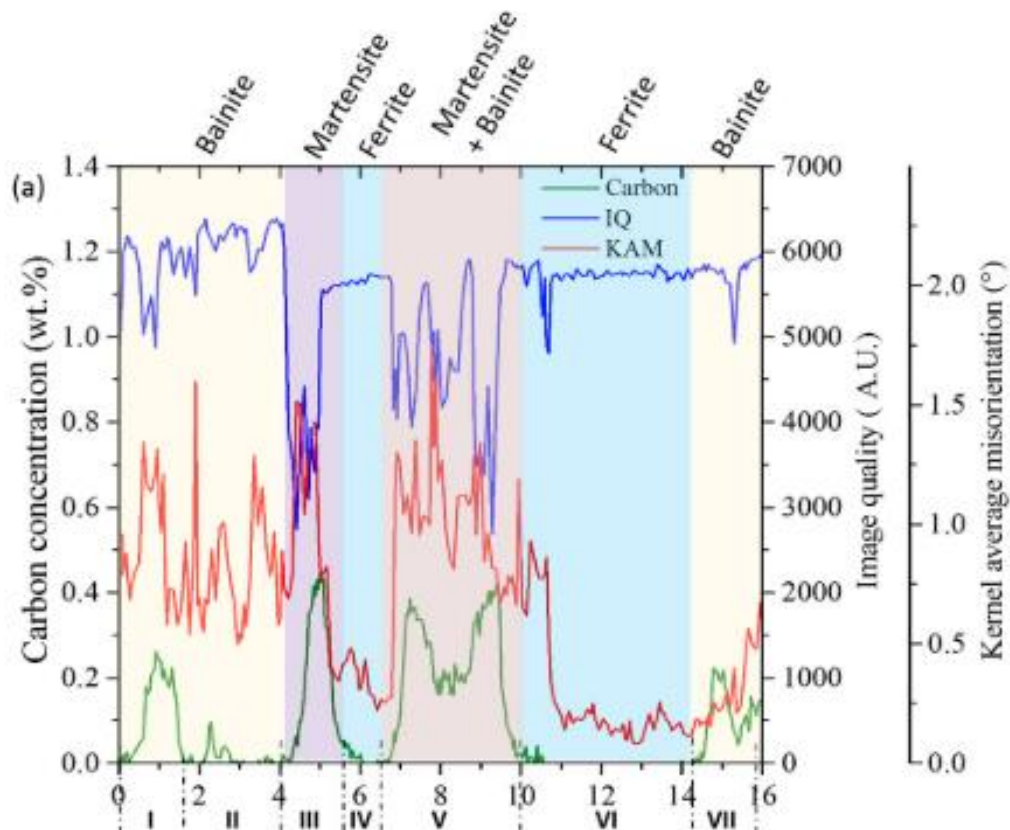


Figure 3.21 EBSD and EPMA combined method threshold using the carbon concentration, IQ, and KAM line scans. Adapted from Bleck *et al.* [73].

The use of some method of carbon quantification is a good way to identify martensite that was indexed as ferrite. De Moor and Speer [18] have applied the same principle as can be seen in Figure 3.24.

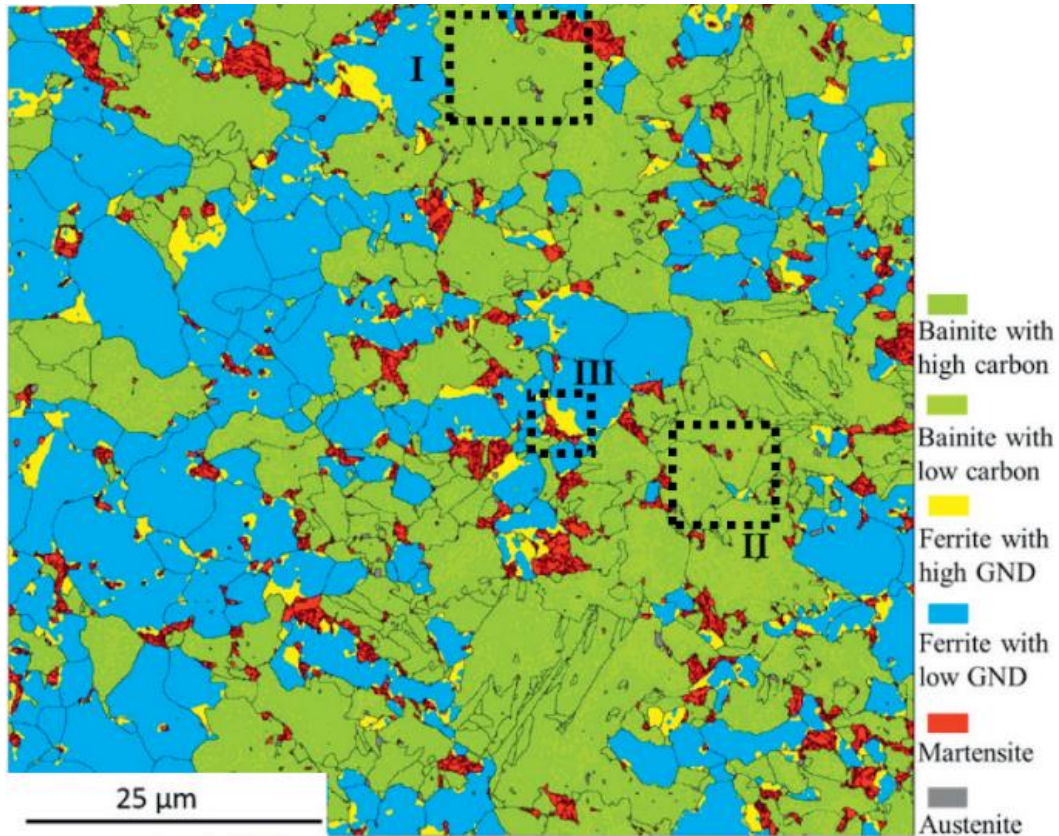


Figure 3.22 Segmented image using the EBSD, EPMA combined method. Adapted from [73].

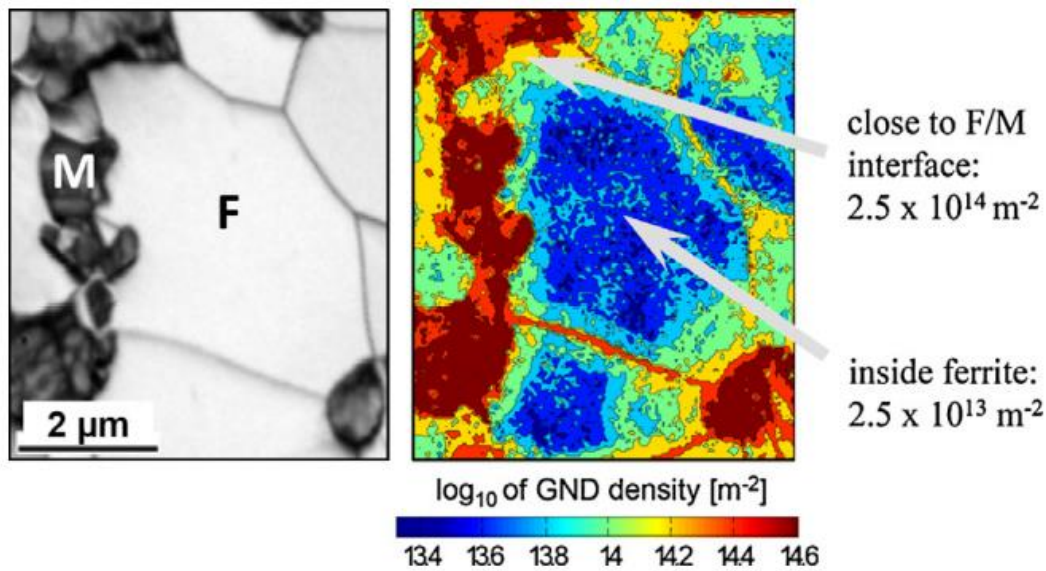


Figure 3.23 Variation of the dislocation density near the martensite-ferrite interface. Reproduced from Kadkhodapour et al. 2011 [93].

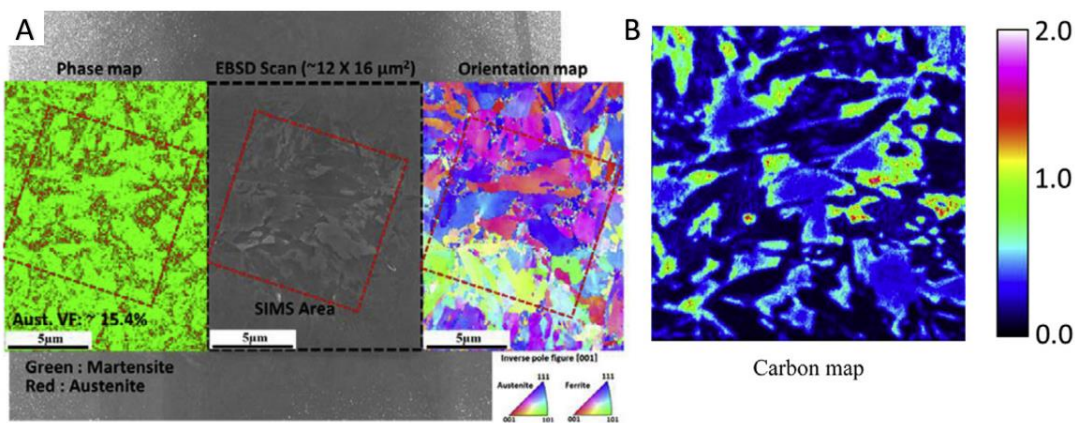


Figure 3.24 EBSD and SIMS analysis of Q&P steel. A – shows that the green area identified as martensite is indexed as ferrite. B – SIMS map showing the carbon concentration. Reproduced from De Moor and Speer [18].

3.5. AFM

Atomic Force Microscopy (AFM) is a characterization technique developed in the second half of the 80's by Binnig, Quate, and Gerber. The equipment they developed measured the force between a small sharp tip and a sample surface in scales from 10^{-8} to 10^{-12} Newton [94]. In their original design, a diamond tip was mounted on a cantilever. At the back of that cantilever, a small mirror is attached. A laser beam is pointed toward the mirror and, in a standby condition, the beam is reflected towards a

position-sensitive photoreactor. During the analysis, the interaction between the diamond tip and the sample surface causes the cantilever to bend, which deflects the laser beam. This deflection can then be measured to generate the image [94]. Figure 3.25, reproduced from McClelland and associates [94], shows the initial design published in 1987 and Figure 3.26, reproduced from Ros-Yáñez *et al.* [95], shows a more recent design. Nowadays atomic force microscopy is a much more developed tool, extensively applied in fields such as molecular biology, and with well-established literature as reference [96]–[99].

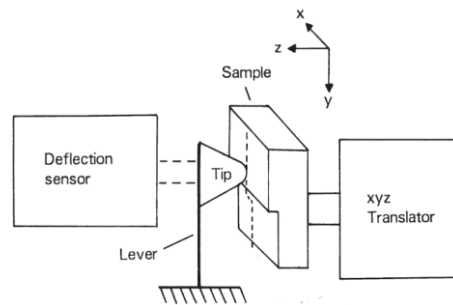


Figure 3.25 Original diagram of the atomic force microscope. Reproduced from McClelland and associates [94].

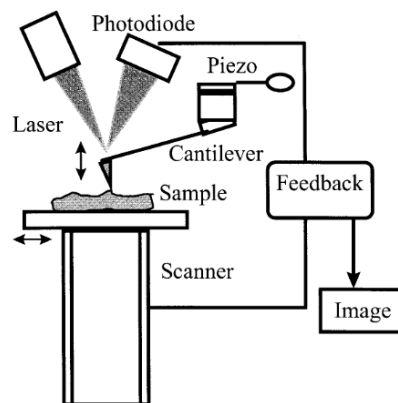


Figure 3.26 Modern diagram of an atomic force microscope. Reproduced from Ros-Yáñez *et al.*[95]

AFM has already been used for microstructural characterization of nital etched TRIP steels back in 2001 [95] when Ros-Yáñez and associates used the height and roughness to differentiate between ferrite, bainite, martensite, and retained austenite. Figure 3.27 presents an example of AFM characterization of TRIP steels, reproduced from Ros-Yáñez *et al.*[95]

and Table 3.5 shows the values of height and roughness of nital etched samples for each microconstituent measured in a C-Mn-Al TRIP steel [95].

Back in 2014, Santos and associates [100] have similarly used the AFM for microstructural characterization on low carbon steels. Not only did they use the AFM in the characterization, but also claimed that it could be an appropriate tool for continuously cooled bainite characterization. They made, the loosely translated statement:

“...unlike upper or lower bainite, formed isothermally in low-carbon steels, bainite formed in continuous cooling exhibits a variety of different fine morphological characteristics that are difficult to distinguish by light microscopy and often by electron microscopy. One of the tools that can be used to solve the limitations of these techniques is the microstructural characterization using atomic force microscopy”

Moreover, despite being different segmentation ideas, Magnetic Force Microscopy and Scanning Kelvin Probe Force Microscopy, have also been used for phase segmentation in Duplex stainless steel [101]

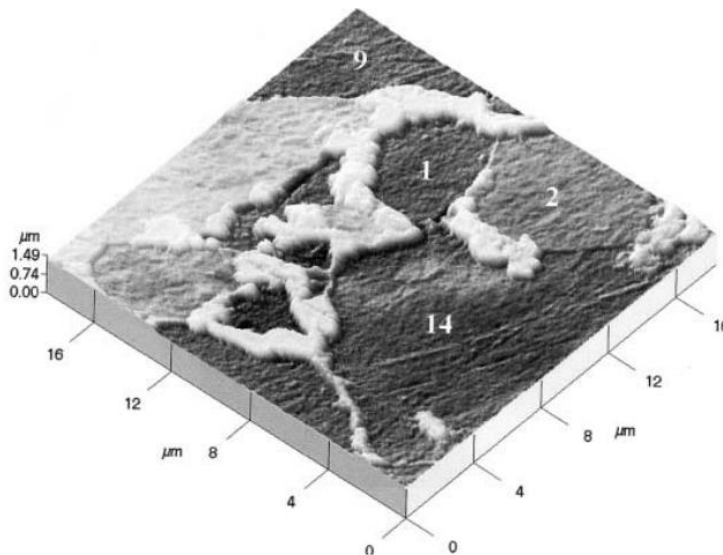


Figure 3.27 Example of AFM characterization of a nital etched TRIP steel, published by Yáñez *et al.* [95]. 1,9 and 14 are ferritic regions, 2 is a bainite region.

Table 3.5 Average roughness and height for each microconstituent according to Yáñez *et. al.* [95]

Microconstituent	Surface Roughness (nm)	Mean Height (μm)
Ferrite	16	0.150
Bainite	8	0.250
Martensite	20	0.335
Retained Austenite	5	0.300

3.6. Machine Learning and Neural Networks

The focus of the present thesis is the production and characterization of a new CP1200 steel. The use of neural networks in the characterization is important, but to minimize the amount of parallel information and to keep the focus on the microstructure, only the basics of neural networks will be explained. More detailed information about neural networks, machine, and the deep learning processes can be found in the literature [102]–[109].

The use of a machine to separate and interpret data can be seen as a massive jump for the scientific community. A well-trained machine can identify patterns that humans cannot easily see, let alone interpret and use. The first step of this process is to make sure that the machine can understand something and correctly extract the data information [109].

The idea of the use of automation for repetitive process is not a new one. Back in 1957, the Cornell Aeronautical Laboratory published a report on automaton perception and recognition [103]. Even back then, they already had the idea that an action, in this case, the act of perceiving and understanding something, was dependent on more than one input of information. In their study, they were describing a binary system, with input 0 or 1, and that had three simultaneous inputs. Figure 3.28, reproduced from Rosenblatt 1957, presents a schematic of this idea [103].

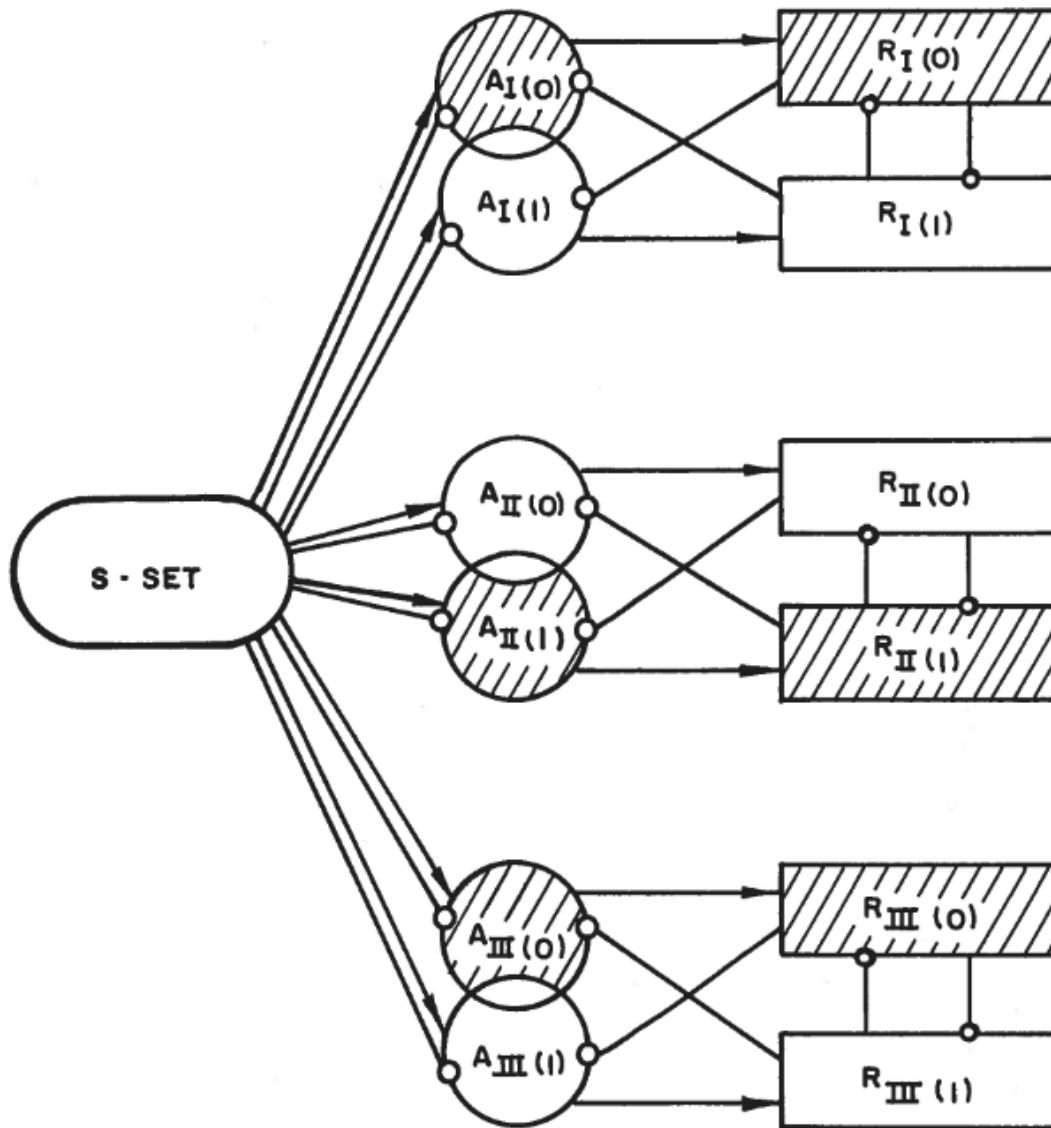


Figure 3.28 Representation of the perception as a function of 3 different inputs and a binary response. Reproduced from Rosenblatt 1957 [103].

Their representation was already very similar to the neural network functionality. In a simple explanation, they receive inputs, those inputs will pass by a hidden layer, so called because the human operator does not see this layer action. From this hidden layer, an output is obtained. Figure 3.29, reproduced from Glassner 2018 [109], presents schematics of the neural network.

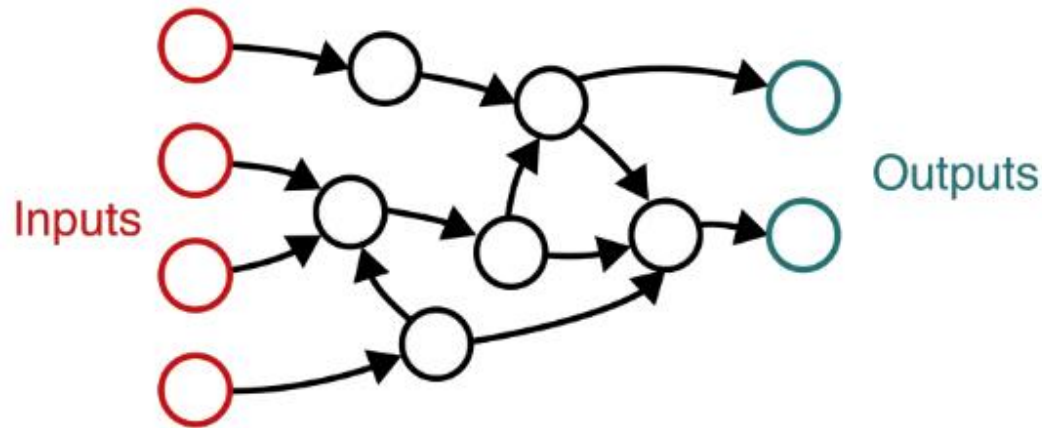


Figure 3.29 Graphic representation of a neural network. The data flows from the inputs to a final output following the path of the arrows. Adapted from Glassner 2018 [109].

Consider Figure 3.29 as an example for the segmentation of an EBSD map. This neural network has four inputs, in this case, they can be RGB color value, maximum color value, the mean color value, and the neighbors color value. The neural network will take the value of those inputs for each pixel of the image, they will be sorted by a series of combinations in the hidden layers, and then each pixel will be segmented as one of the possible outputs, for this example, the outputs can be ferrite or martensite. This would be the description of basic neural network segmentation.

4 Experimental Methods

4.1. Material

The steel under study was produced by the CSN Research Center. The composition used was based on the composition of other steels already produced by the company such as DP600, DP450, DP800, DP1000, CP800 and CP1000, along with some empirical-based modifications. The composition used can be seen in Table 4.1.

Steel plates were received from two different steps of the production process: the cold rolled and the CP treatment/Galvanizing. All the samples were from the same run of the industrial scale process, detailed in section 4.2. Some relevant mechanical properties of the CP1100 are shown in Table 4.2 [110]. The cold rolled steel plates had about 1.4 mm of thickness.

Table 4.1 Chemical composition of steel used in % wp [110].

C	Mn	Si	Cr	Al	Nb
<0.17	>1.6	0.2	>0.2	>0.015	>0.01

Table 4.2 Mechanical properties of the CP1100 [110].

YS(MPa)	UTS(MPa)	El. (%)
831	1112	9

4.1.1. Samples Identification (ID)

The samples Identification (ID) was done taking into account the last process undergone followed by the corresponding temperature or percentage of the process, such as “A50” for sample austenitized to 50% of the temperature range (ΔT), or “CP840A500” for CP steel sample that was intercritically annealed at 840 °C and isothermally held at 500 °C. Table 4.3 shows some ID examples.

Table 4.3 Examples of samples ID.

Sample ID	Treatment	Temperature / % ΔT
A75	Austenitization	75%
CP800A500	Complex-Phase	800/500 °C

4.2. Production Process and Treatment

In brief, the production of a CP steel includes a hot rolling step, a cold rolling step and an intercritical annealing, followed by an isothermal holding. On an industrial scale, a galvanizing step need to be applied as well. The present work is focused on temperatures used in the intercritical annealing and the isothermal holding. The Figure 4.1 shows a schematic design of the full CP treatment.

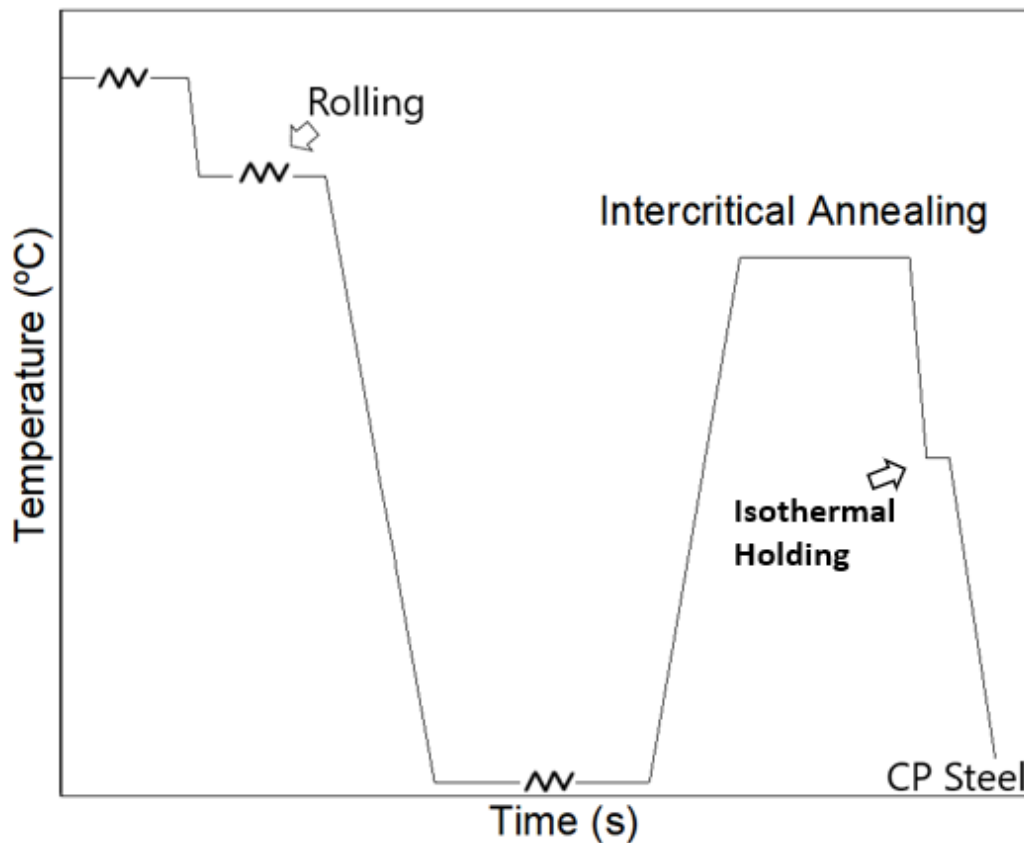


Figure 4.1 Schematic design of the CP treatment

4.3. Dilatometry

Dilatometry samples were machined using wire Electrical Discharge Machining (EDM). The samples were 10 mm long and 4 mm wide with the thickness of the plate (1,4 mm) in study and two small nodes (1 by 1mm) at each end, as shown in Figure 4.2. The nodes are there to support the sample on the dilatometer and to guarantee that it does not undergo buckling.

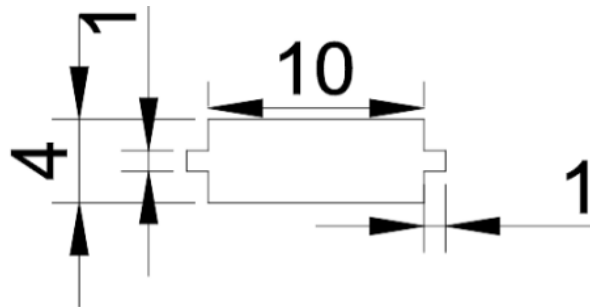


Figure 4.2 A schematic drawing of the dilatometric samples (dimensions in millimeters, mm)

A DIL 805 from TA®instruments was used to do the dilatometry tests. First, continuous cooling treatments were done to establish the CCT curve, an 10 °C/s heating rate, 5 minutes of holding followed colling rates ranging from 50 to 0.1 °C/s were used to developing the CCT diagram. Then, based on the CCT results some thermal treatments were designed and done in the dilatometer.

The transformation temperatures were determined using the points where the heating or cooling curve deviated from linearity. The derivative of the curve was used to better locate these points. An example of the derivate curve behavior near linearity changes and their use on the determination of the Ac1 and Ac3 temperatures can be seen in Figure 4.3. The final value of Ac1 and Ac3, was determined using the average value measured from all the heating curves. After developing the CCT curve, duplicate samples were produced for confirmation.

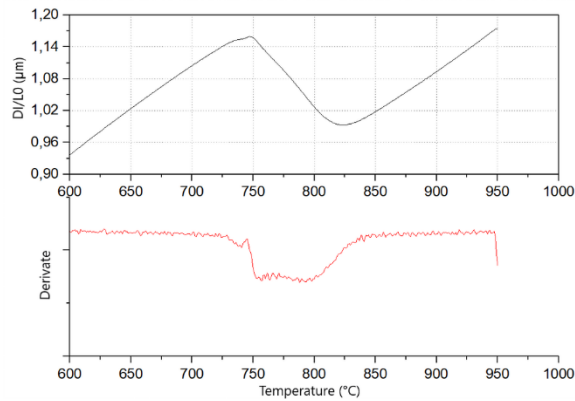


Figure 4.3 Example of the Ac1 and Ac3 determination using the derivative curve.

4.4. Mechanical Properties

The mechanical properties of the newly produced CP1200 steel were evaluated at the CSN research center. The properties in question were tensile strength, elongation, bending tests and hole expansion.

The tensile tests were done at CSN using an Instron 5585H 25t instrument with an AVE extensometer and sub dimensioned 50mm tensile samples following the ASTM E8 norm.

The bending tests were done following the ASTM E290 using a vise and a bend supporter with 3.5 times the plate thickness, as can be seen in Figure 4.4. The bending was first done to 90° for the regular test, and then extended until damage was perceived.

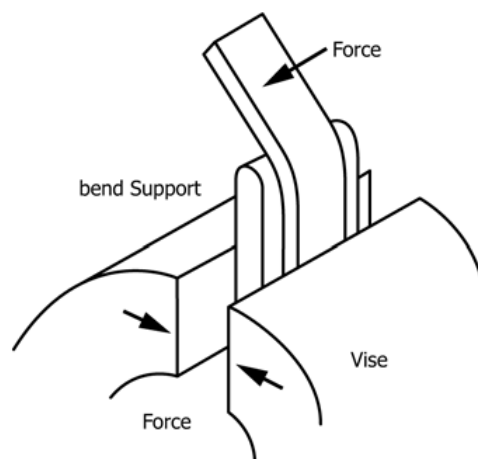


Figure 4.4 Bending test design. Private communication [110].

The hole expansion test was done following the standard ISO-TS 16630 and using a homemade device produced by the CSN research center. The test is done by punching a hole in the sample until nonuniform damage is done, that is, until a crack forms in the surface of the sample. The analysis is conducted with the help of a camera for visualization of the crack formation. The hole limit ratio (λ) is a percentual value measured by considering the initial (D_0) and the final (D_h) hole diameters, following Equation 4-1. Figure 4.5, Private communication from Tolomelli [110], shows the test schematics.

Equation 4-1

$$\lambda = \frac{(D_h - D_0)}{D_0} * 100$$

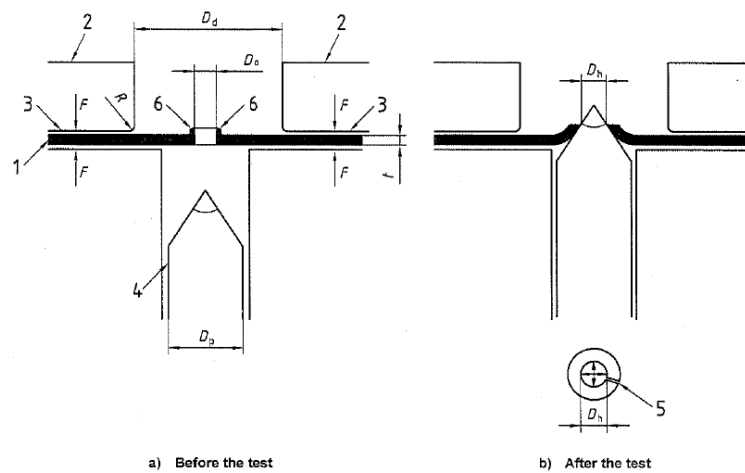


Figure 4.5 Hole expansion test schematics. Private communication [110]

Vickers hardness measurements were done on the samples as a first assessment of mechanical properties. Measurements were done at INT using a Wolpert Wilson Instruments™ universal hardness tester closed loop 930N. The testing was done following the ASTM E92 – 17 standard “Standard Test Methods for Vickers Hardness and Knoop Hardness of Metallic Materials”.

4.5. Metallography

Metallographic samples were manually prepared by grinding with SiC sandpaper FEPA designated P400, P600, P800, and P1200 followed by polishing with diamond suspensions of 9, 6, 3, 1 and 0.25 μm . The samples were then etched either with 2% Nital or using 2% Nital followed by 1% sodium metabisulphite solution.

Samples etched with Nital were used for secondary electron imaging on the SEM and samples etched with Nital followed by a 10% Sodium metabisulphite water solution were used for light optical metallography. This is a color etching method that results in a whitish ferrite, brown/dark brown martensite/bainite and a black retained austenite. Several color etchings have been reported in the literature, but Hairer and associates showed that this is the best option for a CP steel [69]. The metabisulphite etching did not change the SEM results as can be seen in Figure 4.6. Vilela etching was later used to reveal the prior austenite and consequently measure it.

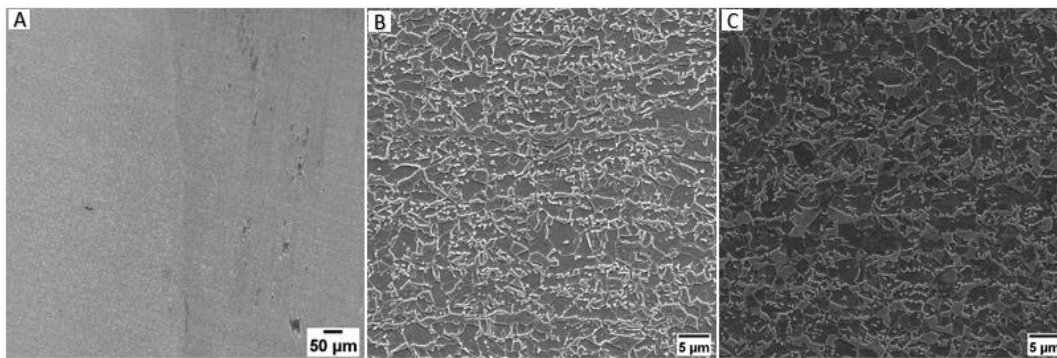


Figure 4.6 Difference between the Nital and the Nital + sodium metabisulphite etched regions on the CP840A500 seen by SEM. A – Interface of the two etchings. B- Nital etched region. C – Nital + sodium metabisulphite etched region.

4.5.1. Light Optical Microscopy

Light Optical Microscopy (LOM) was done at the DIEMP division of INT, using an Olympus BX51M with the software Olympus Stream Essentials. LOM image was used for phase ID through color etching. The segmentation process is discussed in section 4.10.

4.6. Atomic Force Microscopy (AFM)

The AFM characterization was performed using a Bruker Multimode-8 AFM in contact mode. The samples used were polished and nital etched. The Gwyddion open-source software was used to process and analyze the AFM images.

The characterization done in CP1100 and CP1200 followed the one proposed by Ros-Yáñez and associates [95]. But since the complex-phase is a different kind of steel, with a different microstructural distribution, and a much smaller, almost negligible, amount of retained austenite, it would be unreasonable to expect a perfect reproduction of the etching used by Ros-Yáñez and associates. Therefore, making the values for height and roughness reported by Ros-Yáñez and associates, misleading when applied at complex-phase steels. Considering that, new threshold values of height and roughness for each different region needs to be established for the complex-phase steel. These new values were obtained using the Gwyddion open-source software. Figure 4.7 shows an example of the regions selected for the analysis.

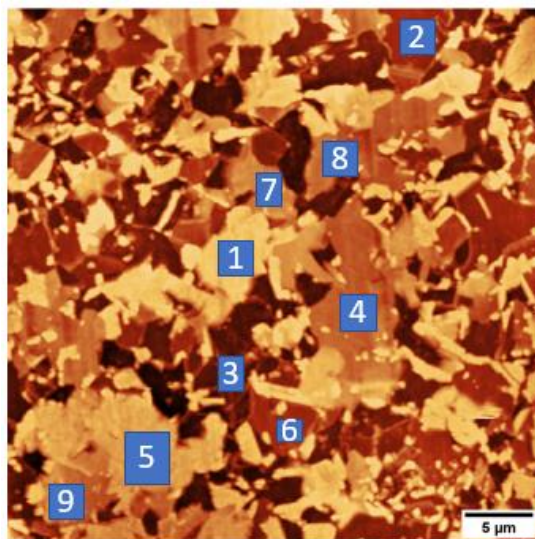


Figure 4.7 Example of surface roughness analyses sampling on an AFM image, numbers mark measured regions

During the AFM characterization the direction of the scanning is important as there is a distinct possibility of a nonlinear or homogeneous background height through the sample. That is even more important as the scanned area increases in length. In those cases, is important to do a background correction prior to the phase's segmentation. Figure 4.8 shows an example of AFM characterization on a complex-phase steel. In A, the sample was not background corrected, you can see to regions pointed by two blue arrows that seems to be at the same height. In B, you can see the same image, now with background correction; it became clear that the regions denoted by the arrows are not at the same height.

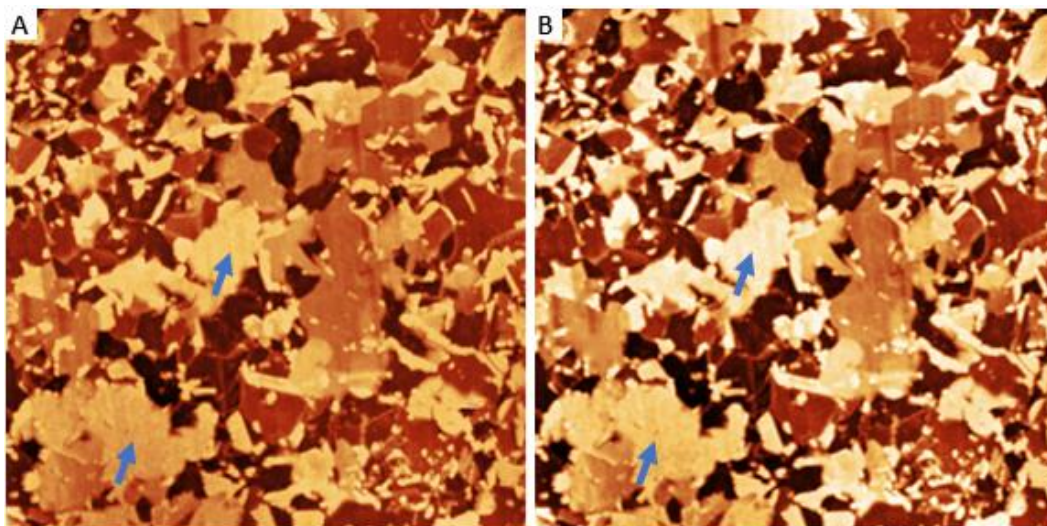


Figure 4.8 Example of the effects from background correction. A – image without correction. B – Corrected image. Blue arrows point two regions that would be incorrectly segmented without the background correction.

4.7. Scanning electron microscopy / EBSD

Scanning electron microscopy (SEM) was done at three different research centers: 1) Centro Brasileiro de Pesquisas Físicas (CBPF), using a Jeol 7100FT equipped with an Oxford Energy Dispersion Spectroscopy (EDS) and an Electron Backscattering Diffraction (EBSD) Nordlys Max2 detector; 2) Colorado School of Mines, in the Electron Microscopy Lab (EM Lab) using a Jeol 7100FT equipped with an EDAX Hikari Pro EBSD. The EBSD post analysis was done using the AZtec software from Oxford and

the OIM software from EDAX. 3) PUC-Rio using a Tescan Clara also equipped with an Oxford Energy Dispersion Spectroscopy (EDS) X-Max 80 and an CMOS EBSD camera model C-NANO.

EBSD was initially done on 20 by 20 μm regions. Higher magnification was used in particular cases to better identify the boundary regions. The 20 by 20 size was chosen based on the average 2 μm grain size and on the limited size for lift-outs. Later, larger areas were used to maximize the quantification capabilities.

4.7.1. EBSD Sample Preparation

The sample preparation for EBSD can be challenging. During the course of this research several sample preparation routes were used.. As EBSD maps were obtained with different sample preparations, all the used preparation routines will be reported.

The first analyses were carried out following the secondary electron imaging. Because of that, the samples used were previously polished and etched as described in section 4.5. These samples were then polished again in an autopolisher with 1, 0.5, 0.25 and 0.05 μm diamond colloidal suspensions at Colorado School of Mines. The final polishing was done in a vibratory polisher with 0.02 μm colloidal silica suspension for 2 hours. Vibratory polishing was done both at Colorado School of Mines and at the *Instituto Militar de Engenharia* (IME). This preparation line produced a well polished surface, and the literature reports it as one of the best methods [111], [112]. It should be mentioned the importance of the specimen preparation for the secondary electron imaging process, that is, if they were not ground, polished and etched as described prior to this EBSD preparation, the results would not be as satisfactory. That became especially evident on the deformation analysis by KAM and GOS. The ground samples needed to be etched at least once prior to the final polishing in order to minimize artifact deformation.

A second line of preparation was used in conditions where the vibratory polisher was not available. This preparation was similar to the

previous one, but it used manual instead of automatic polishing. In this case, after the mechanical polishing to $0.25\ \mu\text{m}$, the sample was hand polished with the $0.02\ \mu\text{m}$ colloidal silica suspension and finished with two seconds of etching in a 0.5 % Nital solution. An example of the sample surface obtained with this preparation can be seen in Figure 4.9. Despite not being as good as vibratory polishing, this method provides the second-best polish for this particular kind of sample.

And last, electropolished samples were also tested. Regular electropolishing was not successful as the samples were easily oxidized yielding inconsistent results. On the other hand, samples prepared with tenupol 5, specifically for TEM, presented exceptionally good conditions for EBSD. However, this use was limited, because TEM sample preparation is long and troublesome, and if used for EBSD, it can no longer be used for TEM. Besides that, the sample size is limited, and the lamination direction can be easily missed if the microstructure does not make it clear (the case for some treated samples). With all that considered, some samples that were initially prepared for TEM, but that had a hole with thick edges or that were not positioned near the center of the sample, were used for EBSD.

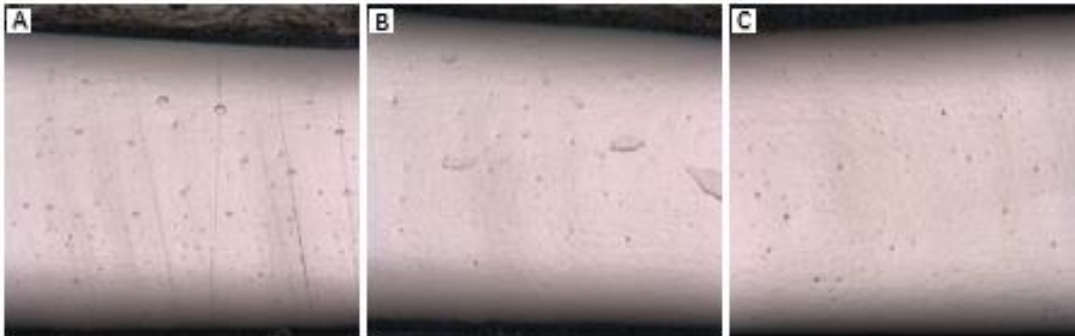


Figure 4.9 LOM of the prepared samples. A – polished $0.25\ \mu\text{m}$. B – Polished at $0.02\ \mu\text{m}$. C – etched at 0.5 % Nital for 2s.

Surface cleaning is another important factor during sample preparation. The colloidal silica tends to be adsorbed on the sample surface and, being an insulating particle it may negatively influence the EBSD. Figure 4.10 shows a prepared sample with SiO_2 particles on the surface. Residue can also be a problem after the two second etching; in the literature, authors

have reported negative impacts on pattern quality due to etching residue [111].

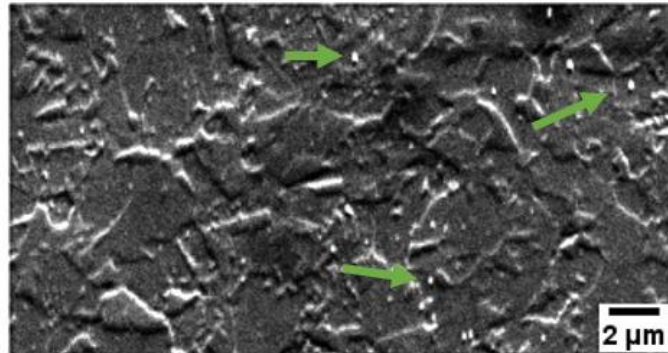


Figure 4.10 Secondary electron image of a EBSD polished sample with channeling contrast. Green arrows point to SiO₂ residue over the sample surface.

4.7.2. EBSD Data Cleaning

Several reasons can lead to a misindexing or non-indexing of a point during a EBSD analysis, such as pits and small precipitates on the surface [113], or even the residues discussed in the sample preparation section. Because of that, the EBSD data is usually subject to a step called “cleaning”. This step is used to replace regions where the Kikuchi patterns were not identified. They are, essentially, algorithms that consider the neighbors of the misindexed or non-indexed point to try to “guess” the proper indexation [114]. For example, Figure 4.11 shows the effect of cleaning in a band contrast plus inverse pole figure plus grain boundary map and Figure 4.12 shows an example of the same cleaning on the KAM plus GOS plus grain orientation spread.

These cleanings are many times performed for “aesthetic” reasons, producing a more appealing image [114]. But this cleaning needs to be done carefully to avoid mistakes or otherwise straight manipulation of data. Laureys and associates recommend no cleaning other than the exclusion of areas with less than 0.1 of confidence index [115]. Petrov and associates used a similar method but with a neighbors “zero solution” exclusion algorithm [116].

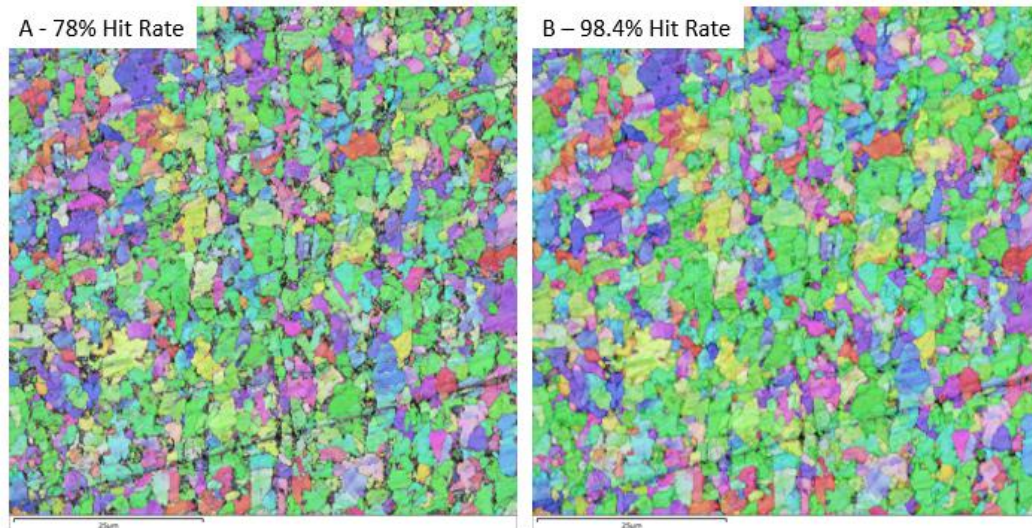


Figure 4.11 Example of the effect of cleaning on a fast obtained Band Contrast + IPF + Grain boundary map. A – 78% hit rate non cleaned map. B – 98.4% cleaned map.

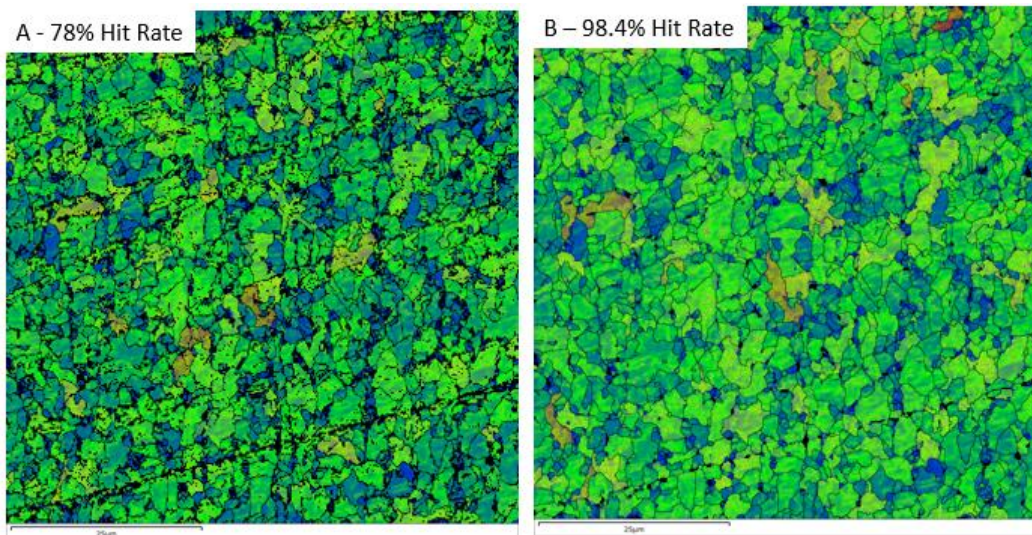


Figure 4.12 Example of cleaning on a KAM + GOS + Grain boundary map. A – 78% hit rate non cleaned map. B – 98.4% cleaned map.

In the present thesis, the cleaning process used was the one recommended by Oxford instruments at their “effective EBSD data processing using AZtecCrystal” webinar, a process used specifically for an AHSS steel. Most of the processing used in the EBSD analysis followed the EBSD vendor suggestions [87]–[90], [117], [118]. This cleaning process consisted of an automatic cleaning using the “exclude void based on band contrast” option, followed by a “remove zero solution with three neighbors” algorithm. The effect of this cleaning process can be seen in Figure 4.13,

going from no cleaning at all to excessive cleaning. In Figure 4.13D the zoomed area shows a misidentified region due to the wrong cleaning; the black arrow points to one clear mistake.

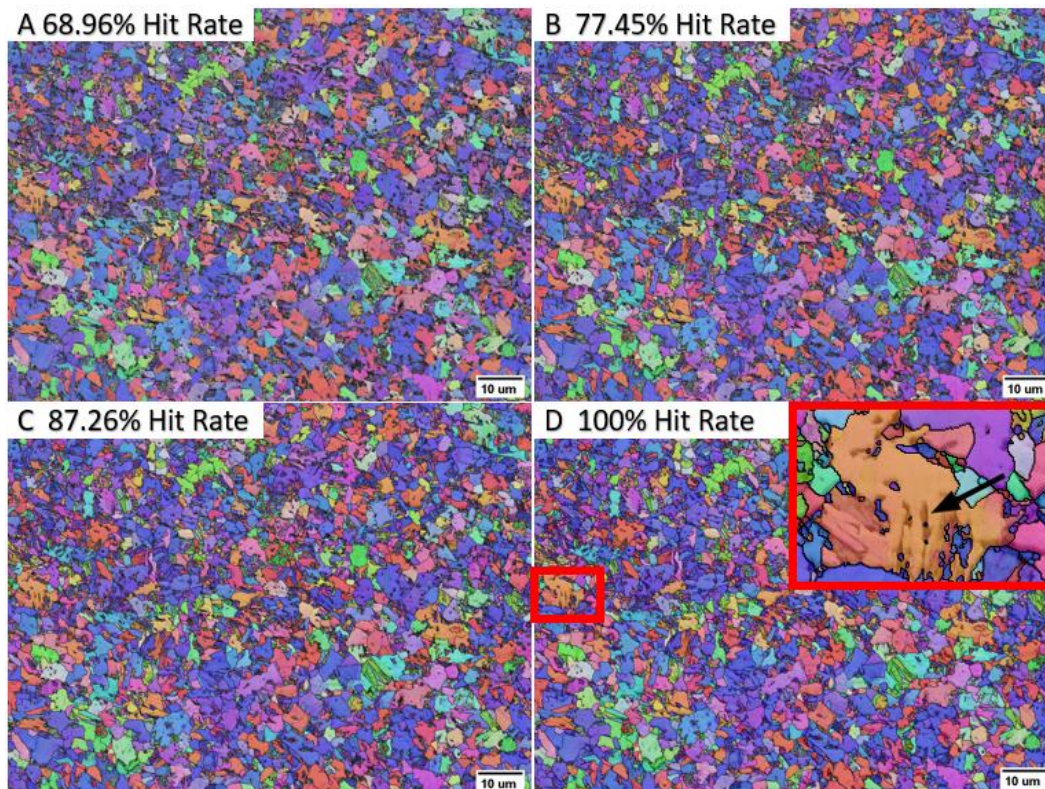


Figure 4.13 Example of the cleaning process step by step. A – Non-cleaned original image. B – Auto-cleaning with band contrast void exclusion image. C – Zero solution removal algorithm using three neighbors. D – 10 iterate zero solution removal using three neighbors, black arrow in zoomed region shows a misinterpretation of the results.

There are some alternative cleaning methods, such as the use of morphological dilation operation on the segmented regions: this cleaning needs to be done after the segmentation and on a phase-by-phase basis. It has been applied in the literature for the classification of TRIP steels [119]. Another cleaning option is the exclusion of small grains or areas, such as the one used in complex microstructures by Zhu and associates [120], where they disregarded regions with less than $0.5 \mu\text{m}^2$.

4.7.3. EBSD Processing, Analysis and Segmentation

After being collected, the EBSD maps need to be processed and segmented. This segmentation process was done by two similar processing routes. The first one, using the FIJI software to directly process the EBSD maps. The second option was to use the Oxford AZtecCrystal software. In both cases similar neural networks were used for the segmentation.

The first consideration in the EBSD analysis was the phase identification done using the indexed Kikuchi patterns. This phase identification did not differentiate between ferrite and bainite. But by considering the ferrite quantification obtained by LOM, it was possible to calculate the difference and estimate the bainite amount, as seen in Equation 4-2. This process did not produce a segmentation of the image, but gave a fast bainite quantification; it also was a good way to check if the latter segmentation was correct. Following that the calculated bainite could be subtracted from the LOM martensite/bainite amount in order to obtain the martensite content, as explained in Equation 4-3.

Equation 4-2

$$EBSD_{ferrite} - LOM_{Ferrite} = Bainite_{calculated}$$

Equation 4-3

$$LOM_{martensite/bainite} - Bainite_{calculated} = Martensite_{calculated}$$

The next step in the EBSD processing was the analysis of the pattern quality. EDAX EBSD analysis produces one kind of pattern quality, the Image Quality (IQ) and Oxford EBSD produces 2 kinds of pattern quality maps, Band Contrast and Band Slope. Band Contrast (BC) is a map derived from the Hough transformation, favoring an average of the total quality of the Kikuchi patterns. The Band Slope (BS) is also derived from the Hough transformation, but it favors the intensity gradient. Thus, BC better reveals the difference between each grain, and BS reveals the grain boundary. It is also possible to combine both maps to produce a better identification of the

phases. Figure 4.14 shows an example of those 3 possible pattern quality maps and their respective histograms. The histogram of the combined map makes clear the two peaks that can be used for an easier segmentation.

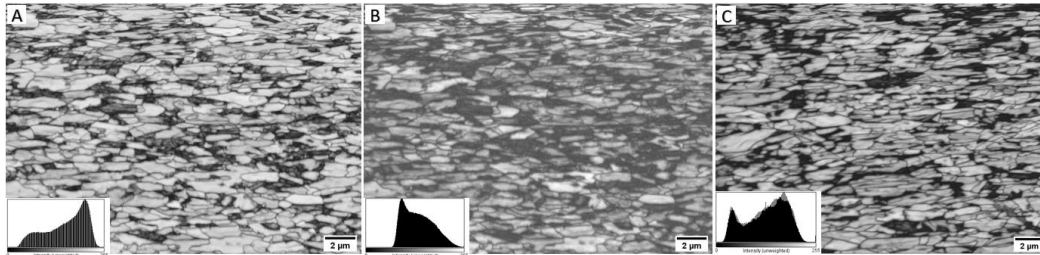


Figure 4.14 Pattern quality maps and their respectively histograms. A – Band Contrast. B – Band Slope. C – Band Contrast + Band Slope.

Before doing any of the map analyses, it was necessary to establish the threshold angle used to define the grain boundaries. Otherwise, regions with low grain boundary angles may be identified as a single region, as illustrated by Figure 4.15.

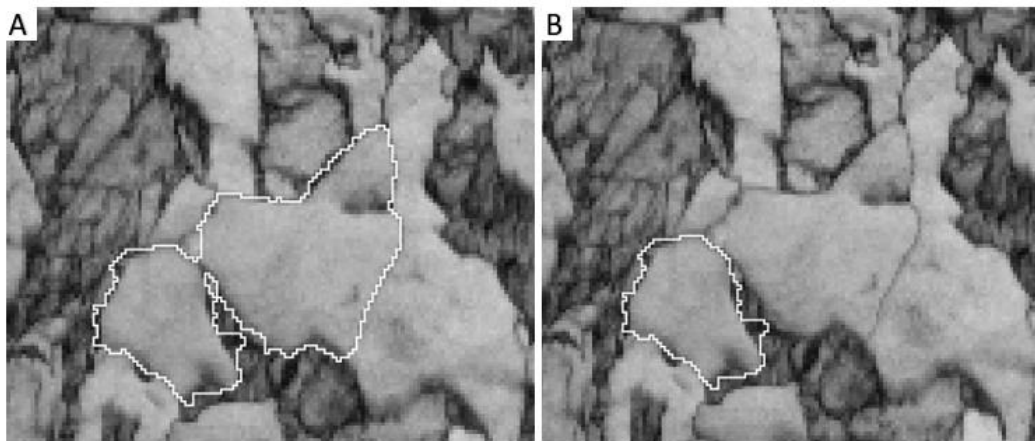


Figure 4.15 Example of a grain misidentification. A – Incorrect identification. B – Correct identification.

The pattern quality maps were used for the segmentation of the martensite. As previously mentioned in the section 3.4.1, due to its high dislocation content, the martensite will have a low to zero pattern quality. Therefore, regions with low pattern quality were segmented as martensite. This process was done first using the FIJI WEKA plugin and will be detailed in section 4.10, image analysis.

The second microconstituent to be segmented was the austenite. Its segmentation was done using the phase identification map. The segmentation was done with FIJI using the command “Color Threshold” followed by an “8 bits” conversion and a regular “Threshold”.

The last step was the segmentation of bainite and ferrite. This segmentation was done using the KAM plus GOS map. When those maps were overlaid the deformed grain became more evident, as green and red areas. These deformed regions were then considered bainitic. In the FIJI software, the process was done by converting the combined map into an 8 bit image, and then segmenting using the “threshold” command. During the 8 bit conversion, all the ferrite is given the same color gray value, making the segmentation much easier. An example of the process can be seen in Figure 4.16 and the histogram showing the concentration of the ferrite can be seen in Figure 4.17.

After that, the segmented maps were added up together. The “image to stack” and “stack to RGB” commands were used to generate a color segmented map.

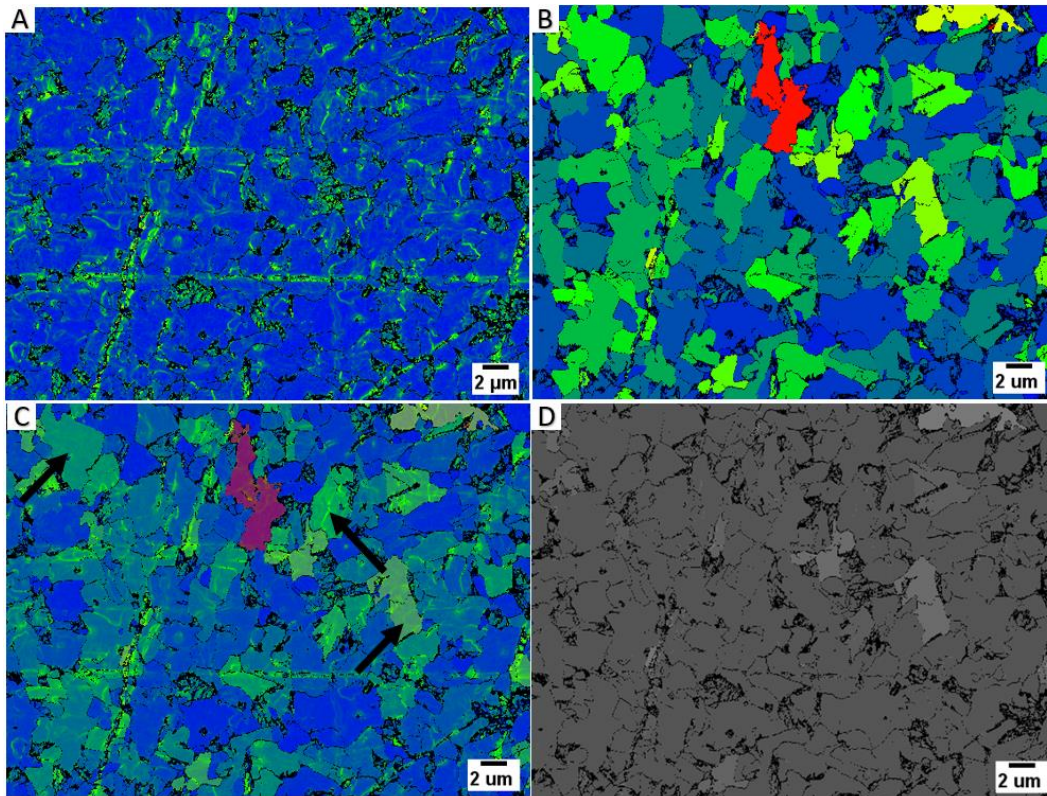


Figure 4.16 Example of segmentation of ferrite and bainite using the FIJI software and the KAM+GOS map. A – KAM map. B – GOS map. C – KAM + GOS map. D – Gray scale of the KAM + GOS map. Black arrows point to bainite regions.

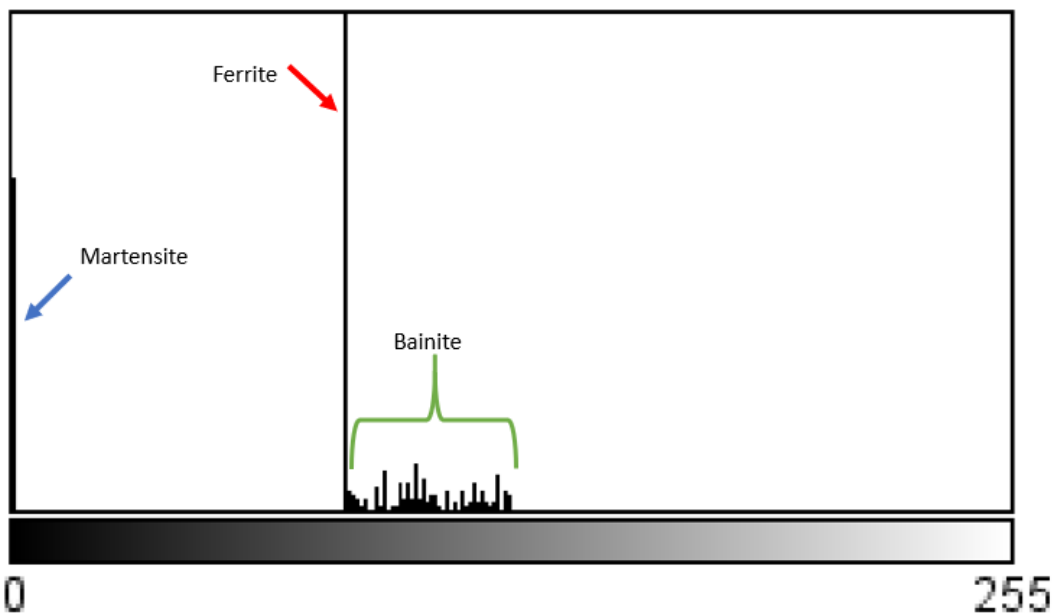


Figure 4.17 Histogram of the 8 bits converted image. Blue arrow shows the martensite peak, red arrow the ferrite one and green the bainite.

Later, the AztecCrystal software was also used for the microconstituent segmentation. It was possible, in this case, to directly combine the phase id information, together with the band contrast, KAM and GOS maps to training of the neural network. This process was much faster than the FIJI one. The grain section tool allows an easier selection of training regions. The trained network can be easily reapplied for other maps. The segmentation process runs constantly, so any change on the training regions will provide a new segmentation instantly. This aspect is interesting with regard to refining the neural network, allowing mistakes to be more easily seen.

Also, on the AZtecCrystal, a line scan can be done over a mapped region for comparison of the BC, KAM and GOS values in different grains. Figure 4.18 shows an example of that use. In the figure, the red arrows point to the high BC, low KAM and low GOS ferrite; the black arrows point to the lowest BC, low KAM and low GOS martensite; and the green arrows point to the high BC, high KAM and high GOS bainite region.

Even when using this method, there is a need to take extra care on determination of the threshold of deformation (KAM and GOS) that defines a bainitic region. Otherwise, a misidentification of the map can happen. Figure 4.19 presents some examples of misidentification. The value for the KAM and GOS threshold was determined map-by-map. That was done to avoid artifacts from the sample preparation.

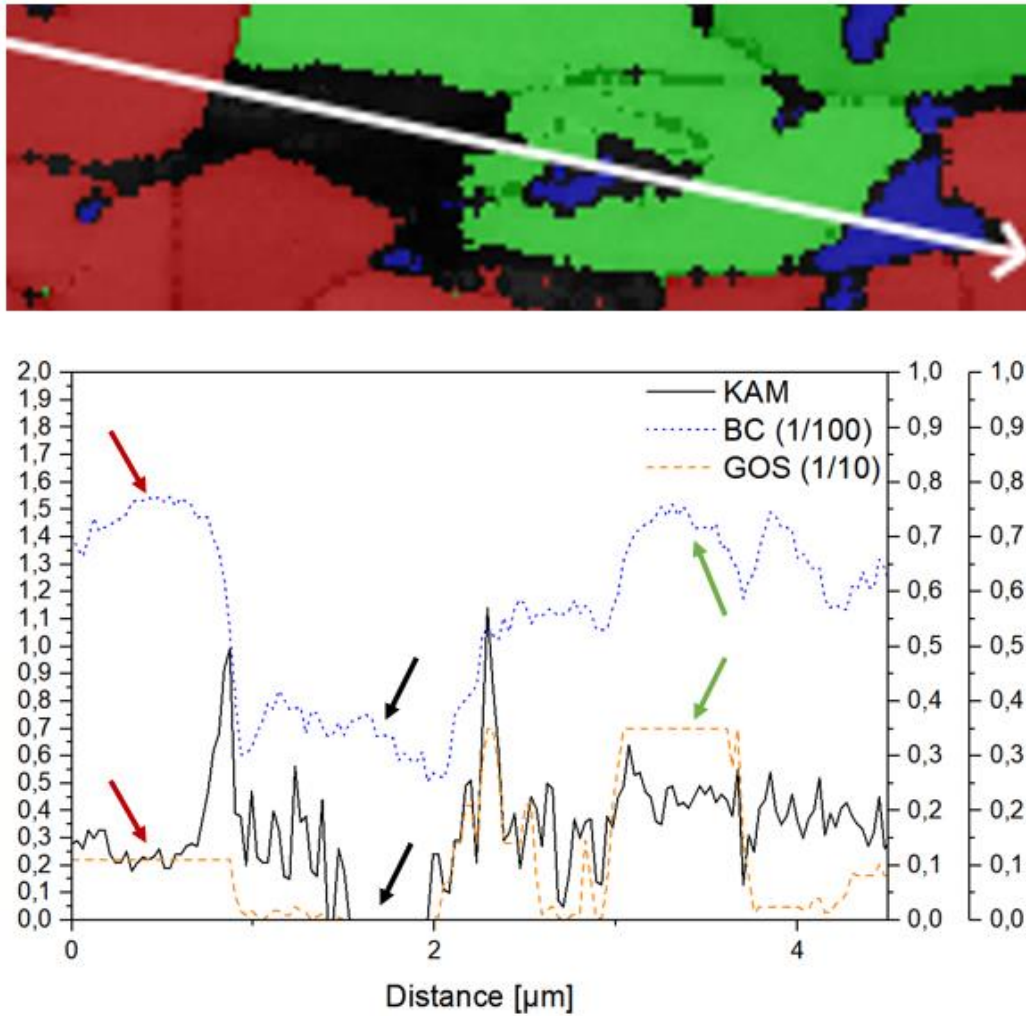


Figure 4.18 Line scan done over the EBSD map of the CP100 steel. The segmented image was a red ferrite, green bainite, black martensite and blue austenite. The blue dashed line is the BC, the black solid line is the KAM and the yellow dashed line is the GOS.

To sum up, in the AZtecCrystal the final microconstituent segmentation was done using a combination of pattern quality, phase identification, KAM and GOS analysis. The martensite was segmented using zero solution regions directly from the Band Contrast map. Retained austenite was segmented using the indexed patterns in the phase identification map (protect phase). This map also carried a ferrite segmentation, but the bainite was segmented together with it. To deconvolute them, deformation data from the KAM and GOS maps were used. The higher deformation regions were deemed as bainite, and lower deformation regions were considered as ferrite. The screen of the AZtecCrystal “Classify” tool can be seen in Figure 4.20.

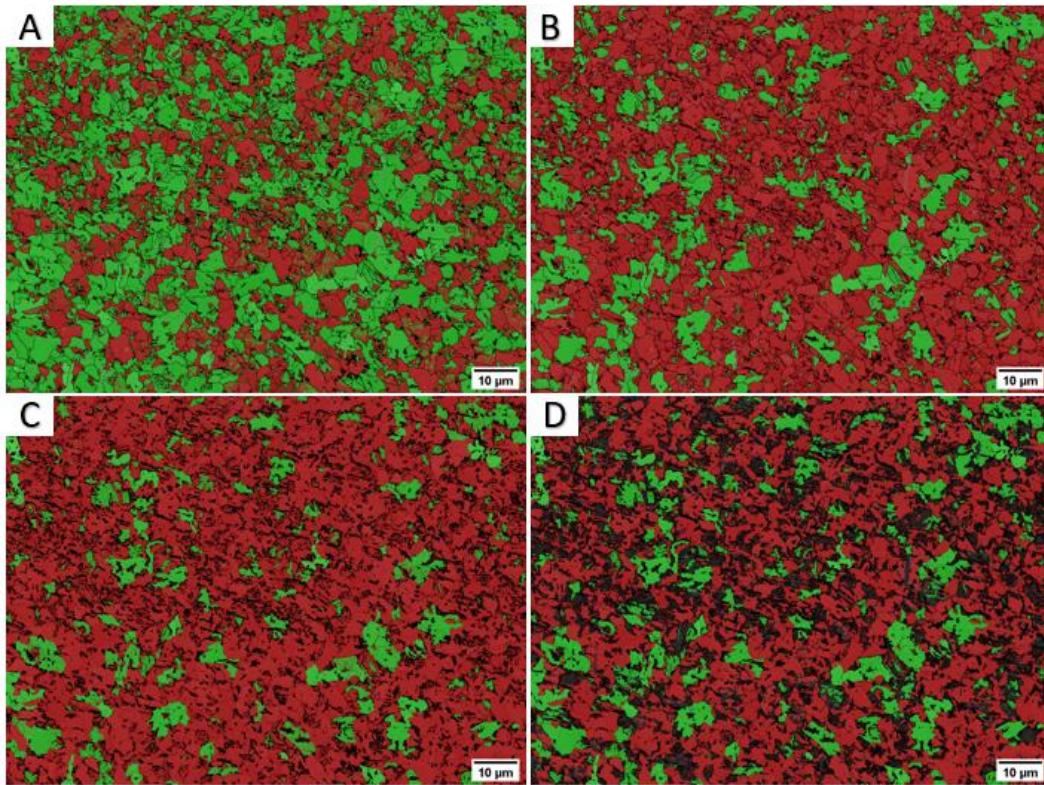


Figure 4.19 Example of misidentification of the microstructure in AZtecCrystal. A through D presents different segmentation results for the same EBSD map.

PUC-Rio - Certificação Digital N° 1712467/CA

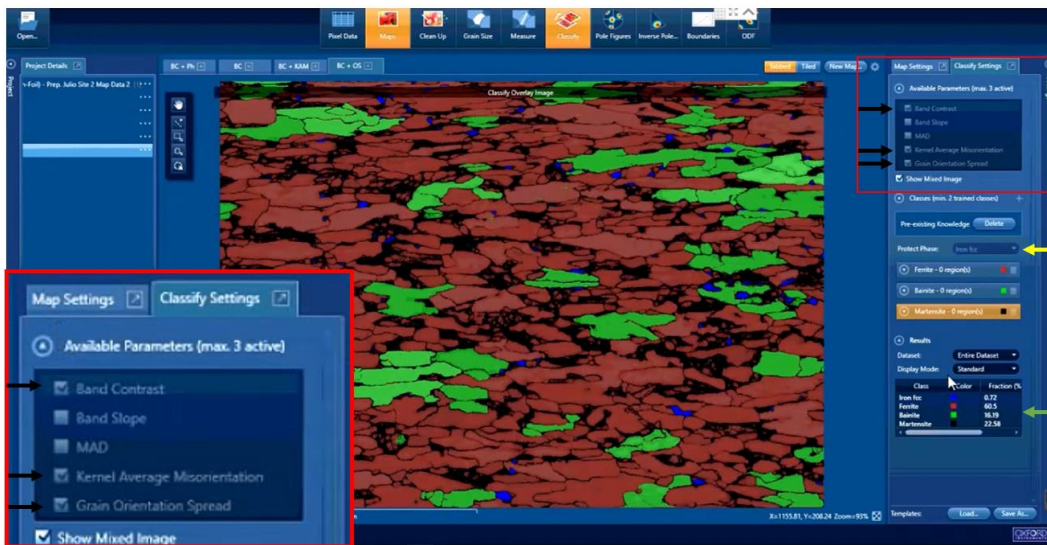


Figure 4.20 Window of AZtecCrystal software. Black arrows point selected maps used for segmentation, as seen in zoomed area. Yellow arrow shows the protect phase FCC. Green arrow shows the quantification results.

4.8. Transmission Electron Microscopy

Transmission Electron Microscopy (TEM) was done at the Colorado School of Mines EM-Lab using a FEI Talos F200X and at CBPF using a Jeol 2100F.

Dark field imaging was done to identify precipitate and martensite/bainite morphology. Electron Diffraction was done to identify the phases.

TEM samples were prepared either by grinding and polishing small pieces to 150 μ m and then cutting 3mm disc using a disc punch and then electropolishing in a Tenupol 5 using a 10% perchloric acid in methanol. The electropolishing was done at -20 °C to prevent any explosive reaction from the solution.

Due to the limited amount of material (dilatometry specimens), some TEM samples were prepared by FIB liftout.

4.9. Focused Ion Beam

A Focused Ion Beam (FIB) Helios 600 from FEI was used to extract TEM samples from the small size dilatometry specimens. In order to do the liftout, samples had to be first very well polished, so as to make easier to choose the “Region Of Interest” (ROI).

In the ROI a 0.5 μ m layer of platinum is deposited using the electron beam (Figure 4.21 A). Then, after a 52° inclination a 3 μ m platinum layer is deposited with the ion beam. The region around the ROI is excavated, a probe is welded to the corner of the ROI (Figure 4.21 B). The lamella is lift (Figure 4.21 C) and then welded to a grid (Figure 4.21 D). The lamella is then thinned and polished (Figure 4.21 E-H). Figure 4.21 illustrates the lift out process.

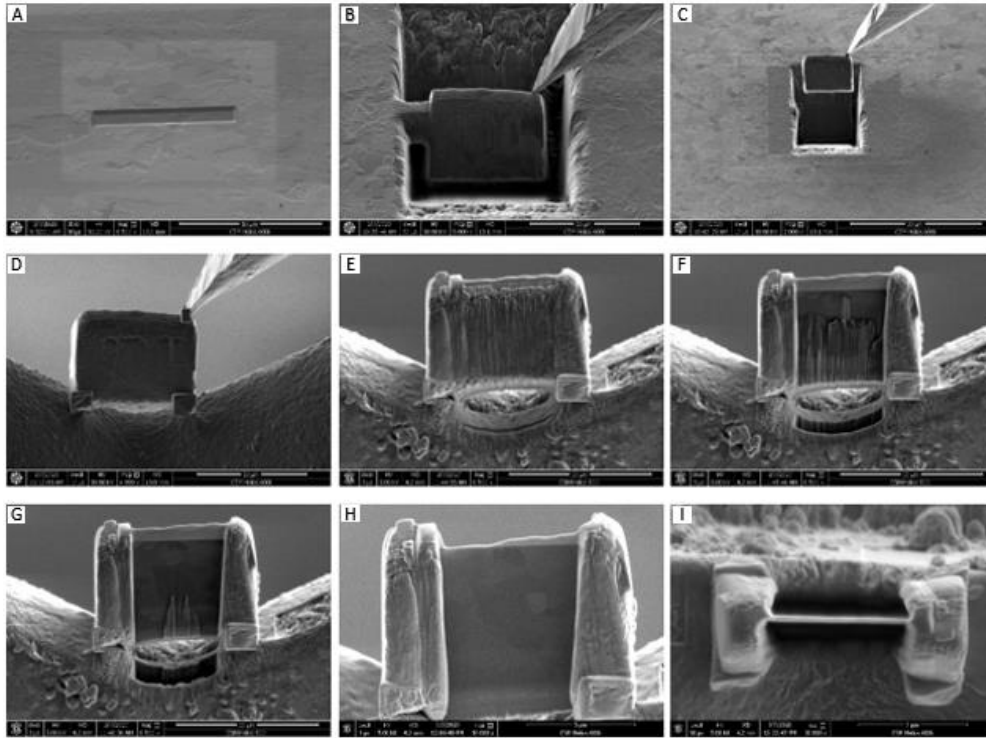


Figure 4.21 Liftout process. A – ROI with a platinum deposition. B – Probe in the corner of the ROI. C – Lift of the lamella. D – Welding of the lamella to the Cu grid. E – Beginning of the thinning process. F – Thinning process after a few minutes. G – Last steps of the thinning process. H – Polished lamella. I – Final thickness of the lamella.

4.10. Image analysis

Image analyses and processing were done using the FIJI software. The Enhance Contrast tool was used as a pre-processing and the trainable Waikato Environment for Knowledge Analysis (WEKA) segmentation plugin was used for the image segmentation process. The following paragraphs describe an example of image segmentation.

The first step of the process was the contrast enhancement. The original image has its contrast enhanced in order to make easier the differentiation between the regions. Figure 4.22 shows an original image and a contrast enhanced image.

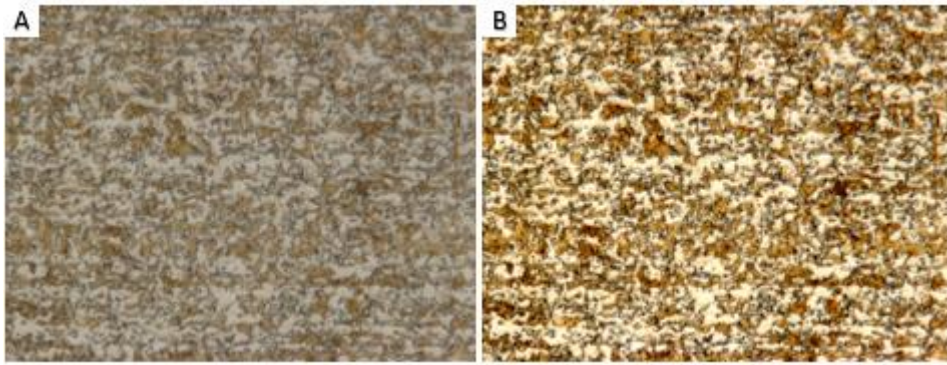


Figure 4.22 Example of the pre-processing. A) Original image; B) Image with enhanced contrast

After the pre-processing is done the WEKA plugin is run. Figure 4.23 shows the plugin window. In the plugin, regions are manually marked and labeled. For the sake of this example, the regions will be identified just by their color, as white, brown and black. The first few classifying runs are usually wrong, but as more and more samples are taken from the image the classifying process more refined and precise.

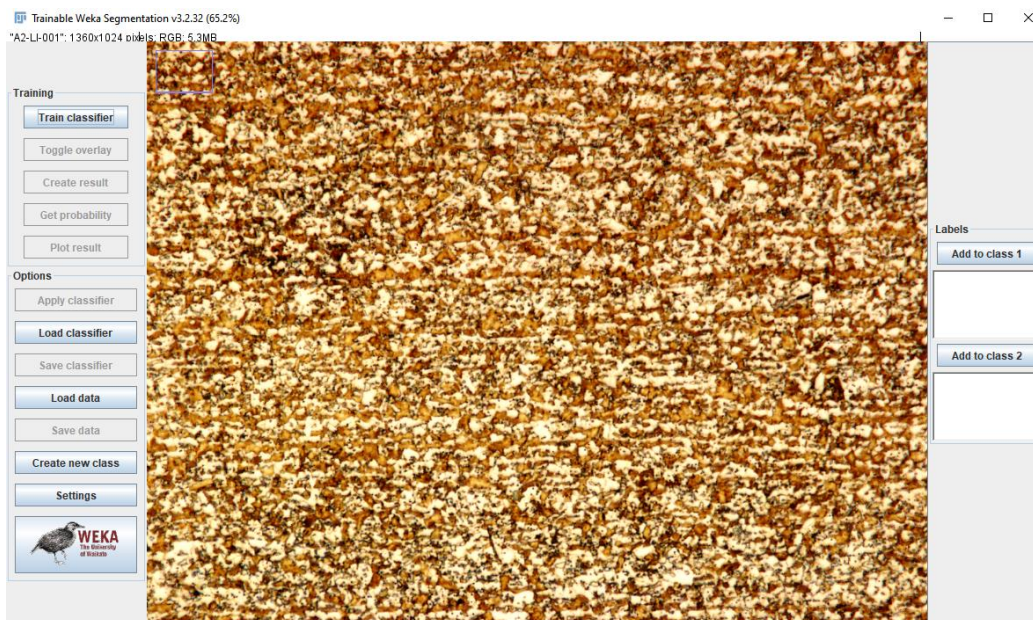


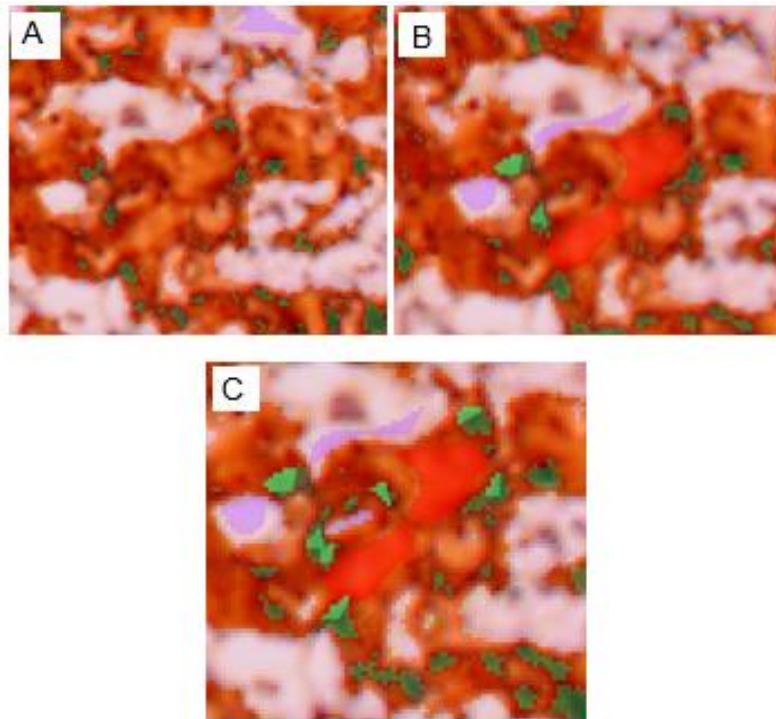
Figure 4.23 WEKA plugin window.

Figure 4.24 shows examples of marked regions. Figure 4.25 shows the improvement of the classifying process as new regions are marked and the training was done. Notice that in image A there is a black/white/brown region being classified as brown. In image B the same region has some

black and white being classified, although still not correctly. Image C has a much better result for the white and black segmentation, as shown by the black arrows.



Figure 4.24 Examples of marked regions.



4.25 Example of the improving segmentation process. A – Close look on a region with a single training process. B – Same region after 3 training were done. C – Region after 5 training were done.

If the image had not gone through the preprocessing step, the segmentation could prove to be complicated, as illustrated by Figure 4.26.

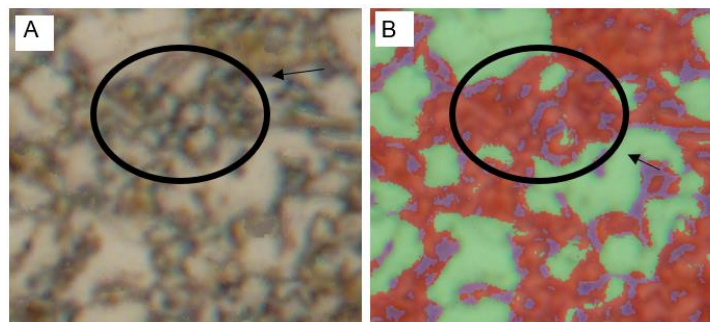


Figure 4.26 Example of miss segmentation in an image without preprocessing. A – Original image. B – Wrongly segmented image.

After the classifier is trained, providing a good classifying result, the image can be segmented, and the classifier can be saved to be used in the next image. The more images are used in the training of a classifier, the easier and more precise becomes the segmentation process.

The classification was done using a fast random forest setup, with 200 trees and constructed considering 2 random features. The classified image was then transformed to an 8 bit gray scaled image. The image is then duplicated, and the segmentation is done using the Threshold.

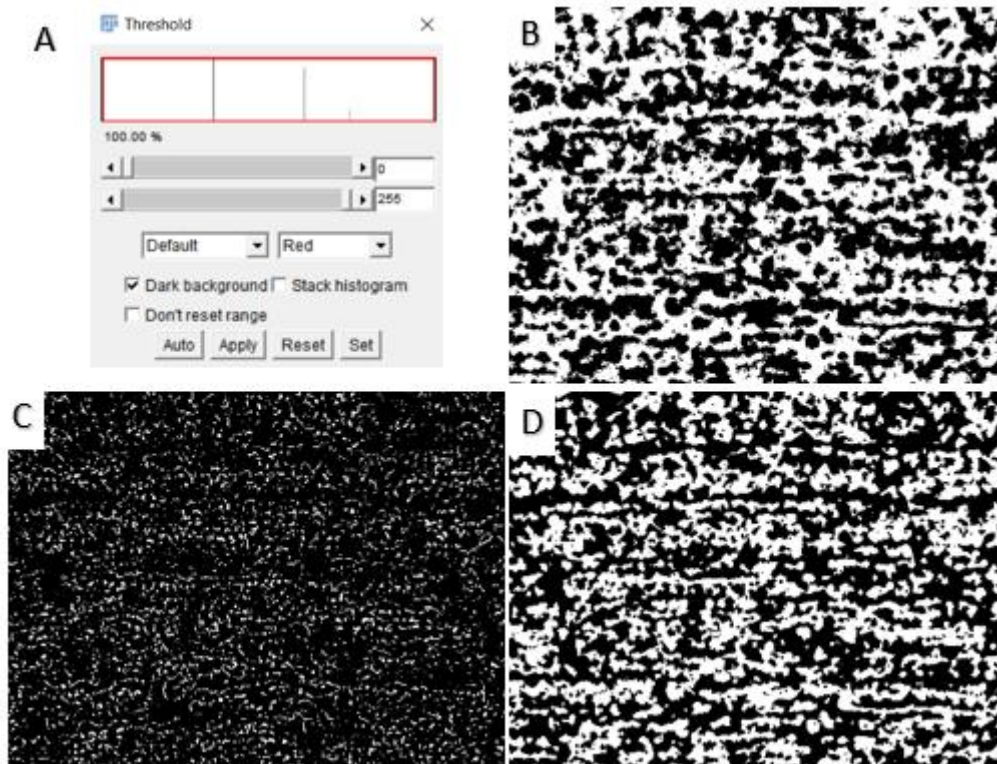


Figure 4.27 Threshold interface and segmented regions. A – Software interface. B – Brown region. C – White region. D – Black region.

The segmented regions can then be analyzed. The image analysis allows several measurements such as area, grain size, aspect ratio among others. This segmentation process was done both in the LOM, SEM, AFM and EBSD images.

4.10.1. Interface Segmentation

Considering that the ferrite-martensite interface is the main cause of void nucleation in DP and CP steels, the quantification of this interface was considered in this thesis. The segmentation of these interfaces was done using the FIJI software. In the interface analysis, the retained austenite was

disregarded. That was done because its content was small, as was its influence on the possible void nucleation.

First a segmented EBSD or AFM map, like the one from Figure 4.28, was separated in 3 segmented maps, for bainite, ferrite, and martensite. This separation was done using the commands “Color Threshold”, “8-bits” conversion and “Threshold”. An example of this command sequence can be seen in Figure 4.29 for a CP1200 steel.

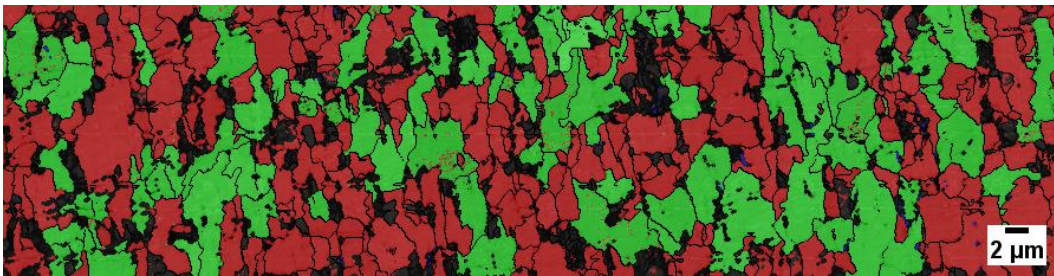


Figure 4.28 Segmented EBSD map of the CP1200 steel. Red ferrite (45.9%), green bainite (35.2%), black martensite (18.7%) and blue retained austenite (0.2%).

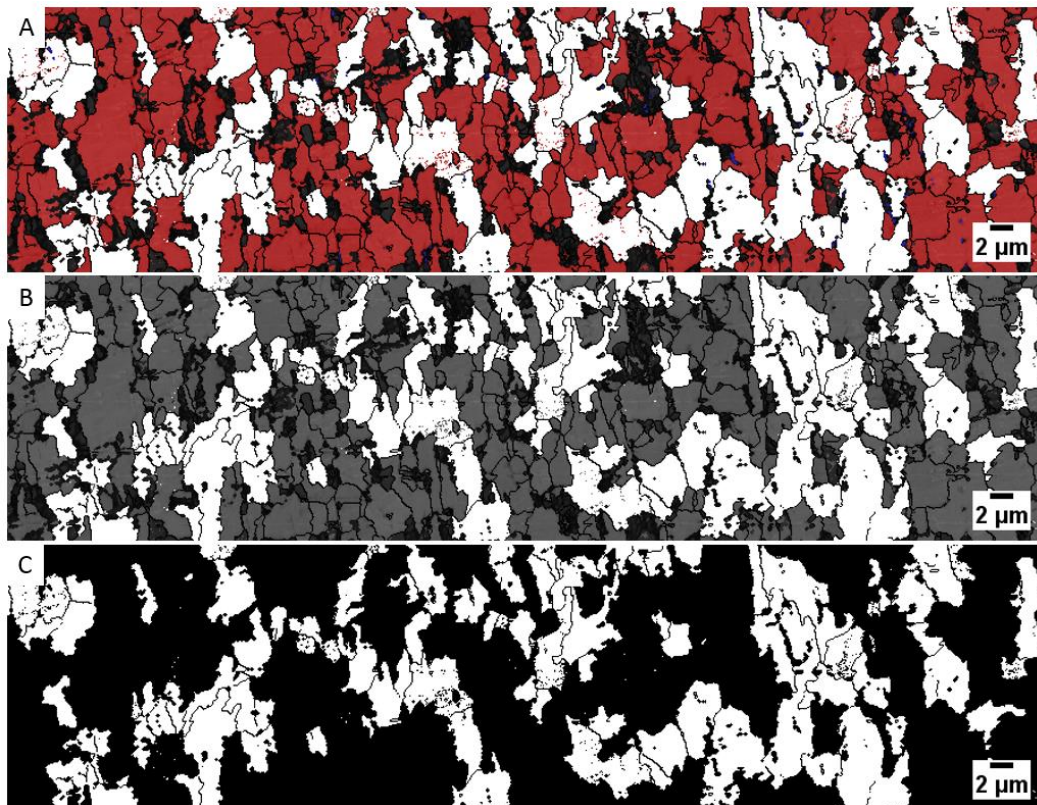


Figure 4.29 Example of the steps to separate the segmented microconstituents. A – Color threshold. B – 8 bits conversion. C – Threshold.

Once the microconstituents are separated, some small noise can be seen in the segmented figure; to deal with the noise, the morphological “open” command is used. This command is followed by the binary “outline” one. Figure 4.30 shows the example for this noise cleaning and interface segmentation. The yellow arrow in the Figure 4.30A points to one “noise” particle that was cleaned in Figure 4.30B. Even with that, some regions of internal interface can be seen in Figure 4.30C, due to either precipitates presence or to mis-indexation.

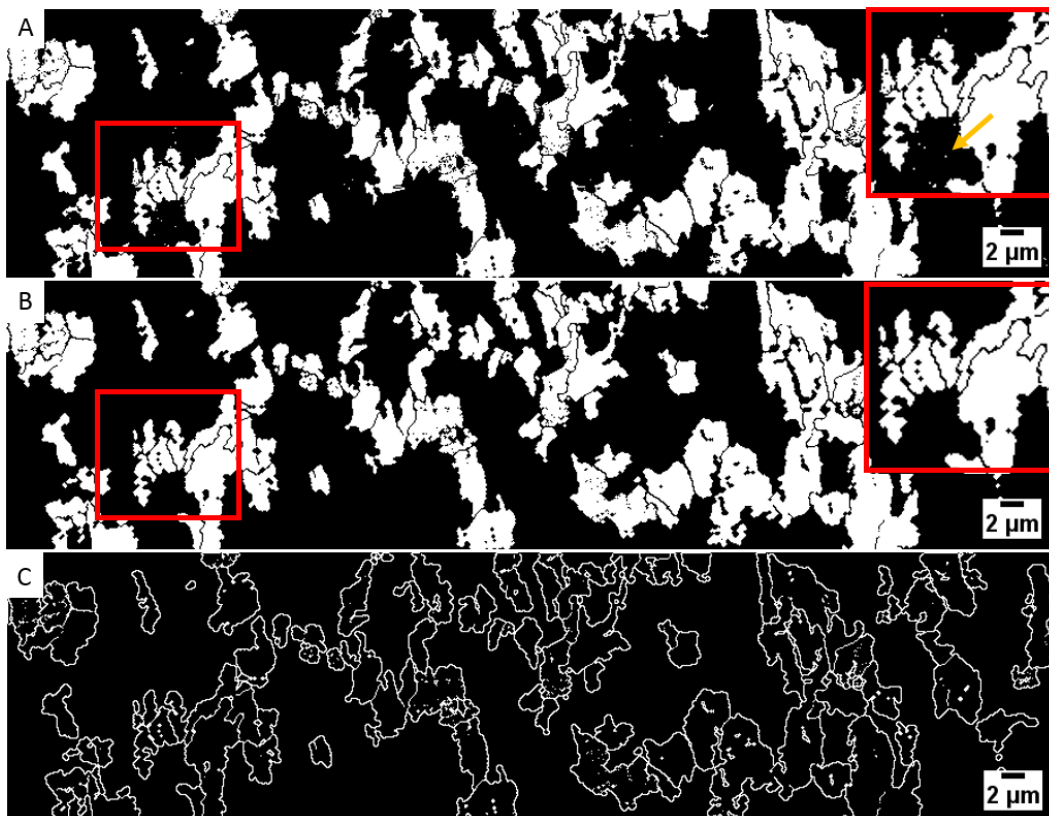


Figure 4.30 Example of the noise cleaning and interface segmentation. A – Segmented bainite. B – Cleaned segmented bainite. C – Interface of the bainitic grains. The zoomed in area in A and B shows example of noise cleaned, as pointed by the yellow arrow.

Once this process was done for the three microconstituents, the commands “image to stack” and “stack to RGB” were used. By doing that, a colored image of all the interfaces can be obtained. The color in the image follows the RGB system. In this way, if we use ferrite as red, bainite as green and martensite as blue, we will have a yellow bainite-ferrite interface, cyan bainite-martensite interface and a magenta ferrite-martensite interface.

This color scheme can be seen in Figure 4.31 and an example of the interface on the CP1200 steel can be seen in Figure 4.32.

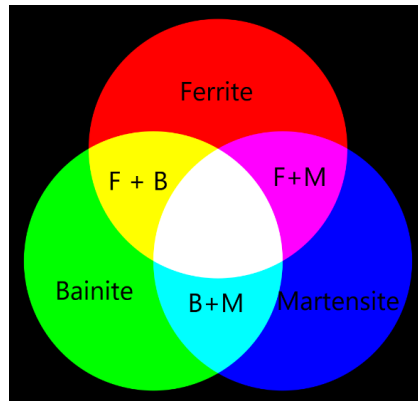


Figure 4.31 Color scheme used for the interfaces.

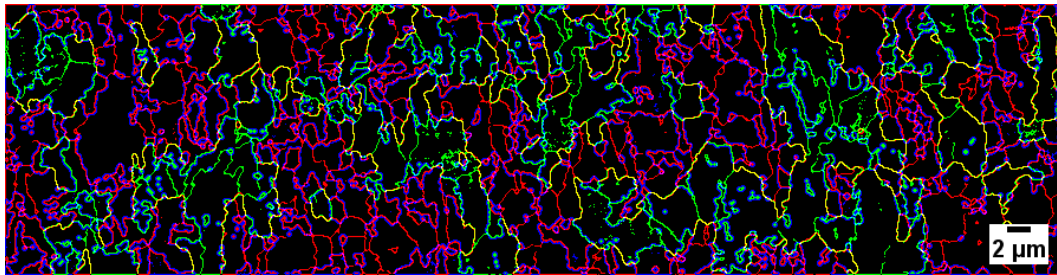


Figure 4.32 CP1200 Colored interfaces following the RGB color scheme. Red ferrite, green bainite, blue martensite and their derived colors.

4.10.2. Grain Size Measurements

The grain size was measured both in FIJI and in AZtecCrystal. In the latter, the mean grain size can be directly seen in the grain size tool, as long as the correct threshold angle for boundary was allocated, as the previous example from Figure 4.15. Also, if a particular microconstituent, after the segmentation, is added as a subset, the grain size of that subset can be calculated as well. Figure 4.33 shows an example of subset grain size of ferrite and bainite in the CP1100. Some misindexed points can be counted as a whole grain, but that problem can be avoided by taking the list of grains (Figure 4.34) created by the software and exporting it to Excel. There, a minimum grain size can be decided so that the average can be more representative. At the same time, any grain whose result looks odd can be

highlighted in the list and be revealed in the EBSD map, as shown by Figure 4.35.

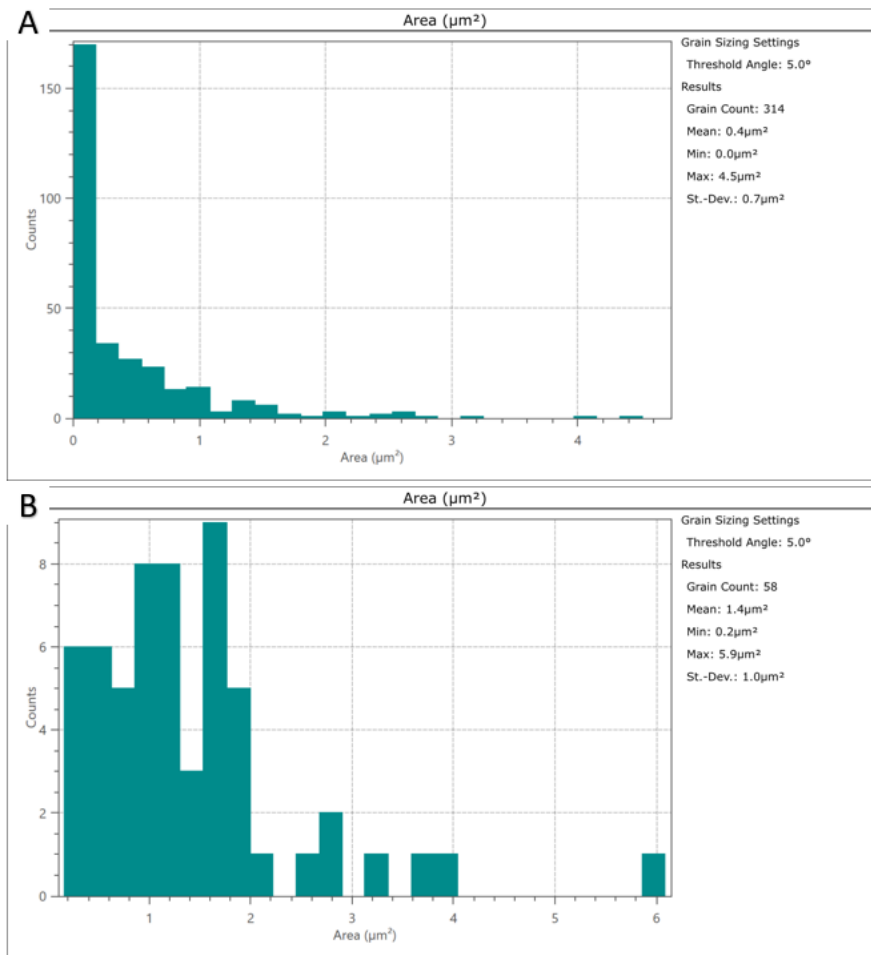


Figure 4.33 Distribution of grain size on the CP1100 steel obtained using the AZtecCrystal software. A – Ferrite grains. B – Bainite grains.

To filter the grain list, right-click on the column headers!

Clear All Filters Parameters...

ID	Phase	Area (pix)	Area (μm^2)	Perimeter (μm)	Equivalent Circle Diameter (μm)	Max Feret Diameter (μm)
5604	Iron bcc (old)	10	0	0,32	0,07	0,1
4998	Iron bcc (old)	11	0	0,29	0,07	0,11
394	Iron bcc (old)	10	0	0,23	0,07	0,11
6052	Iron bcc (old)	10	0	0,23	0,07	0,11
3193	Iron fcc	10	0	0,26	0,07	0,11
2819	Iron bcc (old)	11	0	0,25	0,07	0,11
2293	Iron bcc (old)	12	0	0,26	0,08	0,11
6590	Iron bcc (old)	15	0,01	0,29	0,09	0,11
88	Iron bcc (old)	10	0	0,24	0,07	0,11
1928	Iron fcc	14	0,01	0,3	0,08	0,11
1094	Iron bcc (old)	10	0	0,29	0,07	0,11
8083	Iron fcc	10	0	0,26	0,07	0,11
3956	Iron bcc (old)	10	0	0,26	0,07	0,11
3680	Iron fcc	11	0	0,3	0,07	0,11
3689	Iron fcc	10	0	0,32	0,07	0,12
3972	Iron bcc (old)	10	0	0,25	0,07	0,12
3950	Iron fcc	10	0	0,23	0,07	0,12

Grain Count: 829 Grain Size Number (ASTM E2627): 18,2

Figure 4.34 Image of grain size table on AZtecCrystal.

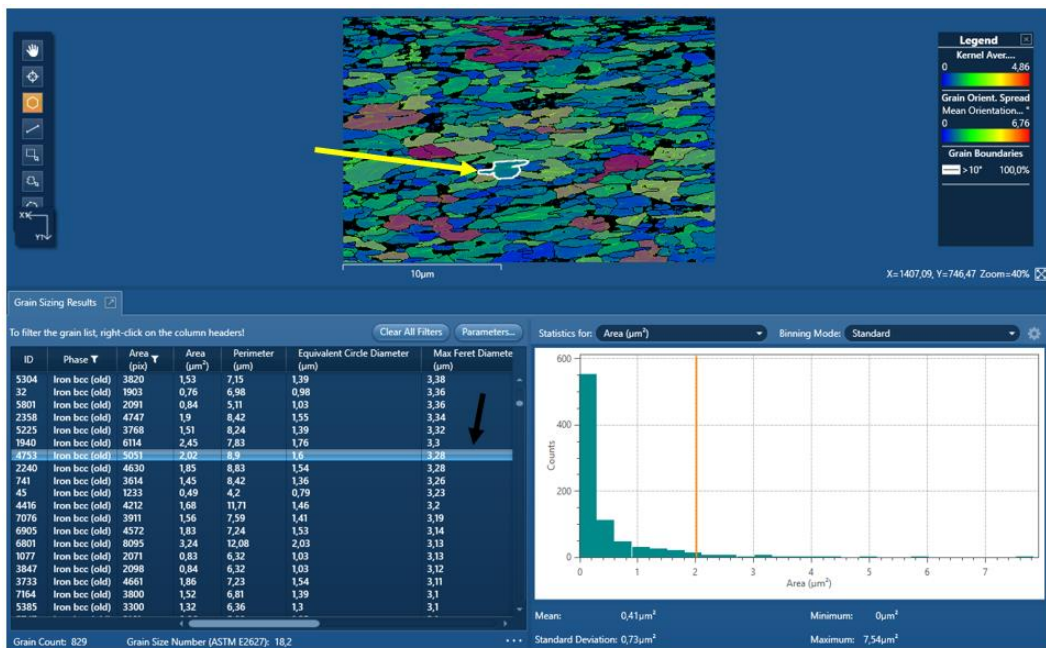


Figure 4.35 Interface of the AZtecCrystal during the grain size analysis. Black arrow points to a highlighted grain in the list and the yellow arrow points to that grain been revealed on the map.

As for the FIJI quantification of grain size, it was done using the “analyze particle” command. To use this command the image needs to be binary, therefore, this process was done in the already segmented maps. The small particles can be easily disregarded in the FIJI analysis by establishing a minimum grain particle size, such as $0.2 \mu\text{m}^2$, as seen in the tools interface in Figure 4.36. A second problem needs to be taken into account, that is, many boundaries are not well defined, from the computer’s perspective. During the image analysis, if a single pixel of the boundary is missing, the

two grains will be counted as one entity. This problem can be seen in Figure 4.37A and Figure 4.37B. An alternative to circumvent this problem is to use some morphological process such as “erode” or “open”. They will reduce a little the grain size, but they allow a better average measurement, as can be seen in Figure 4.37C and Figure 4.37D.

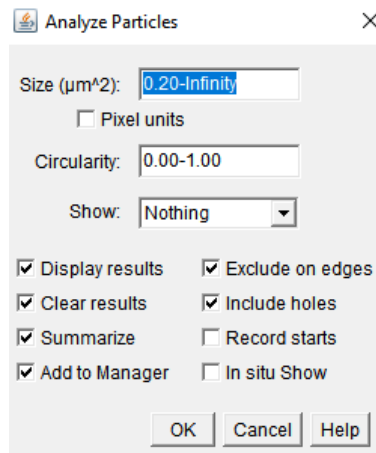


Figure 4.36 Interface of the analyze particles tool from FIJI.

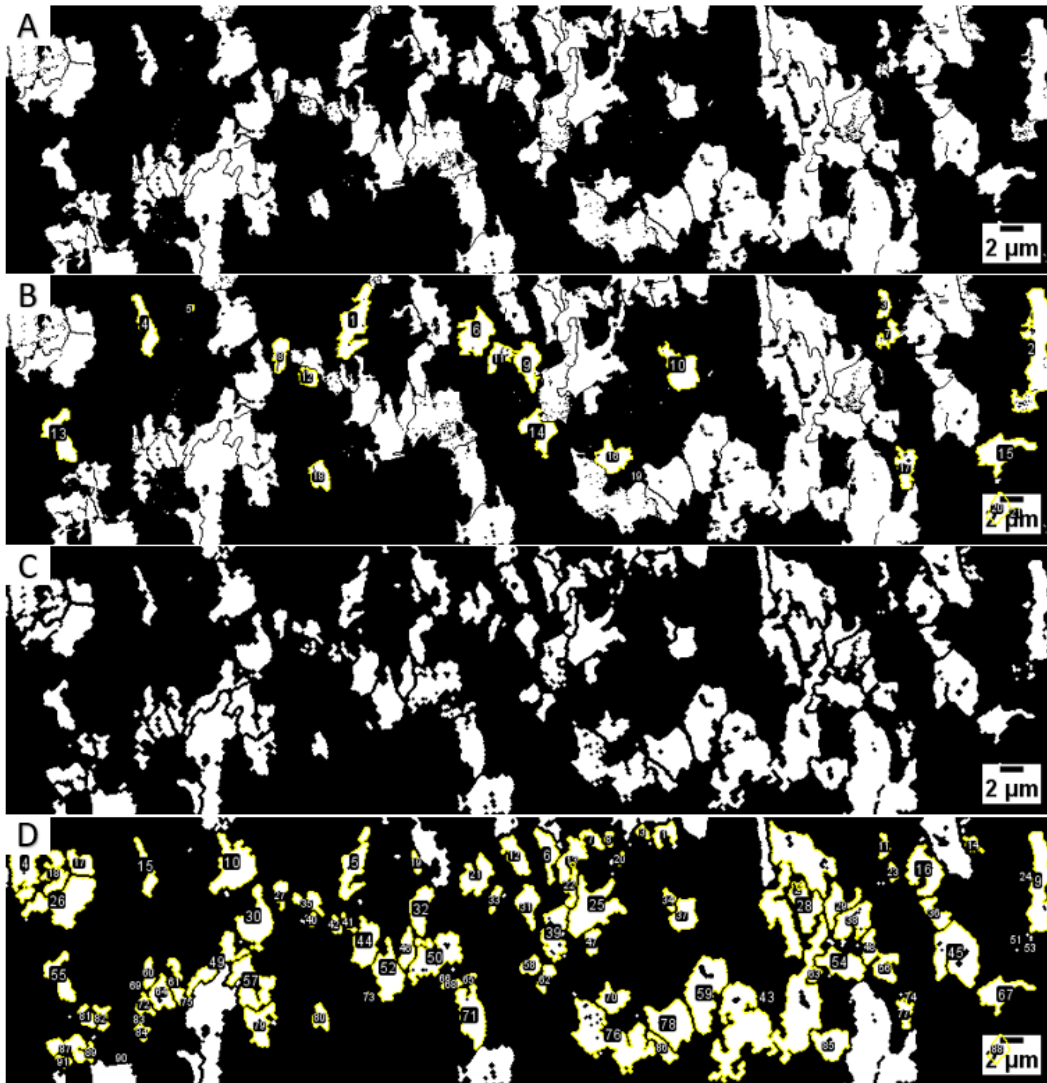


Figure 4.37 Example of grain size measurement on the bainitic microconstituent of the CP1200 done using FIJI software. A – Original segmented bainite. B – Mask of the analyze particles. C – Bainite grain after morphological operation. D – New mask of the analyze particles.

5 Results

5.1. Cold Rolled Steel

The cold rolled steel was the base steel used for the treatments. Thus, its microstructure was investigated, so that the effects of subsequent treatments effects could be better understood and eventually controlled.

5.1.1. Microstructure

A simple nital etching was used at the cold-rolled steel microstructure. Figure 5.1 shows a series of SEM micrographs with increasing magnification, displaying typical, banded, cold rolled microstructure. According to Tasan and associates, these bands were once referred to as ghosts [34], because even after treatments erase the banded aspect, they may, during deformation or heating, reappear [34], [121]. These bands present some detrimental effects to the mechanical properties, such as the fracture toughness, yield and tensile strengths [34]. The precise influence on the property is hard to determine, as that would demand a series of tests using unbanded steel with the same composition, grain size, phase fraction and inclusion morphology. A combination that is not possible on the homogenized unbanded steel [34].

The secondary electron image makes clear that the microstructure is a mixture of ferrite and pearlite. The segmentation needs to be done in a way that guarantees the quantification of the full pearlite region instead of only the cementite part. Figure 5.2 shows the difference between proper and improper segmentation. The WEKA software was used to segment the microconstituents, as seen in Figure 5.3. Table 5.1 shows the microconstituents quantification. EBSD analysis was also used on the cold rolled steel (**Erro! Fonte de referência não encontrada.**). Due to the high deformation of the samples, the {101} ferrite orientation is the typical one for

cold rolled steels [110]. EBSD presents a lot of zero solutions, but the identified regions show a high orientation. Figure 5.4 presents a cleaned map with its pole figure and the series ODF analysis done keeping the second Euler angle (ϕ) constant, in intervals of 5° .

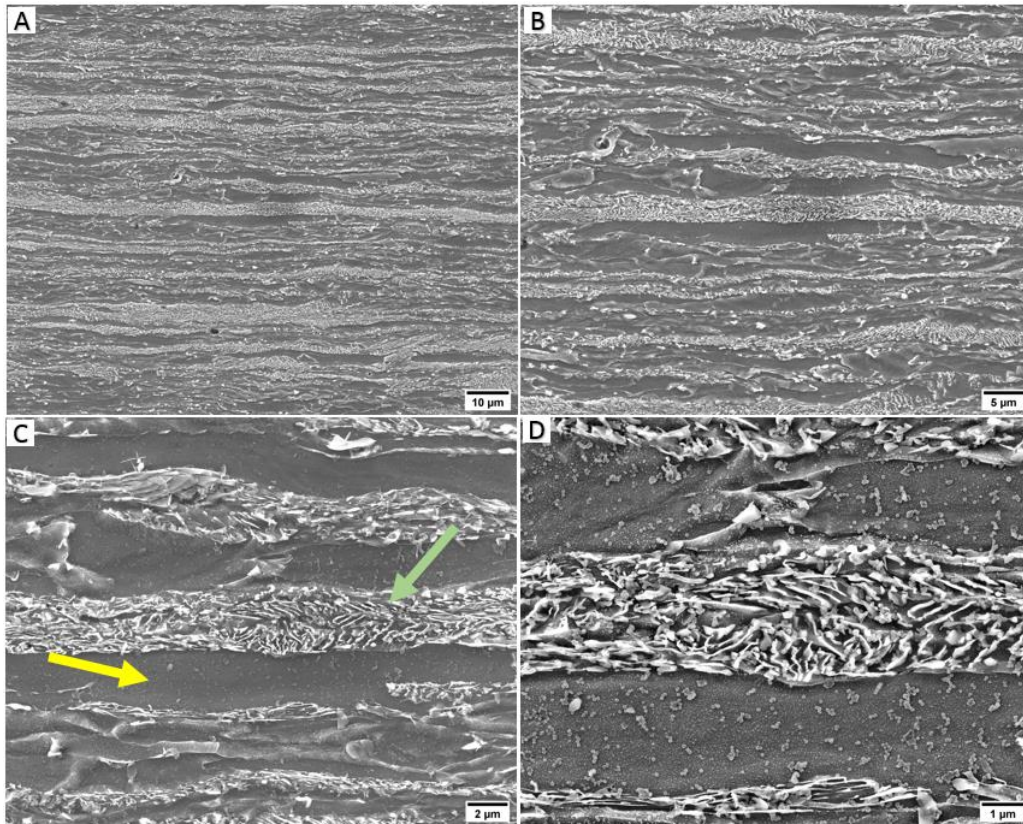


Figure 5.1 SEM secondary electron image of the cold rolled steel. A – 1000X magnification. B – 2000X magnification. C – 5000X magnification. D - 10000X magnification. Yellow arrow shows the ferrite, green arrow shows the perlite.

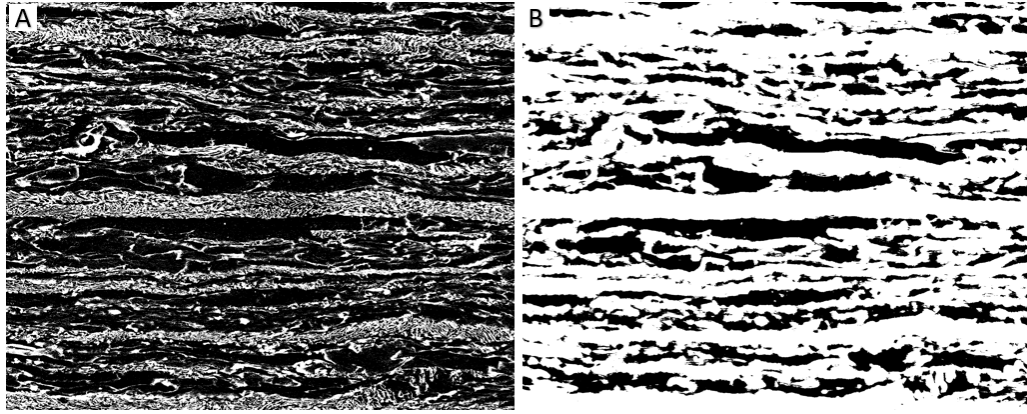


Figure 5.2 Examples of segmentation from the 2000X magnification microscopy. A – Improper way where cementite was segmented instead of pearlite. B – Correct segmentation of the pearlitic region.



Figure 5.3 WEKA segmentation of the cold rolled steel. A – Original 2000X image. B – Pearlite. C – Ferrite.

Table 5.1 Microstructural quantification of cold rolled steel

Ferrite (%)	Pearlite (%)
72.6 ± 1.5	27.8 ± 1.5

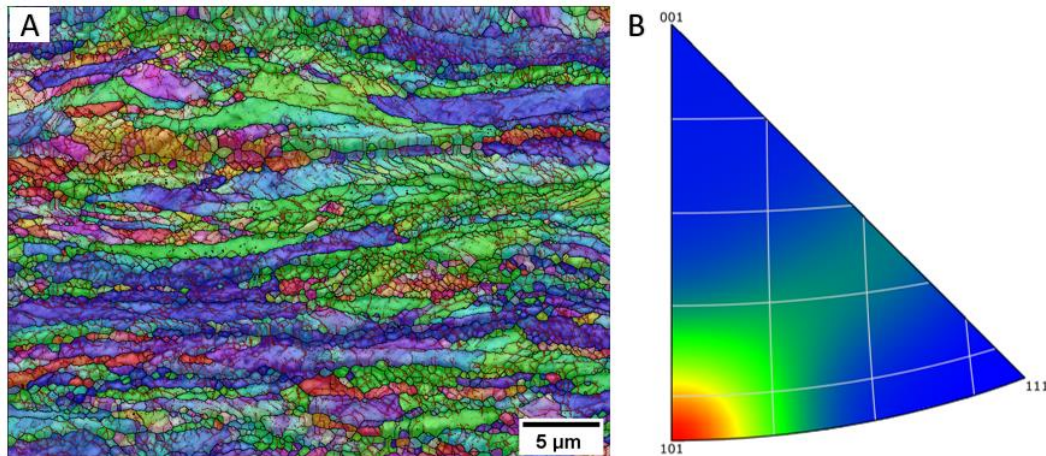


Figure 5.4 Cleaned EBSD analysis of the cold rolled steel. A – Band Contrast plus Inverse Pole Figure. B – Inverse Pole figure with high 101 orientation.

5.2. Calculations

One of the first steps to design the treatment of a complex-phase steel is to calculate the bainite start temperature for that composition. Seven empirical models were used for this calculation, Table 5.2 presents the calculation results, as well as the average. The bainite start temperature measured latter by dilatometry was very close to the average of the calculated from the empirical models.

Table 5.2 Bainite start temperature calculation.

Model	Temperature (°C)
Bodnar #2	577
Kirkaldy	538
Kunitake	573
Lee #2	573
Li	541
Miettinen	584
Suehiro	557
Average	563

5.3. Dilatometry

5.3.1. CCT curve

Continuous cooling transformation curves were used to determine the transformation temperatures for each constituent, (Figure 5.5), providing better understanding of the steel and allowing the design of the heat treatments.

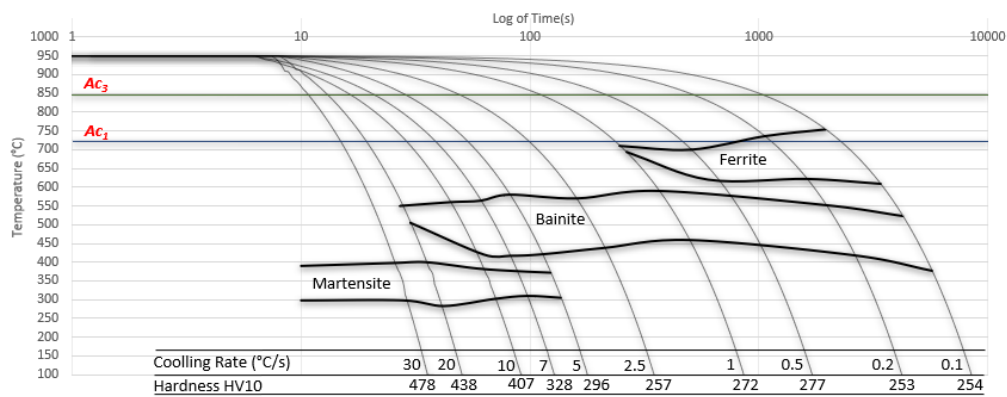


Figure 5.5 Continuous cooling transformation curve obtained from dilatometry experimentation. Cooling rate measured in °C/s, rate going from 30 to 0.1 from left to right.

The CCT data shows that due to the shift of the ferrite field to the right, there is a reasonable time window for producing bainite by quenching avoiding the ferrite transformation, one ideal case for the complex-phase transformation process, as described on section 3.2.2.

Samples with a cooling rate of 30°C/s showed pure martensitic transformations. As the cooling rate decreased to 20 °C/s there was a small bainitic transformation prior to the martensitic one. Due to this bainitic transformation, the remaining austenite is richer in carbon, which makes it more stable, consequently, the M_s temperature decreases as the amount of bainite formed increases. This can be seen in the 20, 10, 7 and 5 °C/s cooling rates. In the 0.1 °C/s, the cooling is so slow that the B_f temperature is even lower than the original M_s one.

The CCT curve was obtained by heating samples to 950 °C, keeping at that temperature for 5 minutes, followed by a continuous cooling to room temperature at different rates. Figure 5.6 shows the curves for rates ranging

from 50 °C/s to 5 °C/s. Figure 5.6 A and B reveal pure martensitic transformations. Figure 5.6 C shows a small deviation from linearity that indicates a small amount of bainite transformation. Figure 5.6 D, E and F show an increasing amount of bainite transformation with a decrease in the martensitic one. Figure 5.7 A shows an almost fully bainitic transformation curve, Figure 5.7 B through E show an increasingly amount of ferrite transformation, as the amount of bainite transformation decreases.

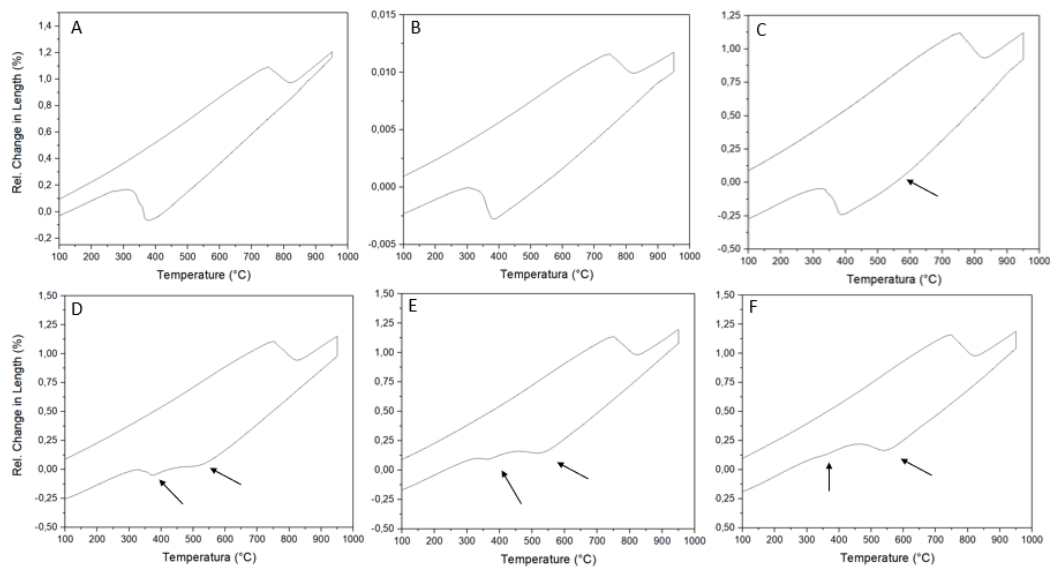


Figure 5.6 Relative change in length versus temperature curves. A – 50 °C/s. B – 30 °C/s. C – 20 °C/s, black arrow shows a small bainite transformation. D – 10 °C/s, black arrows point to martensite and bainite transformation. E – 7.5 °C/s, black arrows point to martensite and bainite transformation. F – 5 °C/s, black arrows point to martensite and bainite transformation.

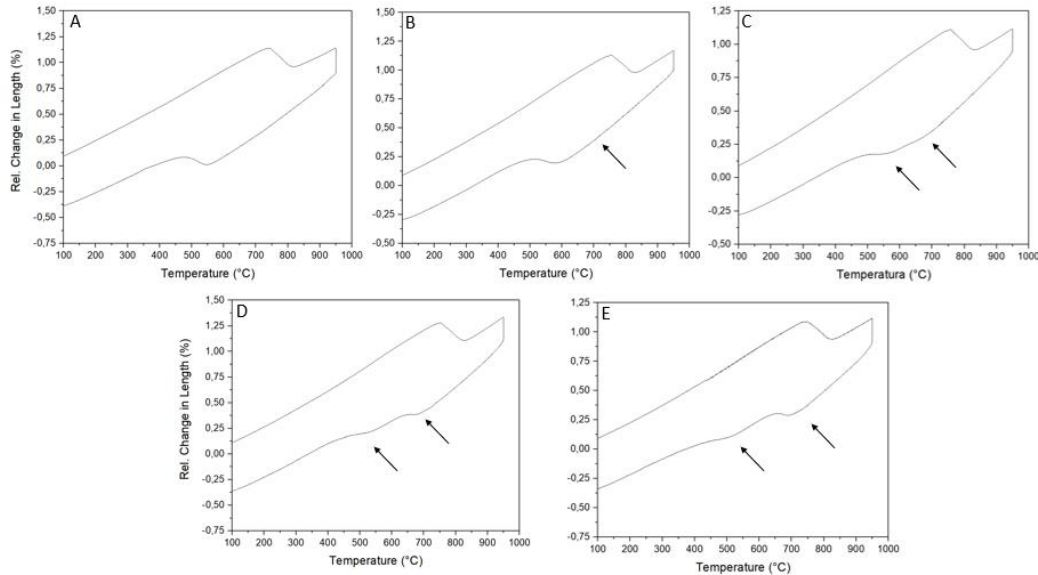


Figure 5.7 Relative change in length versus temperature curves. A – 2.5 °C/s Close to fully bainitic transformation. B – 1 °C/s, black arrow shows a very small deviation that indicates a ferrite transformation. C – 0.5 °C/s. D – 0.2 °C/s. E – 0.1 °C/s.

5.3.2. Heat Treatments

Using the CCT curve, several treatments were designed. Those treatments were divided into a series of soaking followed by quenching and hold treatments, as listed in Table 5.3. With the results of these simpler treatments, some more complex ones, that included the galvanizing step of the industrial production process were done. In this section the results for those treatments will be presented and discussed.

Table 5.3 List of thermal treatments

Sample ID	Soaking (°C)	Isothermal Holding (°C)
CP840A500	840	500
CP840A480	840	480
CP840A450	840	450
CP840A420	840	420
CP830A500	830	500
CP820A500	820	500
CP820A480	820	480
CP820A450	820	450
CP820A420	820	420
CP810A500	810	500
CP800A500	800	500

Figure 5.8 shows the dilatometric curves for samples CP840. In all treatments it is possible to see a change in the linearity as soon as the cooling begins, even though that occurs in a temperature where transformation should not be happening yet. Therefore, those deviations were considered an artifact of the dilatometry measurements. Due to these artifacts and considering that pre-existing ferrite may be growing, it is difficult to point out when the nucleation of new ferrite grains begins. All the CP840 samples show a bainitic transformation at about 600 °C that proceeds until the isothermal hold. They also present a small martensitic transformation. A similar behavior is seen in Figure 5.9 for the CP820 series of treatments.

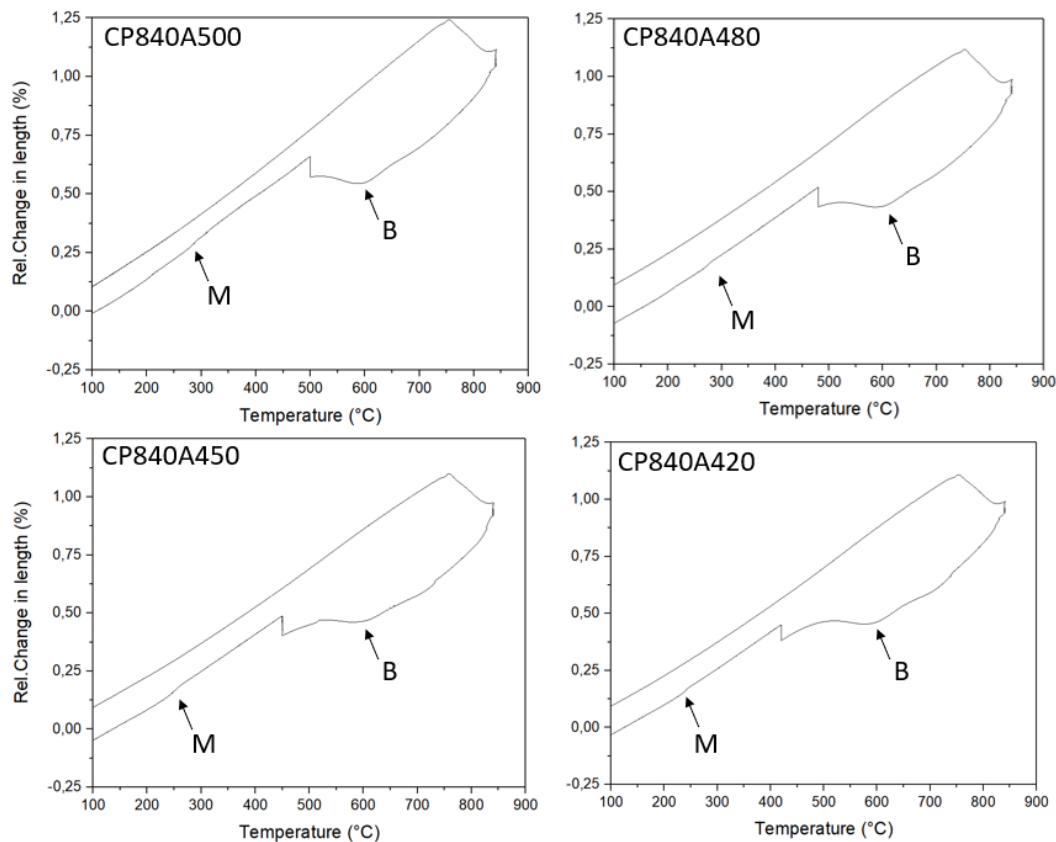


Figure 5.8 Dilatometric data for the CP840Axxx treatments.

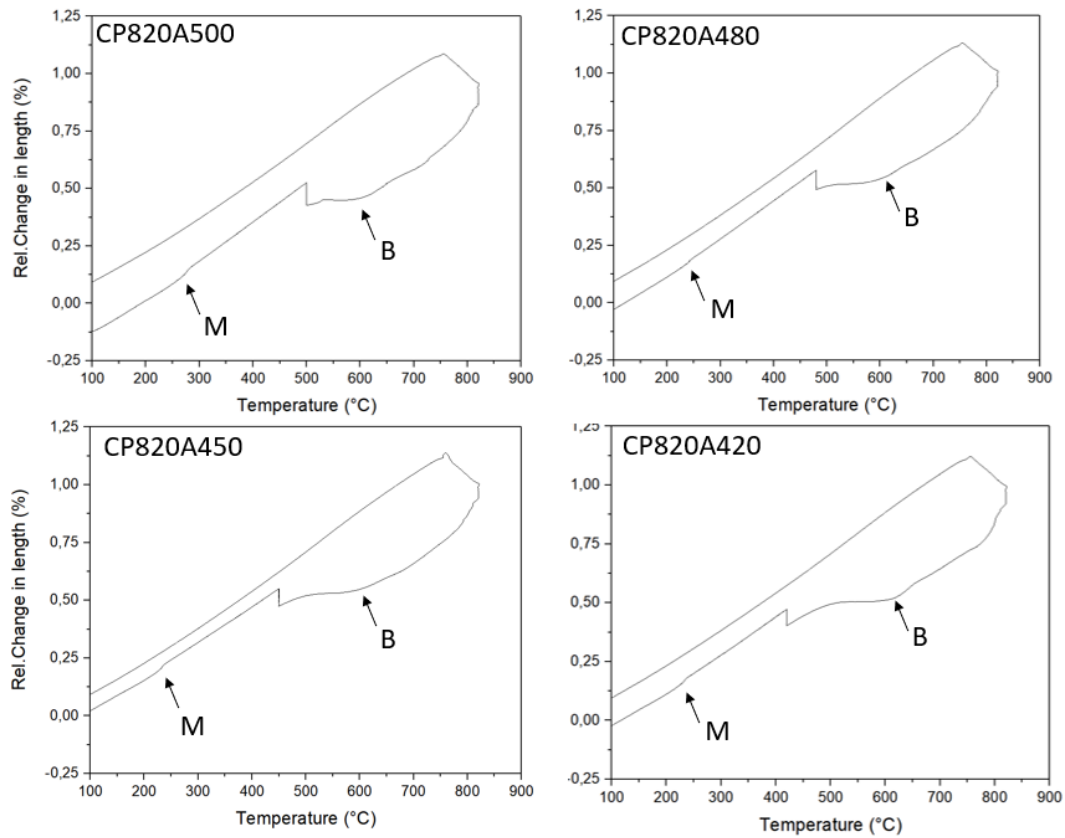


Figure 5.9 Dilatometric data for the CP820Axxx treatments

Using the hardness results, which will be presented in section 5.4.2, it was determined that holding at 500 °C was the best option. Figure 5.10 shows the dilatometric data for the treatments done using 500 °C as the holding temperature.

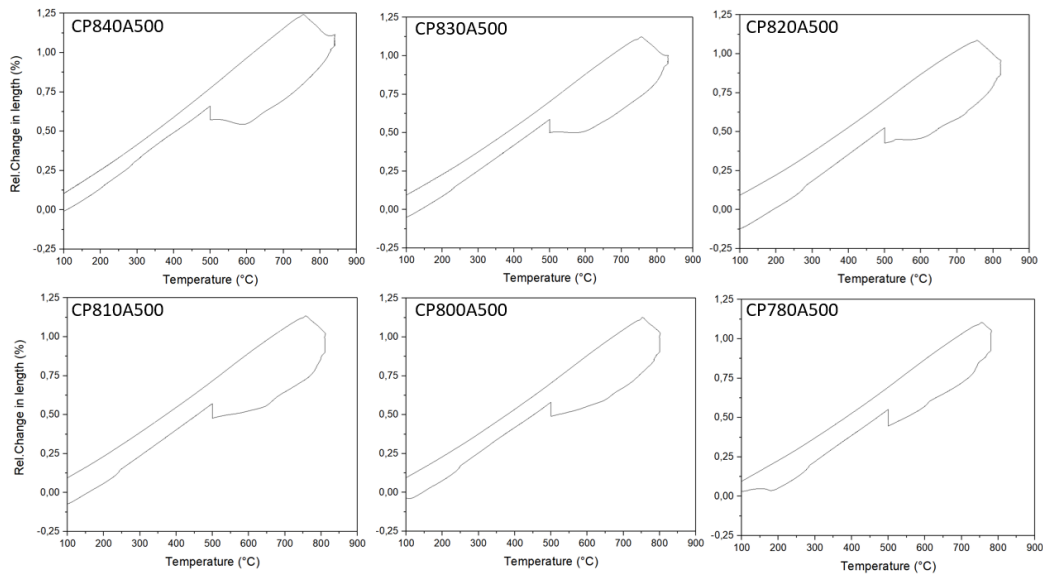


Figure 5.10 Dilatometric data for treatments CPXXXA500.

Besides these simpler soaking and holding treatments, six more complex treatments were designed in agreement with CSN. Among these six treatments, two replicate the thermal cycles for production of CP1100 (treatment 4) and the CP1200 (treatment 6). The heat treatments curves used for the treatments 1 through 6 can be seen in Figure 5.11 and their relative change in length versus temperature is shown in Figure 5.12.

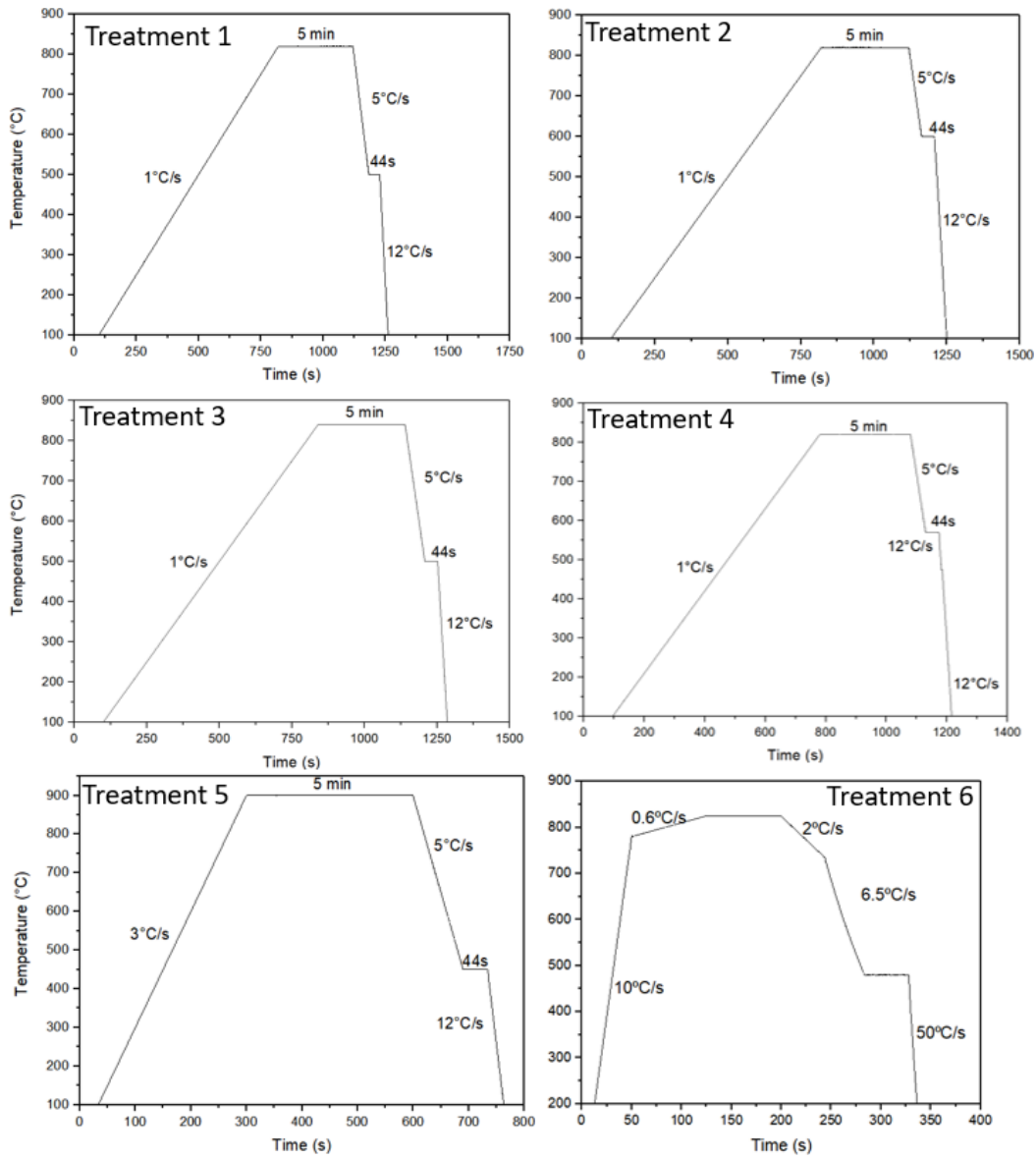


Figure 5.11 Complex-Phase experimental heat treatments.

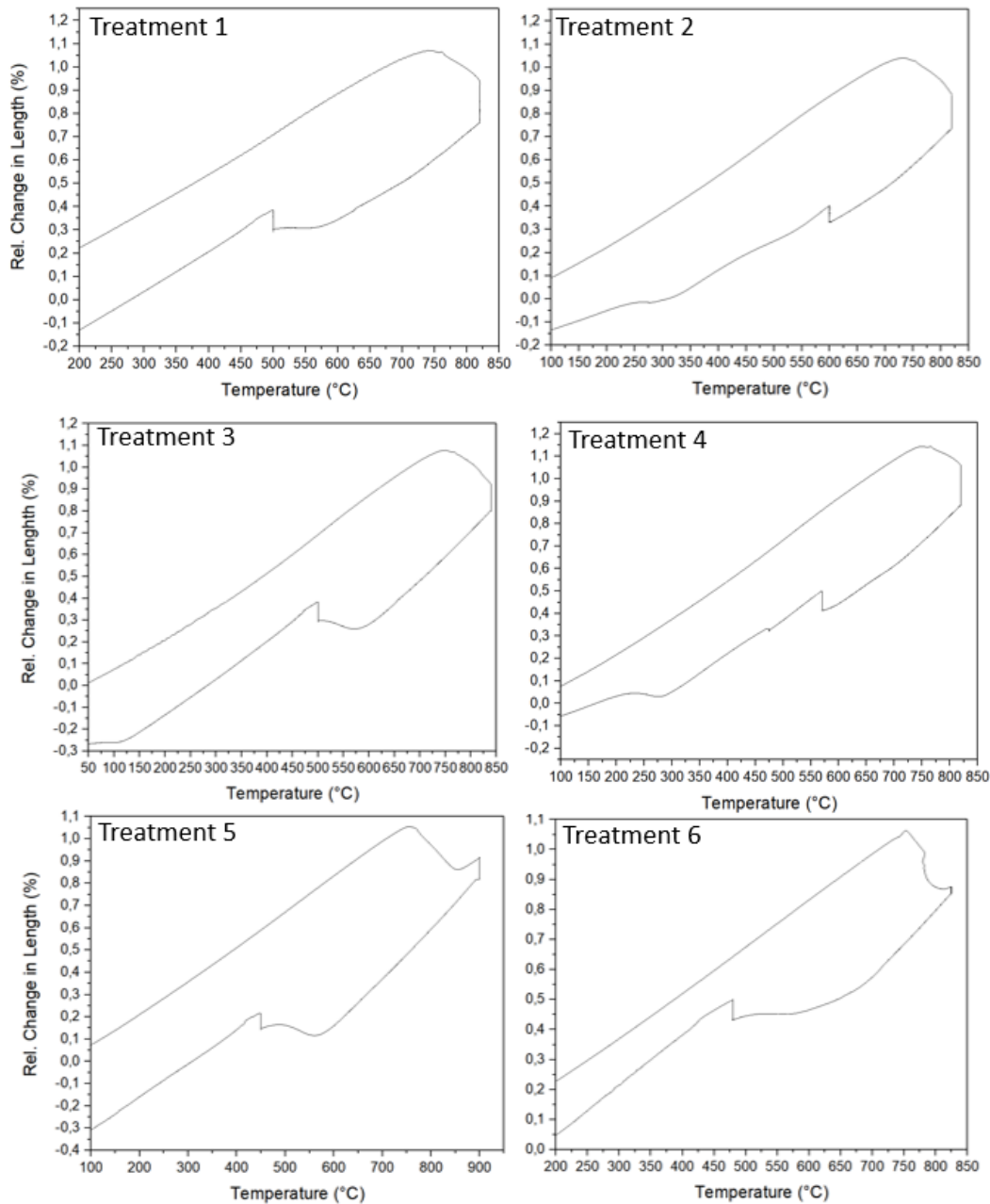


Figure 5.12 Relative change in length as a function of temperature for treatments 1-6.

5.3.3. CP1100

The thermal cycle used to produce the CP1100 in the industrial process was reproduced (Figure 5.13) in the dilatometer. The results can be seen in Figure 5.14.

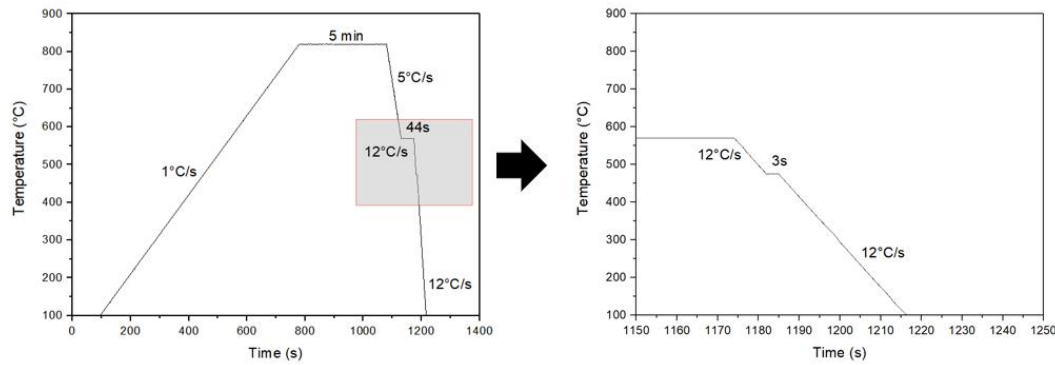


Figure 5.13 Treatment used to reproduce the CP1100 thermal cycle in the dilatometer.

After the 800 °C hold there is a sharp start in the cooling (Figure 5.10), absence of a transformation at the start of the cooling further indicates what was seen in Figure 5.8 was an artifact, instead of a ferrite transformation. As there is intercritical ferrite, it is possible that instead of forming new ferrite grains, pre-existing ferrite grains may be growing. The expansion associated with this growth can be concealed by the steel contraction due to the cooling. The result would then be a very small deviation of the linearity, as seen in the curve. Under 600 °C a continuous cooling bainitic transformation begins and continues through the 570 °C hold. During the galvanizing step there is a very small change in length that could also be due to bainite, suggesting that there is a small transformation after the isothermal hold. Near 300 °C the martensitic transformation takes place.

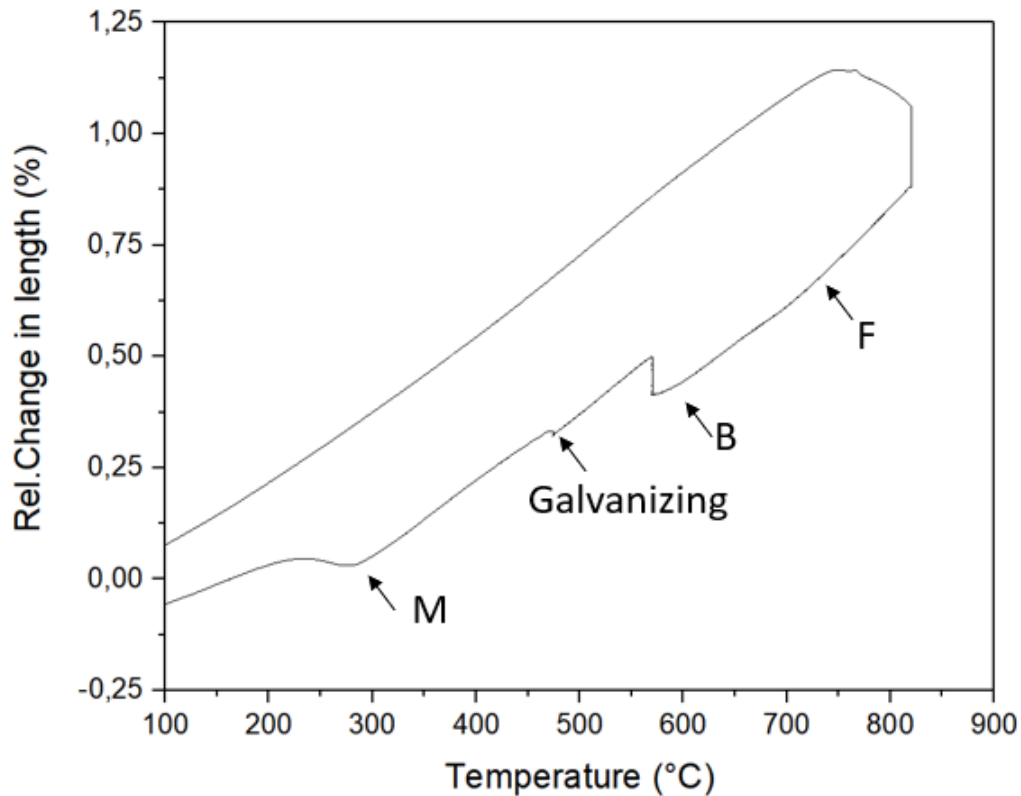


Figure 5.14 Dilatometric results for the CP1100 treatment. Black arrows point to the relevant deviations of the linearity.

5.3.4. CP1200

The CP1200 treatment was designed combining the information provided by the CCT curve with the empirical data available and the experience of CSN in steelmaking. The heating curve and its dilatation cycle can be seen in Figure 5.15. The heating starts fast at 10 °C/s and is slowed near the soaking temperature to guarantee a homogeneous temperature in the sample. After the soaking there is a slow cooling that simulates a passage step in the industrial scale. Following that, a fast cooling to the holding temperature is applied. The isothermal hold is followed by a quenching to the room temperature. A closer look at the cooling curve (Figure 5.16A) indicates that there is no transformation during the slow cooling start, suggesting that the artifacts seen in Figure 5.10, doesn't happen here. A very small ferritic transformation can be observed around 685 °C in Figure 5.16B, but the amount transformed is so small that the transformation can only be seen with the magnification of the curve. There

is a large bainitic transformation during the continuous cooling conditions seen in Figure 5.16C. After the hold there is some martensite transformation occurring in Figure 5.16D.

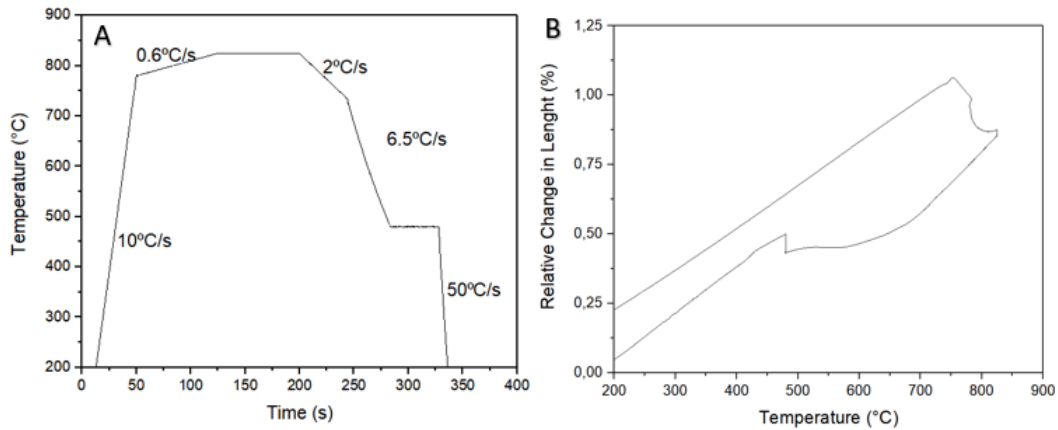


Figure 5.15 Dilatometry treatment of CP1200. A – temperature x time curve. B – Relative change in length x temperature curve.

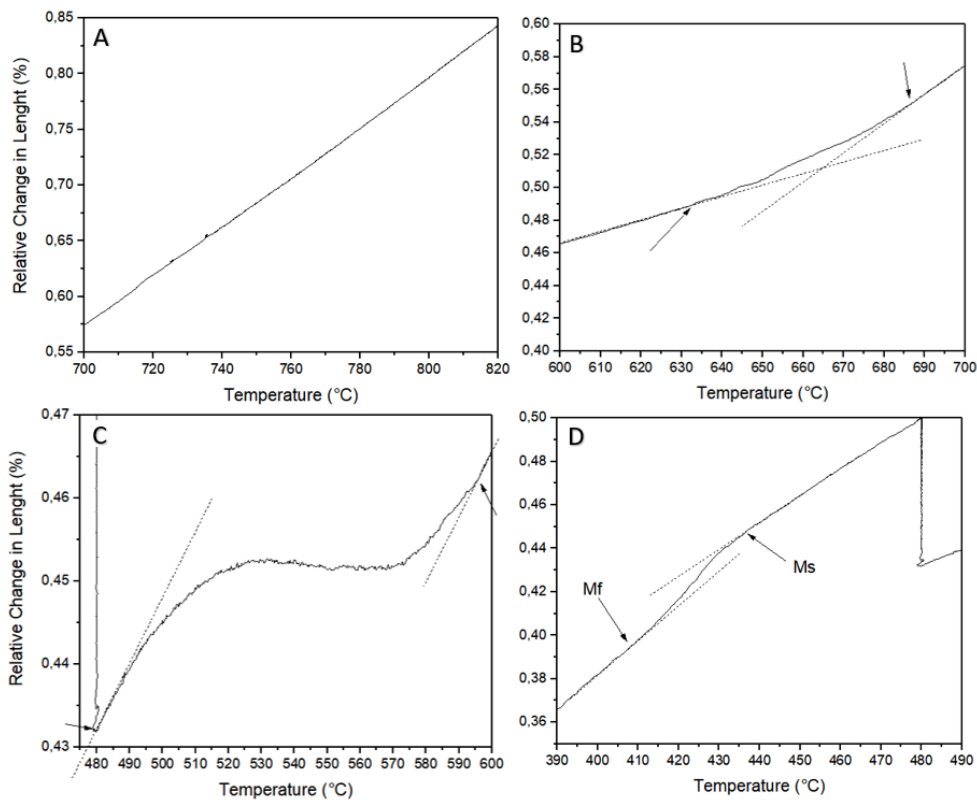


Figure 5.16 Closer look at the relative change in length x temperature curve for the CP1200 Steel.

A – Linear section with no transformation from 820 to 700 °C. B – Very small ferritic transformation (back arrows) between 680 and 630 °C. C – Continuous cooling transformation of bainite (black arrows) from about 590 until the isothermal hold. D – Martensite start and finish temperature (black arrows) after the isothermal hold.

5.4. Hardness

5.4.1. CCT Curve

Vickers Hardness HV10 measurements were performed on the CCT samples. The results can be seen in Figure 5.17. An indentation in the CP800A500 can be seen in Figure 5.18

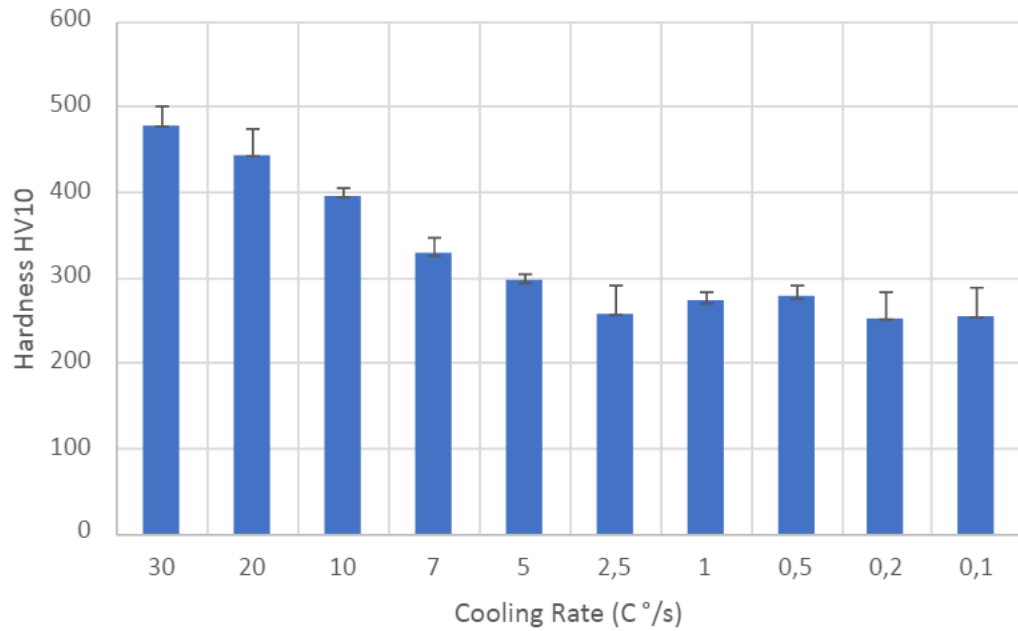


Figure 5.17 Hardness HV10 measurements done on the CCT samples.

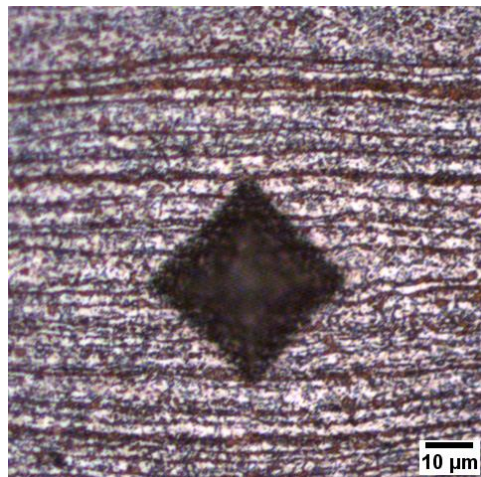


Figure 5.18 Harness HV10 indentation if the CP800A500.

5.4.2. Heat Treatments

Hardness Vickers HV10 measurement was done for the treated samples. The diagram in Figure 5.19 shows the average results. They indicate that the higher values of hardness were obtained for the holding temperature of 500 °C.

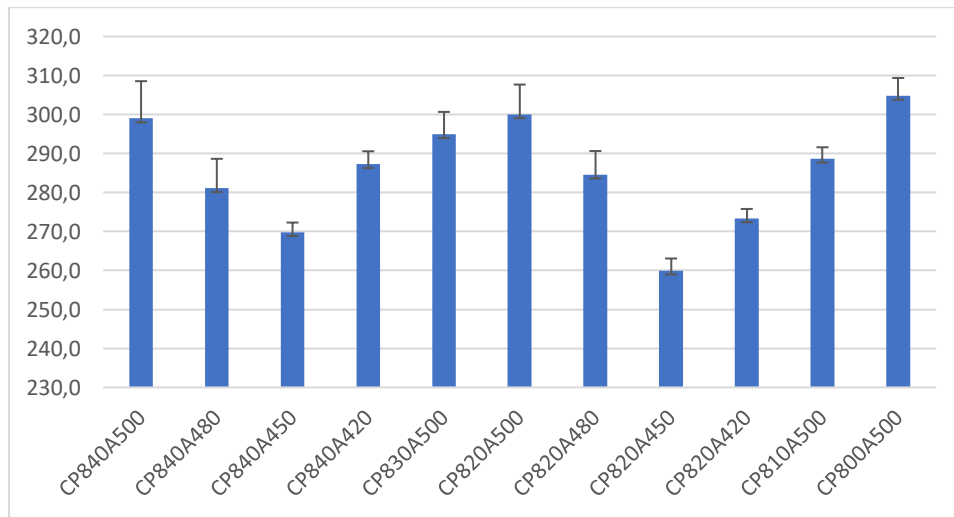


Figure 5.19 Hardness HV10 measures for the treatments.

In Figure 5.20 a diagram shows the average results for the more complex treatments.

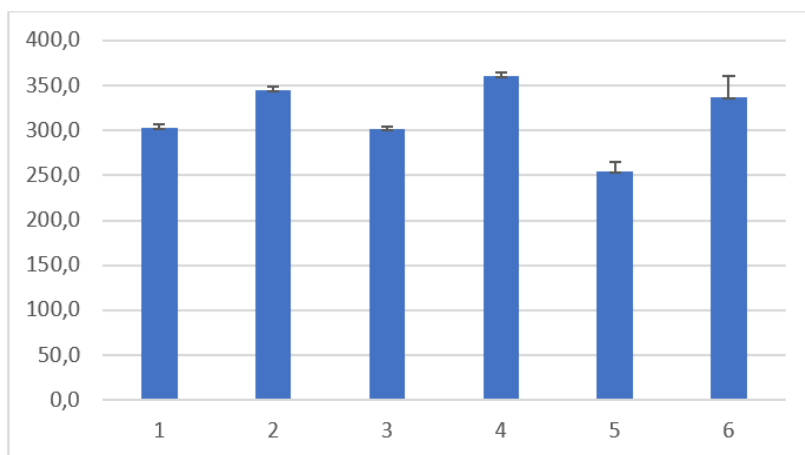


Figure 5.20 Average hardness HV10 measurements of the heat treated samples.

5.4.3. CP1100/CP1200

Table 5.4 shows the hardness measurements of the industrial CP1100 steel and the newly produced CP1200 steel. The higher hardness can be explained by its microstructure distribution that will be presented in section 5.6.

Table 5.4 Hardness measurements for the CP1100 and CP1200 steels.

Steel	HV10
CP1100 Industrial	323.8 ± 2.8
CP1200 Dilatometry	337 ± 2.3

5.5. CP1200 Mechanical Properties

An CP1200 steel was produced by CSN in both pilot and industrial scales. Its mechanical characterization using tension, bending and hole expansion tests was done at CSN research center [110]. The pilot scale samples were sub-sized 50mm samples and treated using five different soaking temperatures (Table 5.5). Then, the best results for a CP1200 were reproduced in an industrial scale. Samples for tension were then obtained from the initial, middle and final section of a processed plate. The tension results for the industrial scale are shown in Table 5.6.

Table 5.5 Pilot scale tensile test done on CP1200 trials [110].

Sample	T (°C)	YS(MPa)	UTS(MPa)	EI. 50%	n (6%-UTS)	Elastic Ratio
1	760	463	911	10	0,07	0,51
2	780	555	1136	6	0,07	0,50
3	800	693	1399	10	0,09	0,50
4	820	672	1357	9	0,09	0,50
5	840	663	1309	9	0,09	0,51

Table 5.6 Tension results for CP1200 measured at the initial, middle, and final regions of a processed plate [110].

Region	YS(MPa)	UTS(MPa)	El. (%)	Unif. El.	n (6%-UTS)	Elastic Ratio
I	818	1290	10	8	0,08	0,55
M	817	1270	11	8	0,09	0,57
F	827	1274	10	7	0,09	0,54

The bending test showed satisfactory results for the bending at 90° and only above 105° the plate showed signals of crack formation.

As for hole expansion, a λ value of 120% was obtained. This value is within the expected value for this steel.

5.6. LOM/SEM

5.6.1. Prior Austenite Grain Size

Vilela etching was used in the austenitized steel, as well as on the CP1100 and CP1200 to identify the prior austenite grain size. Figure 5.21 shows the result of the etching in samples that were heated to 950 °C. Figure 5.22 show a comparison between the CP1100 and CP1200 samples. The average prior austenite grain size of the three conditions can be seen in Table 5.7.

As the values of prior austenite grain size for the CP1100 and CP1200 are close to each other a t Student test was applied to these statistical values. The test was done using a two-tailed unpaired hypothesis. The result showed a 0.16 % probability that the samples have the same average prior austenite grain size.

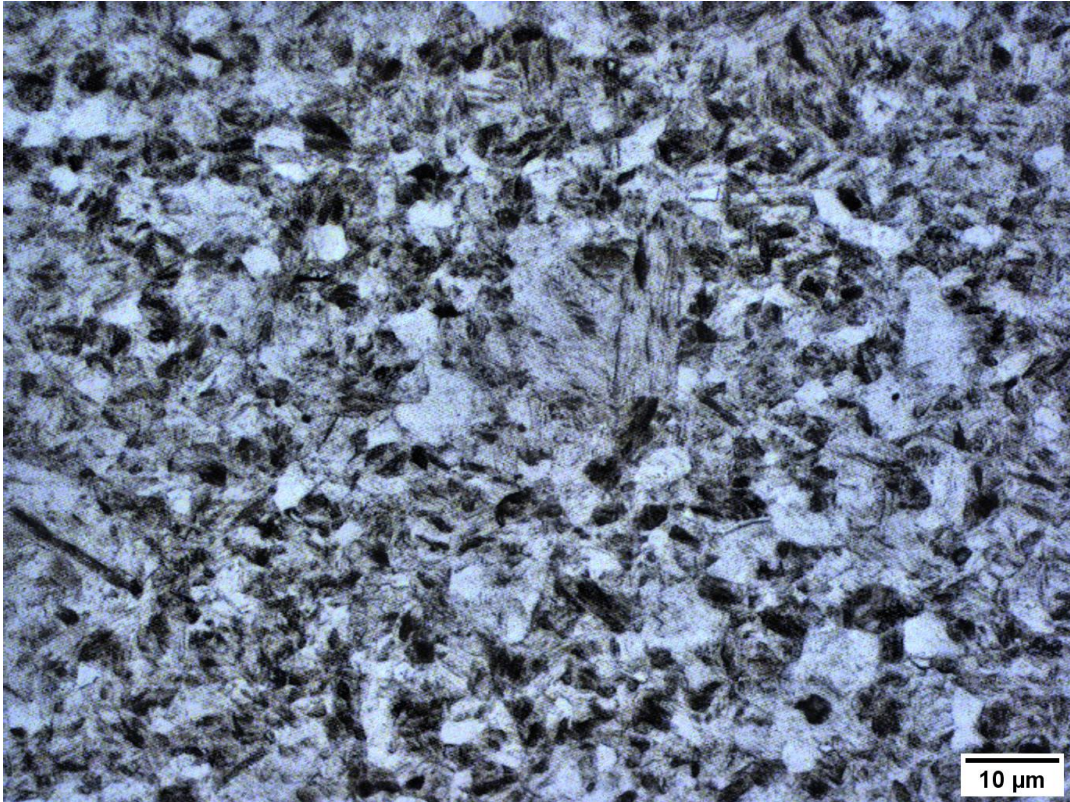


Figure 5.21 Vilela etching of the 950°C austenitized sample.

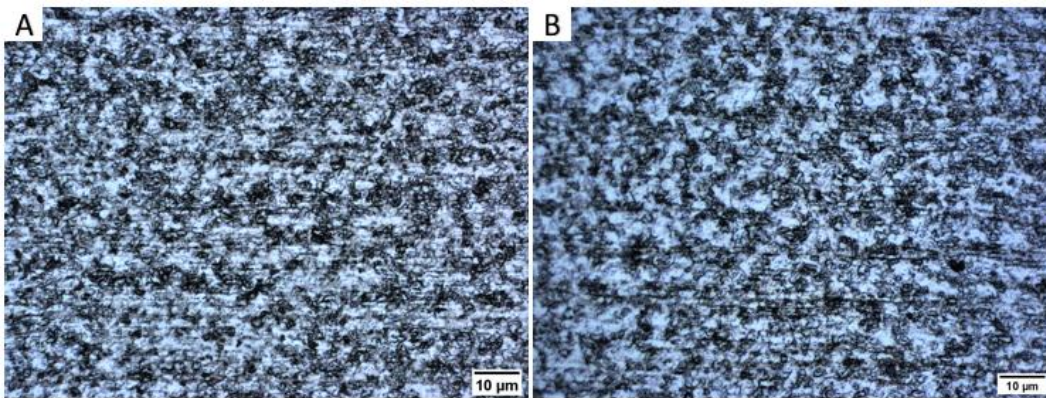


Figure 5.22 CP1100 and CP1200 Vilela etched microstructure. A – CP1100. B – CP1200.

Table 5.7 Prior Austenite Grain Size

Sample	Heat temperature	Grain Size
Austenitized	950°C	9.2 ± 1.1
CP1100	800°C	4.9 ± 1
CP1200	825°C	5.7 ± 0.8

5.6.2. Austenitization Measurement

Using Ac_1 , Ac_3 and three temperatures between these two, an austenitization curve was obtained. The microstructure of the A25 and A50 samples can be seen on Figure 5.23. The fitting of the austenitization is presented in Figure 5.24.

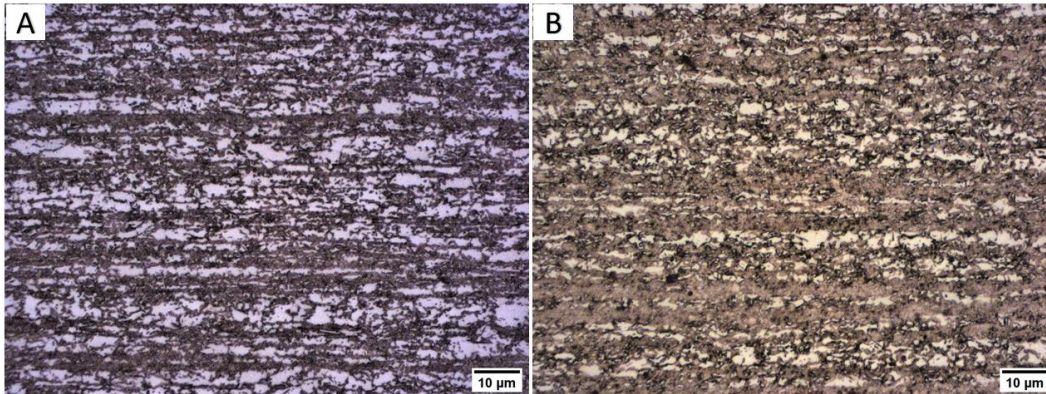


Figure 5.23 Microstructure comparison between the A25 and the A50 samples.

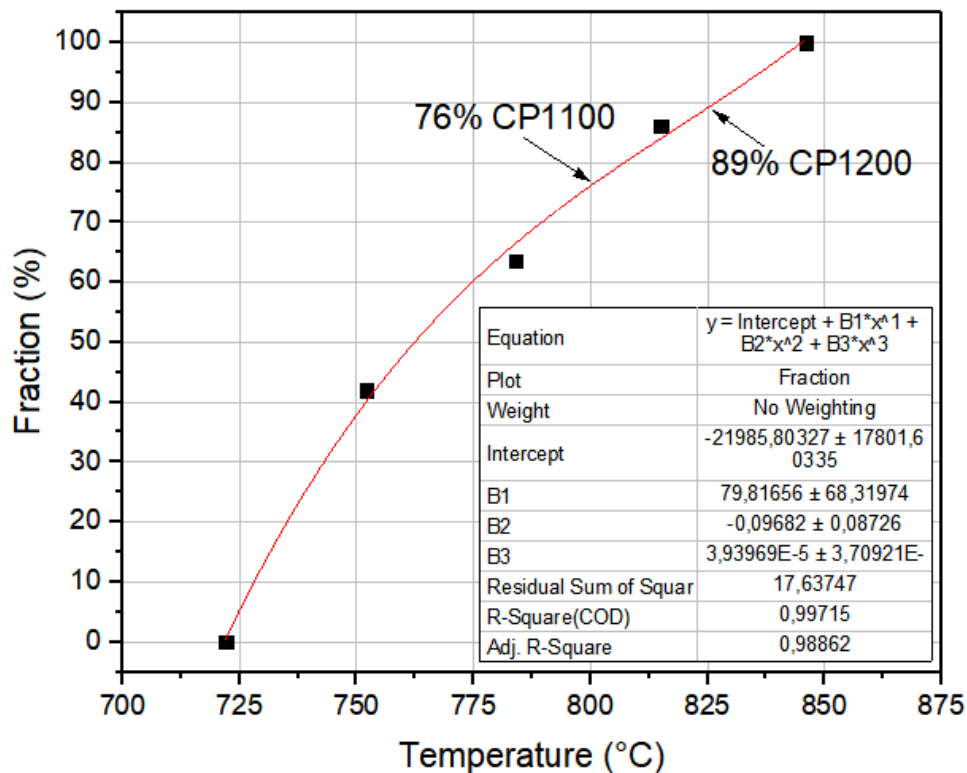


Figure 5.24 Austenite content as a function of the intercritical temperature.

5.6.3. CCT

In order to better observe the microstructures obtained during the construction of the CCT, nital and nital plus metabisulfite etched samples were analyzed using LOM and SEM. Figure 5.25 presents the LOM of the nital etched samples. The nital plus metabisulfite etched ones can be seen in Figure 5.26. As the cooling rate decreases, they present an increasing amount of ferrite; the amount was quantified and is shown in Table 5.8. A polynomial fitting was used for this data and the result can be seen in Figure 5.27.

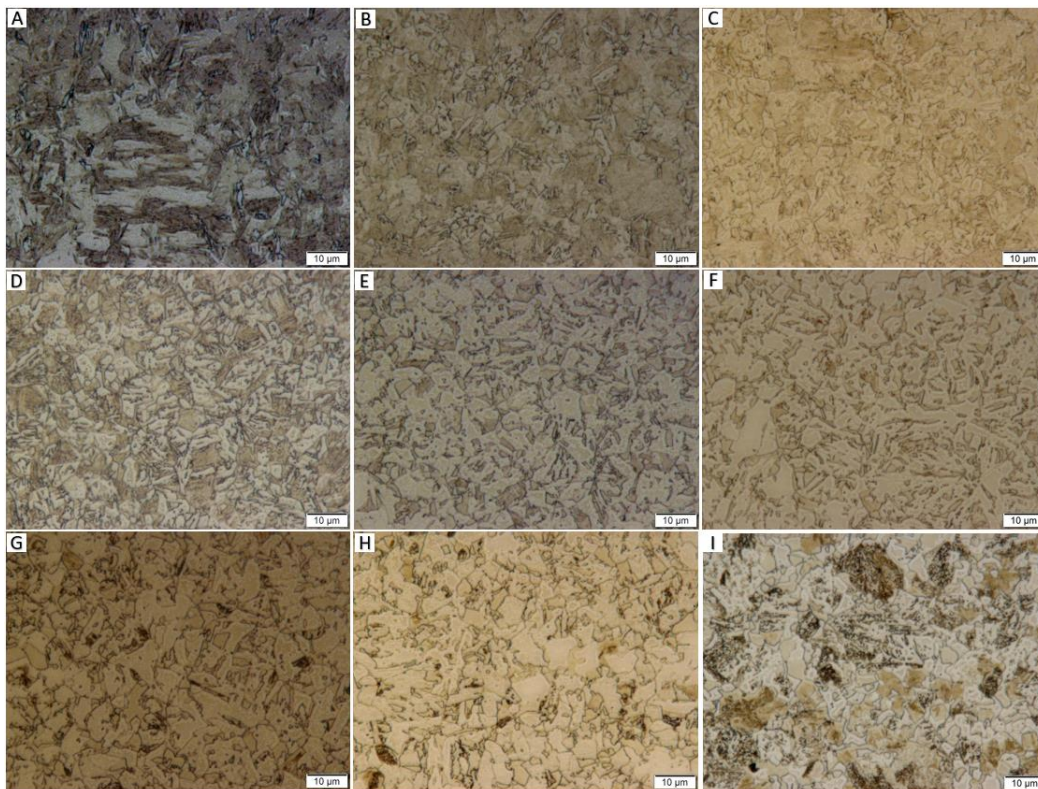


Figure 5.25 Microstructure of the CCT samples with decrease in cooling temperature seen by LOM at 2000X. A – 30 °C/s. B – 20 °C/s. C – 10 °C/s. D – 7.5 °C/s. E – 5 °C/s. F – 2.5 °C/s. G – 1 °C/s. H – 0.5 °C/s. I – 0.1 °C/s.

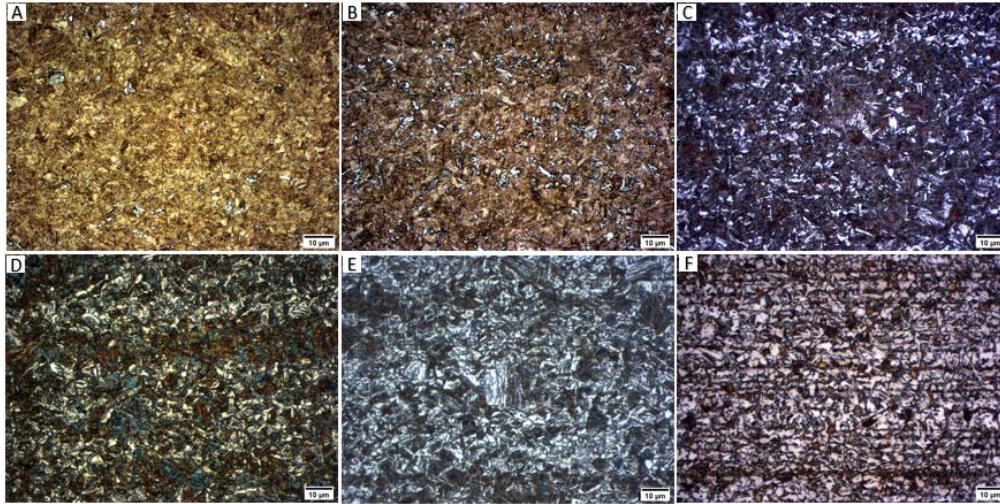


Figure 5.26 Nital + Metabisulfite etching, microstructure of the CCT samples with decrease in cooling temperature seen by LOM at 1000X. A – 30 °C/s. B – 20 °C/s. C – 10 °C/s. D - 7.5 °C/s. E – 5 °C/s. F – 1 °C/s.

Table 5.8 Ferrite quantification as a function of the cooling rate

Cooling Rate	Ferrite amount	Cooling Rate	Ferrite amount
30	0.86±0.5	5	29.73±2.63
20	2.94±0.86	1	40.13±0.88
10	17.36±4.01	0.5	45.13±2.71
7	21.28±1.55	0.2	44.15±2.12

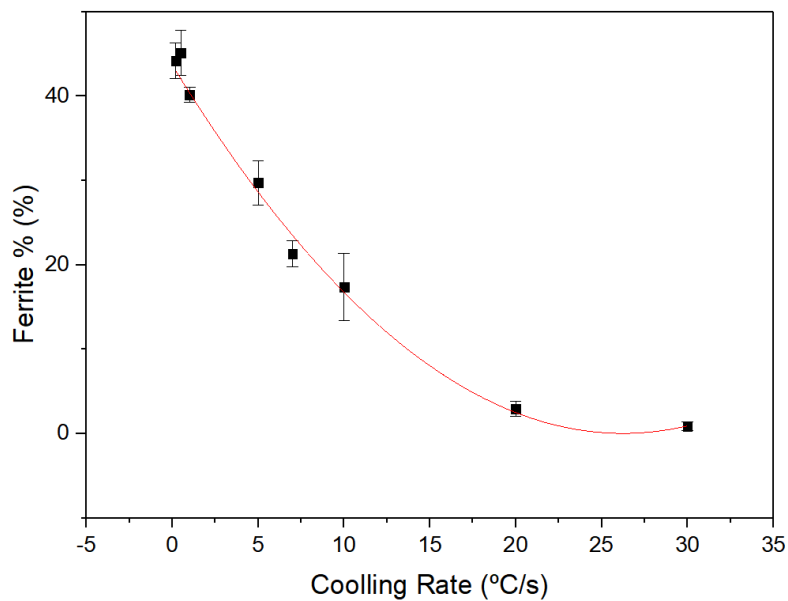


Figure 5.27 Ferrite amount depending on the cooling rate. Polynomial fit with 0.9979 R-square

The SEM images of the microstructures for the samples etched with nital can be seen in Figure 5.28. The samples cooled at the faster rate, 30 °C/s, shown in Figure 5.29, presents a martensitic microstructure, with a lot of second phase, as well as some smaller concentration of a plate like microconstituent free of second phases.

As the cooling rate is decreased, more of the precipitate free microconstituent starts to appear, accompanied by a more island like martensite/retained austenite microconstituent, as seen on the 20 °C/s cooled sample (Figure 5.30).

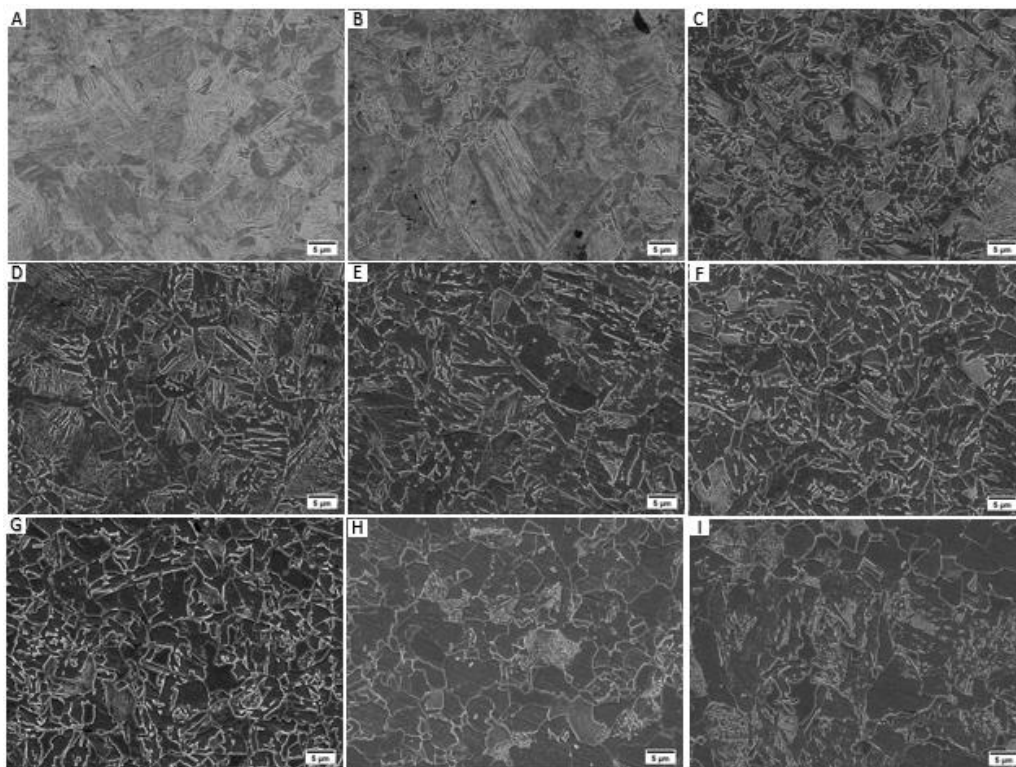


Figure 5.28 Microstructure of the CCT samples with decrease in cooling temperature seen by secondary electron imaging at 2000X. A – 30 °C/s. B – 20 °C/s. C – 10 °C/s. D – 7.5 °C/s. E – 5 °C/s. F – 2.5 °C/s. G – 1 °C/s. H – 0.5 °C/s. I – 0.1 °C/s.

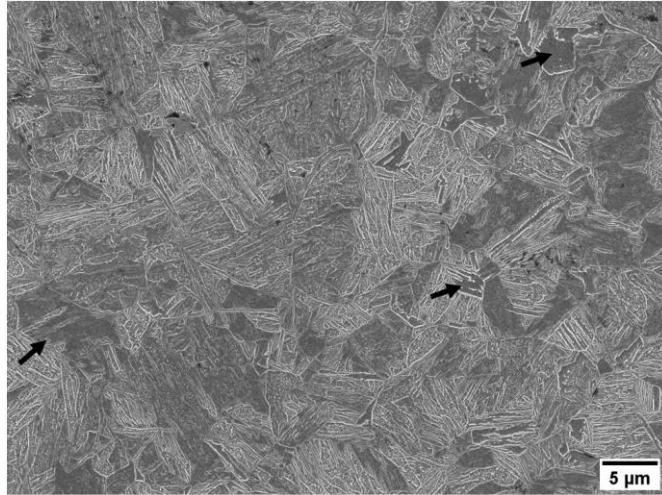


Figure 5.29 Microstructure of the 30 °C/s cooled sample seen by secondary electron imaging. Black arrows point to some precipitates free microconstituents.

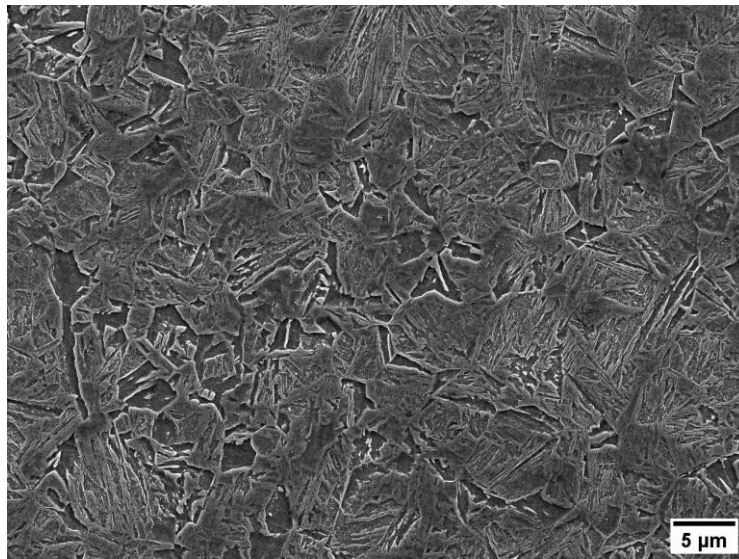


Figure 5.30 Microstructure of the 20 °C/s cooled sample seen by secondary electron imaging.

Bainite will first appear at 20 °C/s, but its identification is complicated. In the 7 °C/s some island like microconstituents that are, what appears to be an incomplete or interrupted transformation (Figure 5.31). These would be consistent with the idea of a bainite nucleation and growth interrupted by the martensitic transformation.

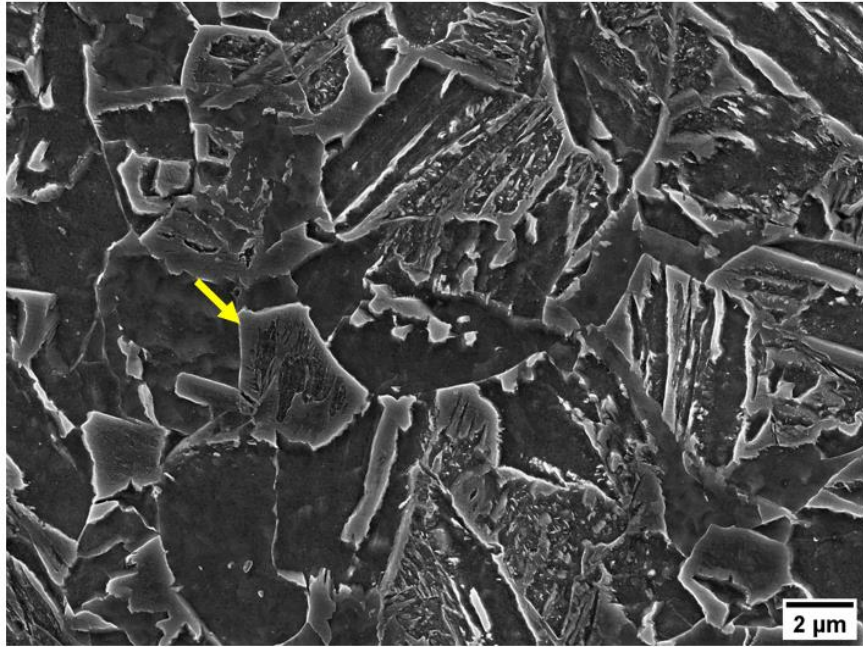


Figure 5.31 Microstructure of the 7 °C/s cooled sample seen by secondary electron imaging. Black arrow point to an island like microconstituent that presents an incomplete transformation in its interior.

As the cooling rate decreases to 2.5 °C/s, the close to fully bainitic condition, the amount of these islands increase, followed by the presence of a more flat microconstituent, likely carbide free bainite or ferritic bainite (Figure 5.32). A closer view of both these microconstituents in the 2.5 °C/s can be seen in Figure 5.33. As will be shown latter, in both CP1100 and CP1200 steels, the presence of these microconstituents were observed.

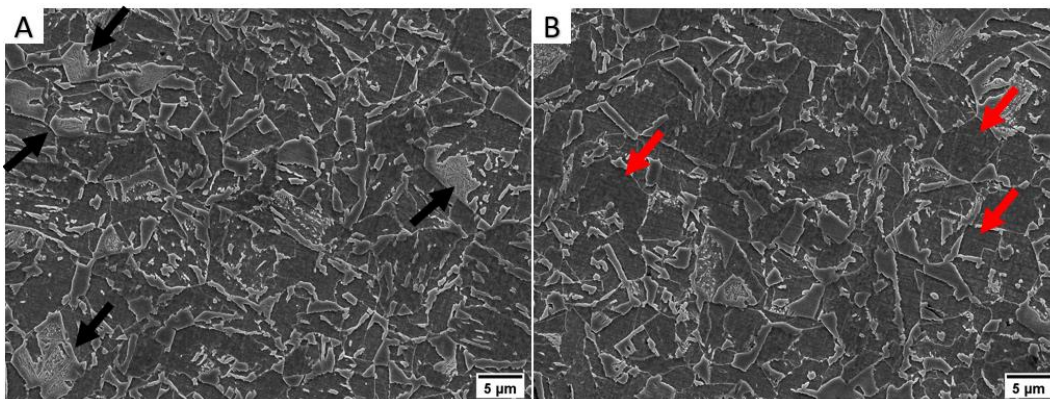


Figure 5.32 Microstructure of the 2.5 °C/s cooled sample. A and B present 2000X magnification images. Black arrows point to an island like microconstituent with an incomplete transformation in its interior. Red Arrows point to bainitic ferrite.

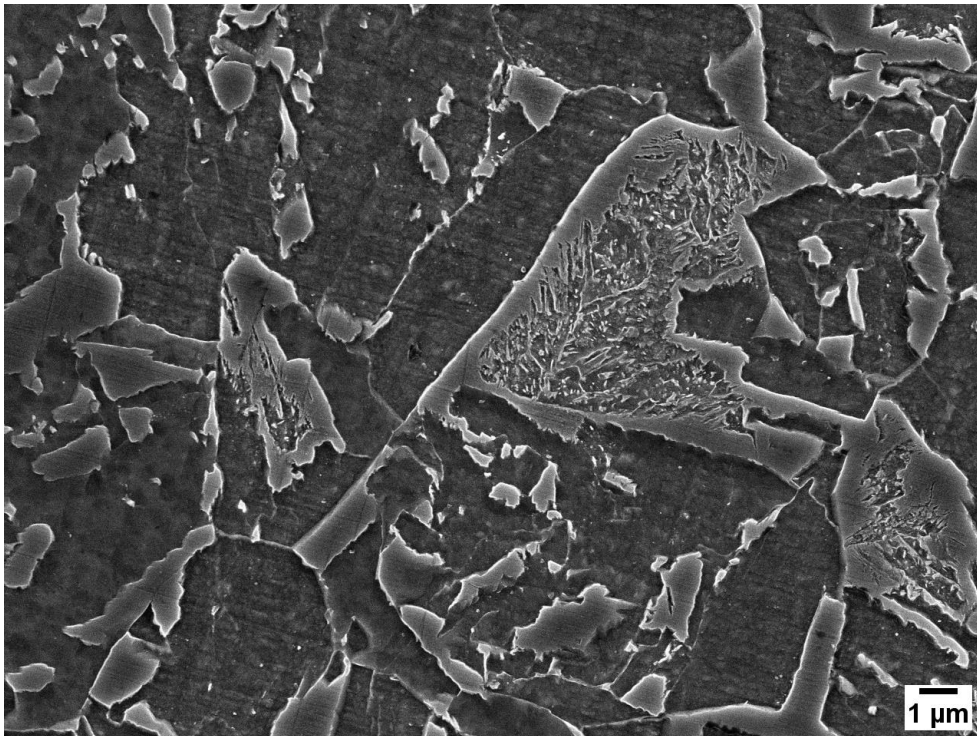


Figure 5.33 Closer view of the 2.5 °C/s cooled samples microstructure.

5.6.4. Heat Treatments

Light optical microscopy and secondary electron imaging were conducted for the more relevant heat treated samples. First, that was done for the treatments that had a 500 °C holding temperature. Figure 5.34 presents some LOM images from the CP840A500 to the CP810A500. It is possible to see that CP830 and CP820 presented some martensitic bands. Figure 5.35 shows the microstructure of the CP840, 830, 820 and 800 with 500 °C of isothermal hold, some important information can be taken from it, like the mixture of a band and a more heterogeneous microstructure in the CP830 or the presence of large martensitic bands seen in the CP820. Figure 5.36 shows some martensitic bands in the CP800A500 steel at higher magnification.

To understand the difference in hardness between the 500 °C and 450°C isothermally held sample, their microstructures were also compared (Figure 5.37). In Figure 5.38 these microconstituents can be seen at higher magnification.

As the 500 °C isothermally held samples showed undesirable martensitic bands and the 450 °C isothermally held samples showed low hardness values, an intermediary temperature was chosen for the holding in the CP1200 final treatment.

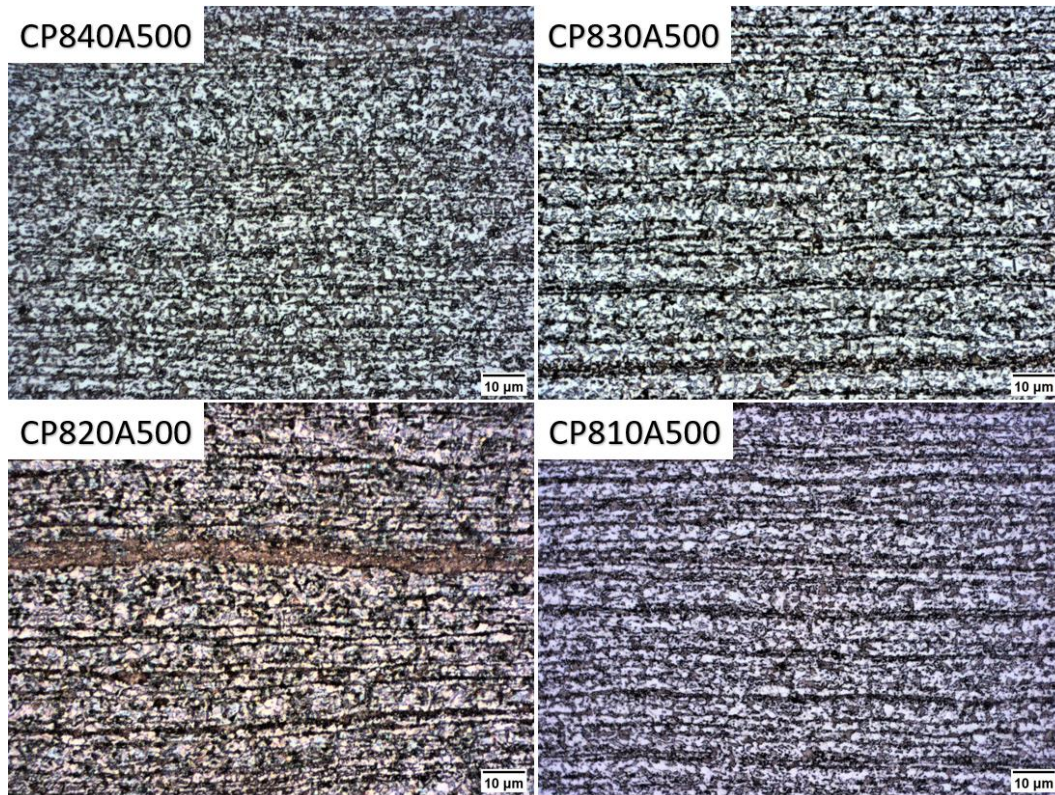


Figure 5.34 Microstructure of CPXXXA500 steels.

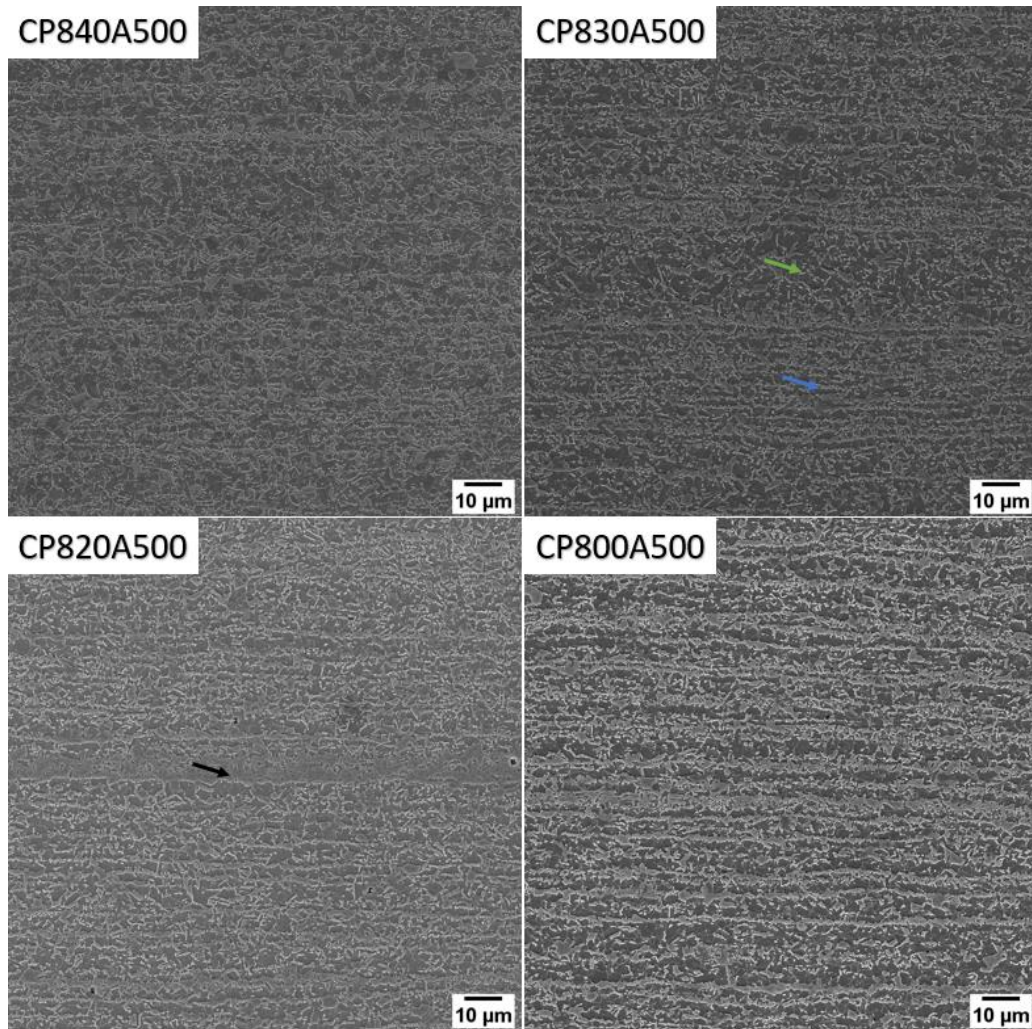


Figure 5.35 2000X magnification of CP840A500, CP830A500, CP820A500 and CP800A500 seen by scanning electron microscopy. Blue arrow point to a more banded morphology, green arrow point to a heterogeneous morphology and black arrow point to a clear martensitic banded microstructure.

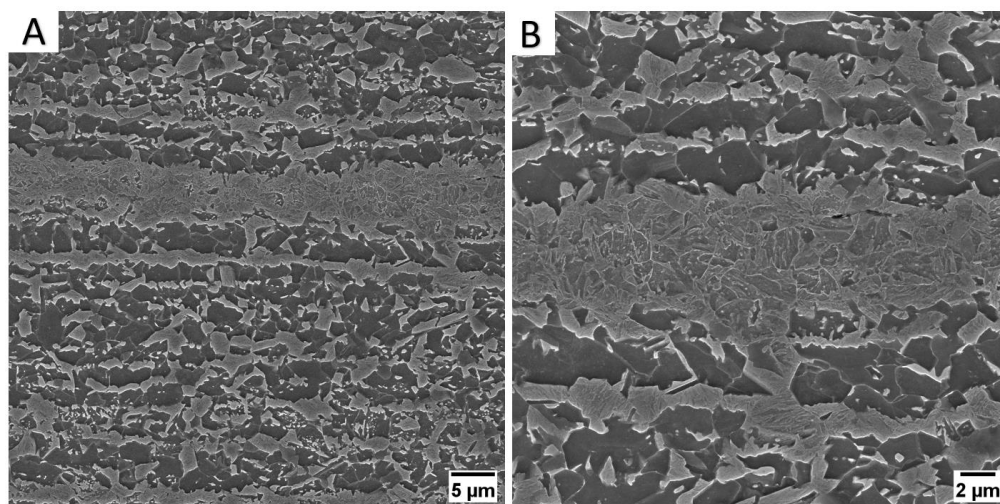


Figure 5.36 Large martensitic band in the CP800A500 seen by scanning electron microscopy. A – 5000X image. B – 10000X image.

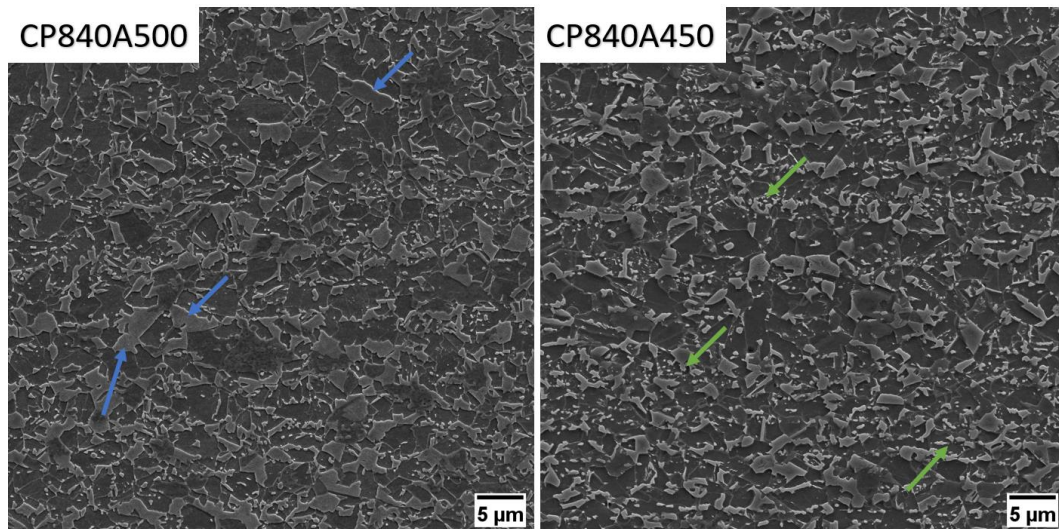


Figure 5.37 5000X magnification of CP840A500 and CP840A450 seen by scanning electron microscopy. Blue arrows point some larger grains, green arrows point to regions with small precipitates.

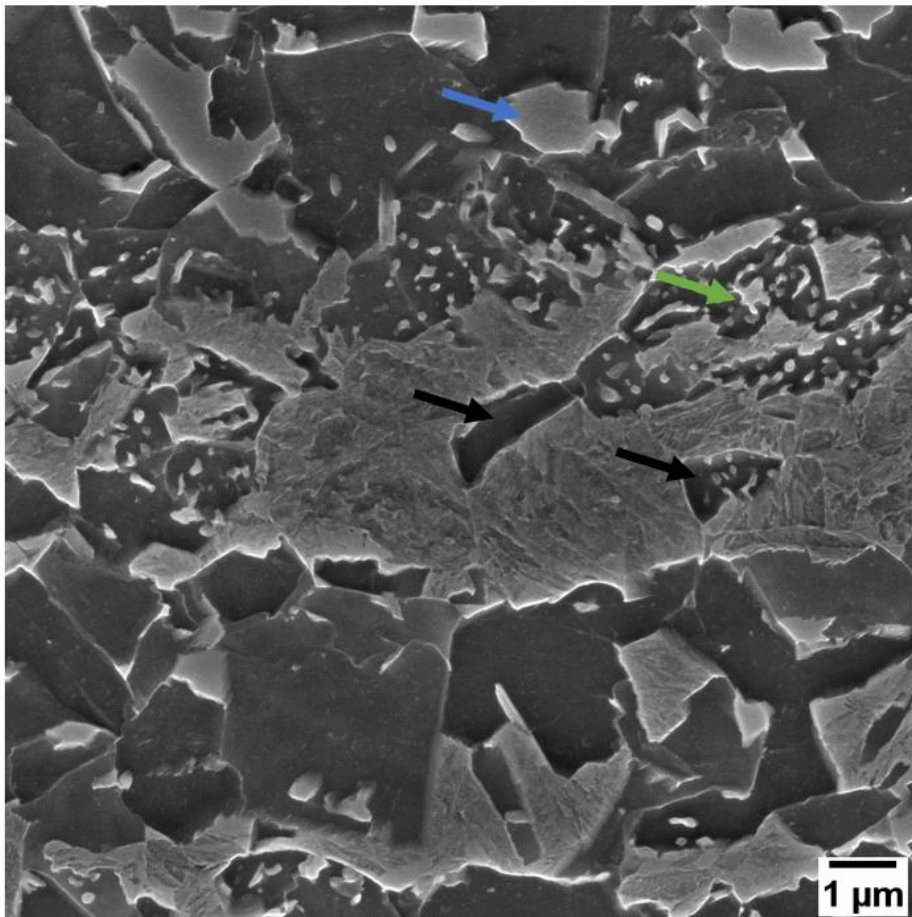


Figure 5.38 20000X micrograph of the CP800A500 steel seen by scanning electron microscopy. Black arrows point areas more prone to void nucleation, blue arrow to more traditional martensite islands, green arrow to a precipitate-filled microconstituent.

5.6.5. CP1100

The CP1100 steel had its LOM done using the Nital + sodium metabisulphite solution. Figure 5.39 show the LOM image and its WEKA segmentation. Table 5.9 has the phase quantification for the industrially produced samples.

Besides the LOM, secondary electron imaging was used to analyze the morphology and microstructure of the CP1100. Figure 5.40 shows the SEM images of the industrially produced CP1100.

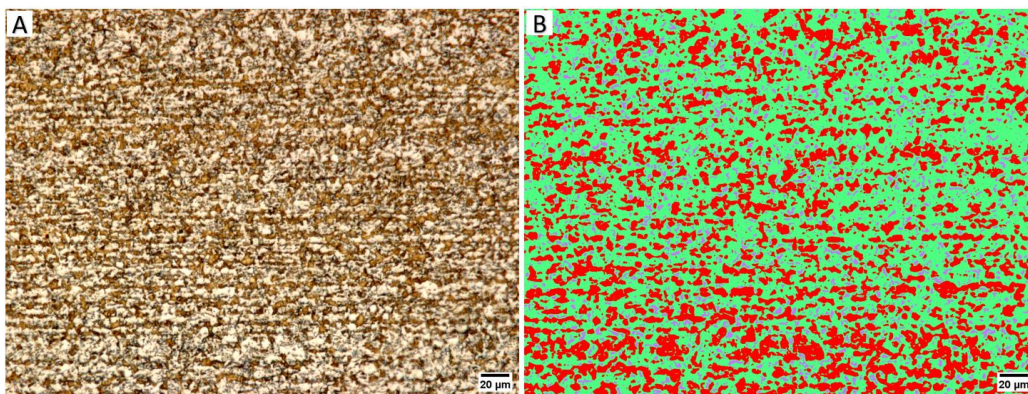


Figure 5.39 LOM 500X image of CP1100. A – Color etched surface. B – WEKA segmented image.

Table 5.9 Quantification of CP1100 LOM images

Ferrite %	Bainite/Martensite %	Retained Austenite %
53.9 ± 3.7	45.3 ± 3.6	0.78 ± 0.25

Figure 5.40A clearly shows the two distinguishing morphological characteristics of industrially produced steel microstructure, some highly banded regions, which can lead to void nucleation, and regions more heterogeneously distributed. Those banded and unbanded regions have an average of 40 µm of width.

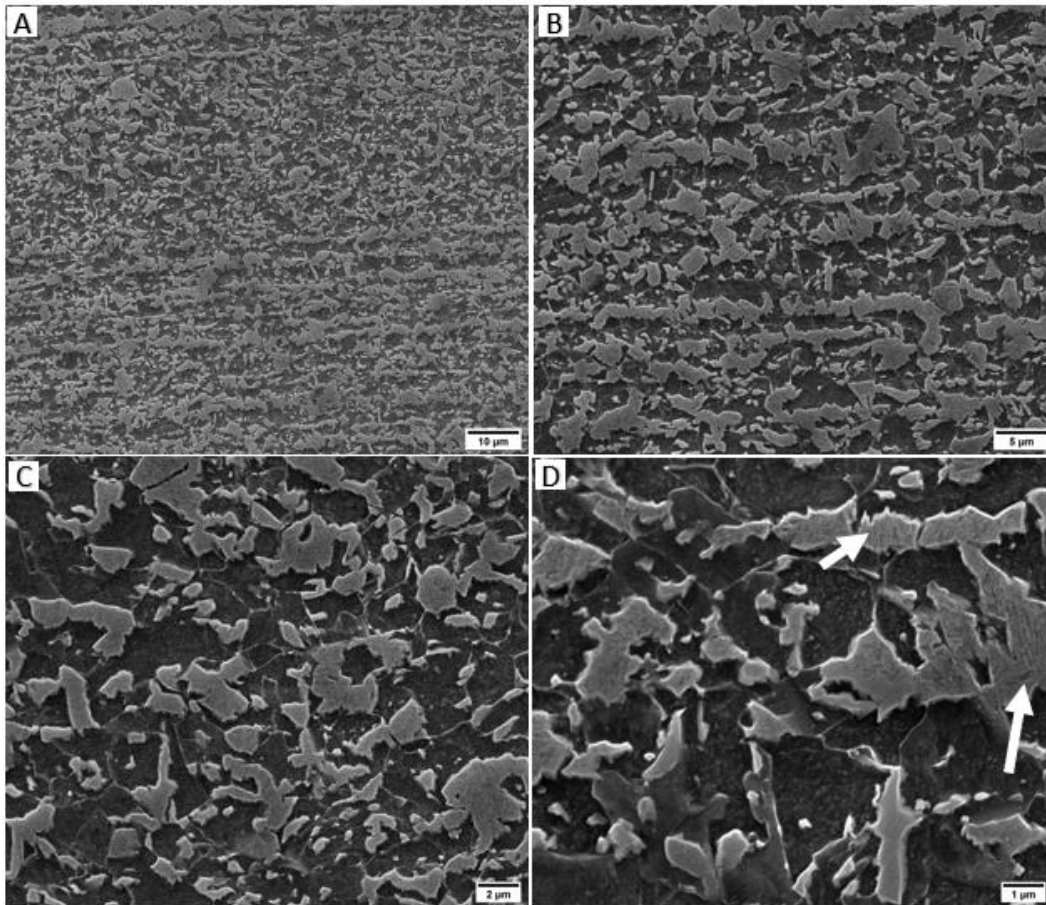


Figure 5.40 Secondary electron imaging of the industrial produced CP1100. A – 2500X. B – 5000X. C – 10000X. D – 20000X, white arrows point to over etching in martensitic/austenitic islands.

5.6.6. CP1200

LOM and SEM were likewise used to evaluate the CP1200 steel. Figure 5.41 presents an example of LOM image of the CP1200 and Figure 5.42 shows the same for SEM. Quantification of the LOM for the CP1200 can be seen in Table 5.10.

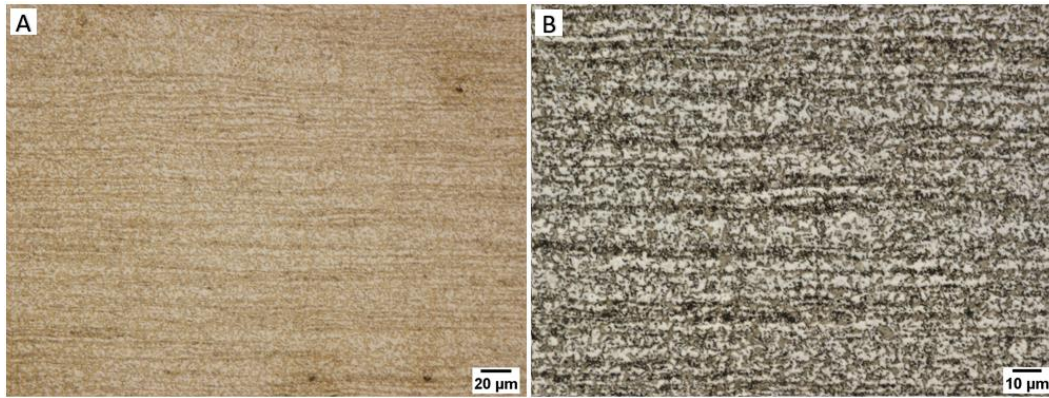


Figure 5.41 LOM imaging of the CP1200. A – 500X magnification. B – 1000X magnification with improved contrast.

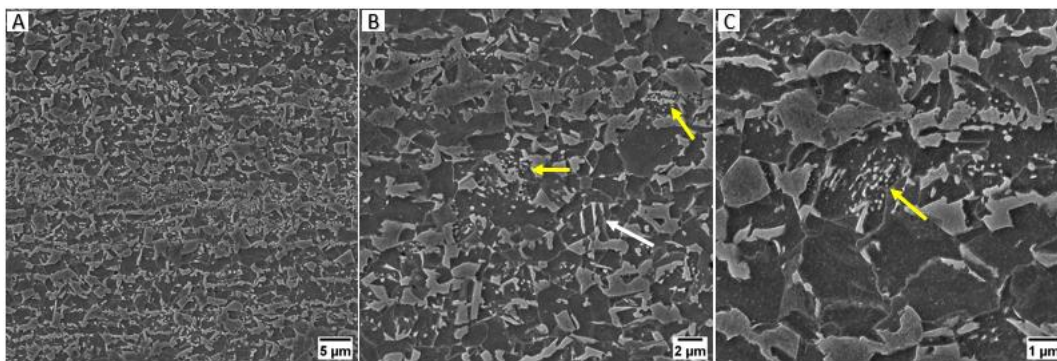


Figure 5.42 SEM image of CP1200. A – 2000X magnification. B – 5000X magnification. C – 20000X magnification. White arrow points to plate like microstructure, yellow arrows point small second phases in a highly etched grain.

Table 5.10 LOM quantification of the CP1200 microstructure

Steel	Ferrite %	Bainite/Martensite %	Retained Austenite %
CP1200	47.4 ± 1.97	50.34 ± 1.64	0.4 ± 0.18

5.7. AFM

5.7.1. CP1100

Atomic force microscopy was done following section 4.6. Figure 5.43 presents a sequence of 60x60, 40x40, 20x20 and 10x10 μm maps. Following the report by Ros-Yáñez and associates [95], the lower grains were identified as ferrite, the higher as martensite and the 2 intermediary levels as bainite. The last consideration was done because more than one kind of bainite is expected in this microstructure.

One apparent difference between the AFM and SEM images is the number of precipitates and their contrast with the rest of the microstructure. In SEM those precipitates are not as apparent and do not influence the quantification. In AFM they strongly change the quantification process because they have a height close to that of the martensite, and can be wrongly segmented as such.

In order to identify the microconstituents, the height and roughness of some regions were measured, as seen in Figure 5.44. Table 5.11 presents the measurements results.

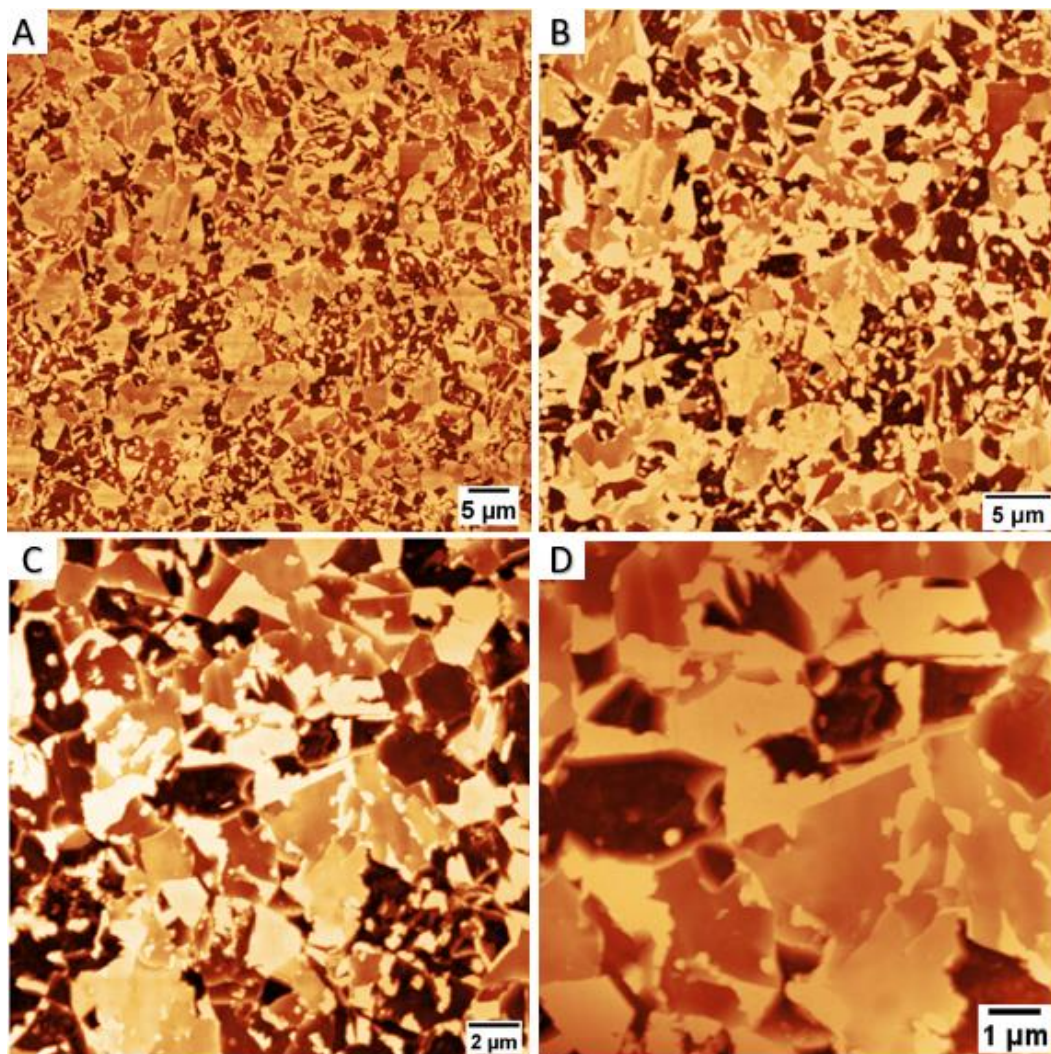


Figure 5.43 Atomic Force Microscopy imaging of the CP1100 steel. A – 60x60 μm map. B – 40x40 μm map. C – 20x20 μm map. D – 10x10 μm map.

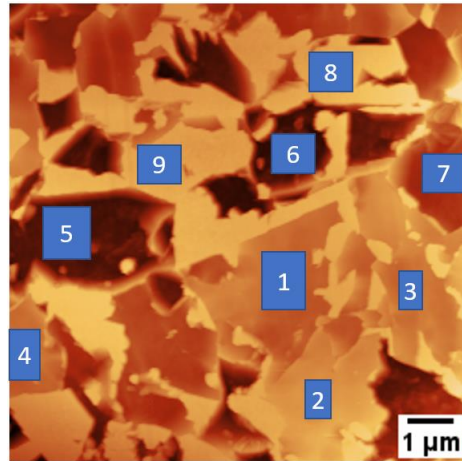


Figure 5.44 Regions used for measurement of the height and roughness of the microconstituents.

Table 5.11 Measurements done over the AFM image

Measure	Height (nm)	Mean Roughness (nm)
1	-0,2	73,71
2	71	10,57
3	21,57	7,7
4	5,04	11,42
5	-171,9	12,38
6	-174,5	24,97
7	-58,46	15,17
8	99,8	6,6
9	84,42	4,5

The first measurement shows a peculiar result with a high roughness. The reason for that becomes clear in Figure 5.45 where a 3D image of the 10x10 μm map can be seen. The grain whose faces are at an angle with the normal plane will present results that cannot be compared. Measurements like those were then disregarded when taking the average of the phases; but still, there is a clear segmentation problem when you consider that the interfaces are not sharp, presenting a gradient in height, which limits, or at least complicates, the use of AFM for that finality.

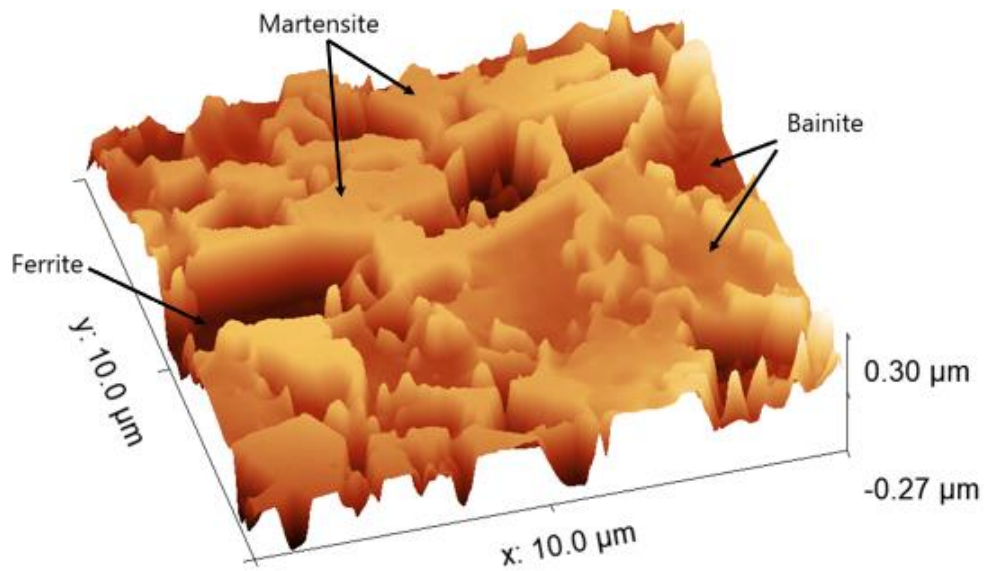


Figure 5.45 AFM 3D map of the CP1100 steel.

5.7.2. CP1200

AFM characterization on CP1200 is shown in Figure 5.46 a sequence of 60x60, 40x40, 20x20 and 10x10 μm maps. The microconstituent identification was also done considering the height of the grain as seen in Figure 5.47. The three-dimensional 10x10 μm map is in Figure 5.48.

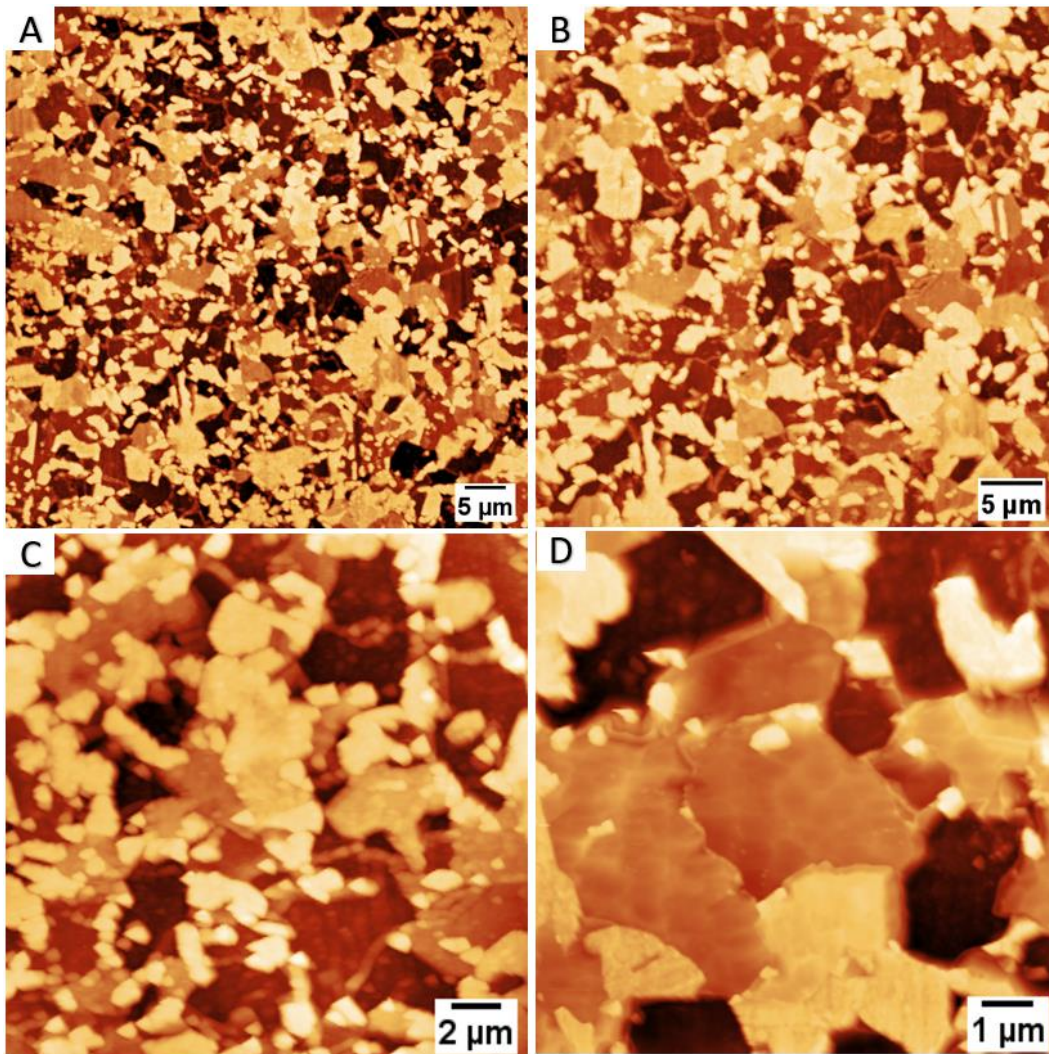


Figure 5.46 Atomic Force Microscopy imaging of the CP1200 steel. A – 60x60 μm map. B – 40x40 μm map. C – 20x20 μm map. D – 10x10 μm map.

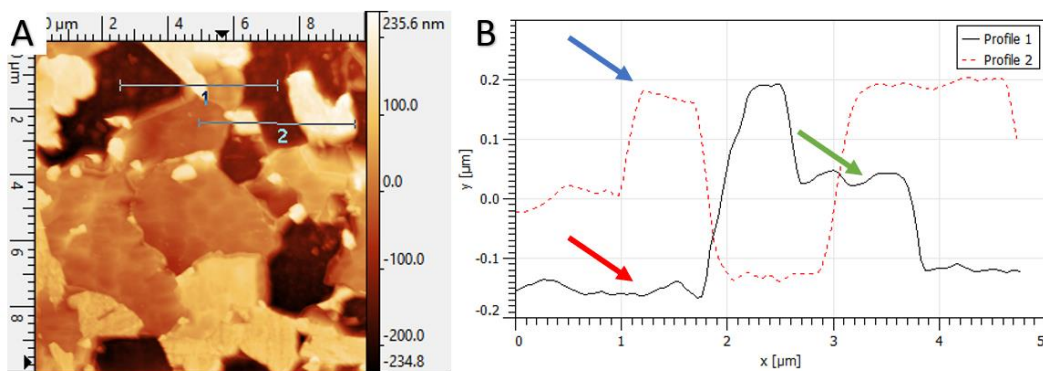


Figure 5.47 AFM profile on CP1200 steel. A – AFM image with two profile lines. B – Height following the profile lines. Blue arrow point to martensite height, green arrow to bainite and red arrow to the ferrite.

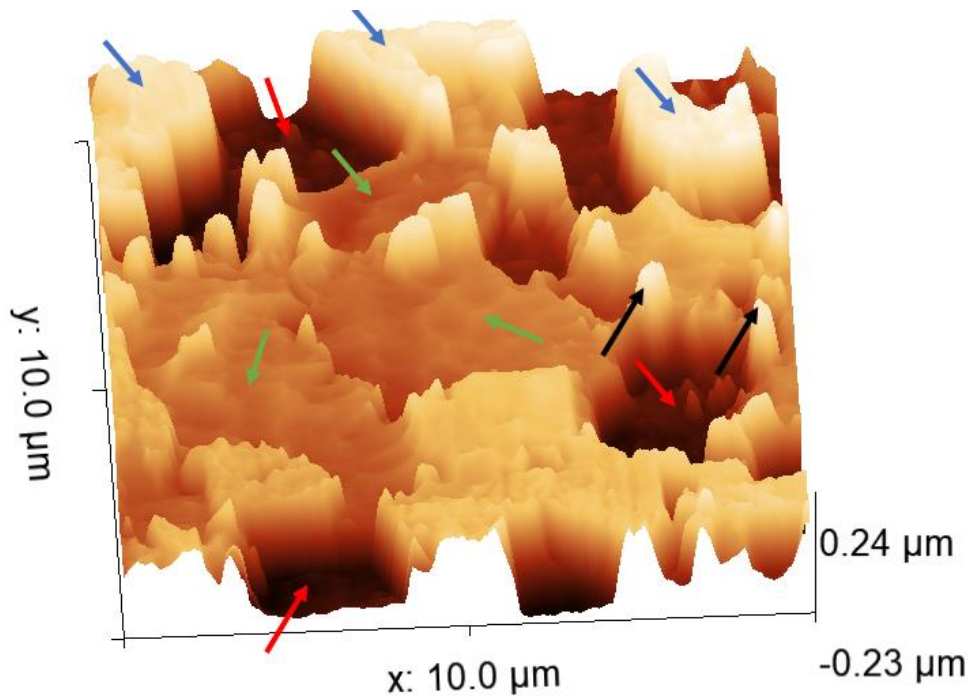


Figure 5.48 AFM 3D map of the CP1200 steel. Blue arrows points to martensite, green arrows to bainite, red arrows to ferrite and black arrows to precipitates.

5.8. EBSD

5.8.1. CCT Curve

To characterize how bainite would show up in EBSD, an analysis was done in the 2.5 °C/s continuously cooled sample, which should be nearly pure bainitic. The results can be seen in Figure 5.49. The band contrast map (Figure 5.49 A) has a better contrast than the band slope (Figure 5.49 B), but the band slope has a better definition at the boundaries. When used together, they provide a good contrast with high-definition edge. This map does not differ much from the regular CP steel. The reason is that the scale of the map (gray scale used) is set automatically, allowing the best exhibition possible according to the software. That makes hard to compared it with the CP steels results.

The Kernel Average Misorientation (Figure 5.49 D) and the Grain Orientation Spread (Figure 5.49 E) shows a highly deformed microstructure, with a lot of zero solution inside the grains. When the KAM and GOS maps are put together (Figure 5.49 F), a mixture of blue and green is seen all over

the map. Later, in the CP treated samples, the same kind of mixture can be seen in grains identified as bainite. In Figure 5.50 the same behavior of Figure 5.49 can be seen at higher magnification.

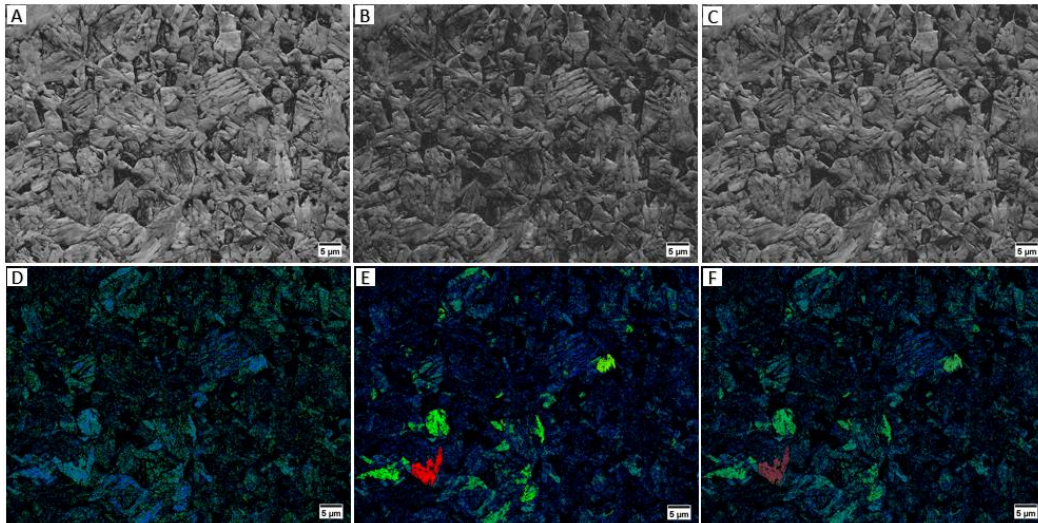


Figure 5.49 EBSD analysis of the 2.5 °C/s cooled sample with low magnification. A – Band Contrast. B – Band Slope. C – Band contrast plus Band Slope. D – Kernel Average Misorientation. E – Grain Orientation Spread. F – Kernel Average Misorientation plus Grain Orientation Spread.

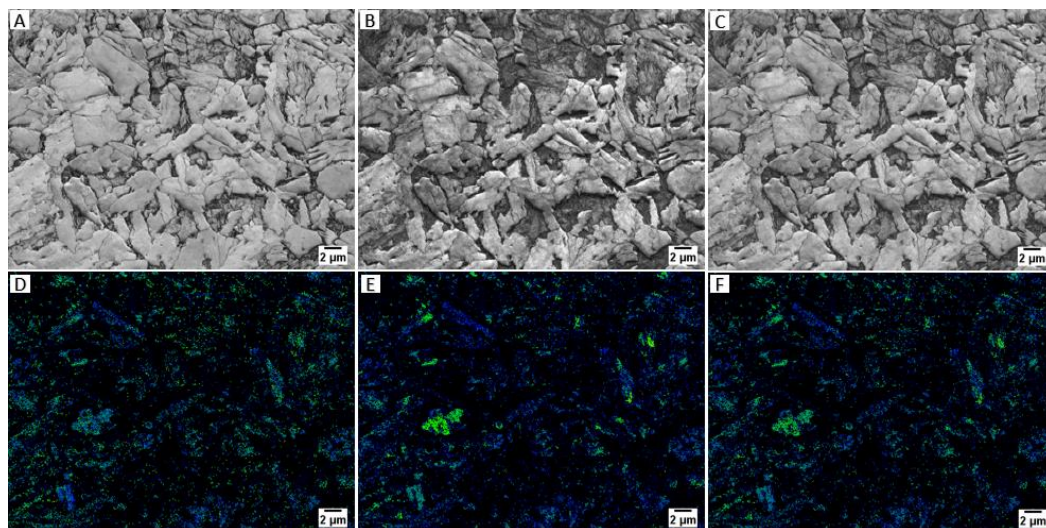


Figure 5.50 EBSD analysis of the 2.5 °C/s cooled sample with a higher magnification. A – Band Contrast. B – Band Slope. C – Band contrast plus Band Slope. D – Kernel Average Misorientation. E – Grain Orientation Spread. F – Kernel Average Misorientation plus Grain Orientation Spread.

5.8.2. CP1100

EBSD analysis was done for the industrially processed and the dilatometric treated samples. Figure 5.51 shows the band contrast image for both cases. A simple analysis of these maps can already indicate that the dilatometric treated sample has a smaller grain size and a higher concentration of phases with higher dislocations contents (bainite or martensite). Figure 5.52 shows the different maps used to identify the phases. Band contrast (Figure 5.52A) is used together with qualitative carbon concentration seen by EDS (Figure 5.52B) to confirm the martensitic regions. Those are usually not indexed, giving zero solution. The phase ID map (Figure 5.52D) is used to identify the retained austenite. Kernel average misorientation (Figure 5.52E) and the grain orientation spread (Figure 5.52F) are combined to distinguish the bainite from the ferrite. Figure 5.53 presents an example of a fully segmented image with all the phases identified in the industrially produced steel. Similarly, Figure 5.54 presents the result for the dilatometric treated sample.

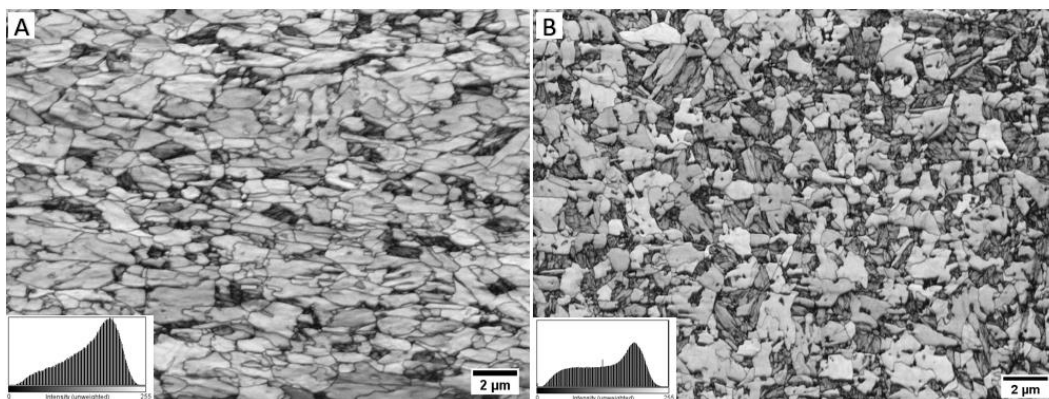


Figure 5.51 Band contrast map for CP1100. A – Industrial processed. B – Dilatometric treated.

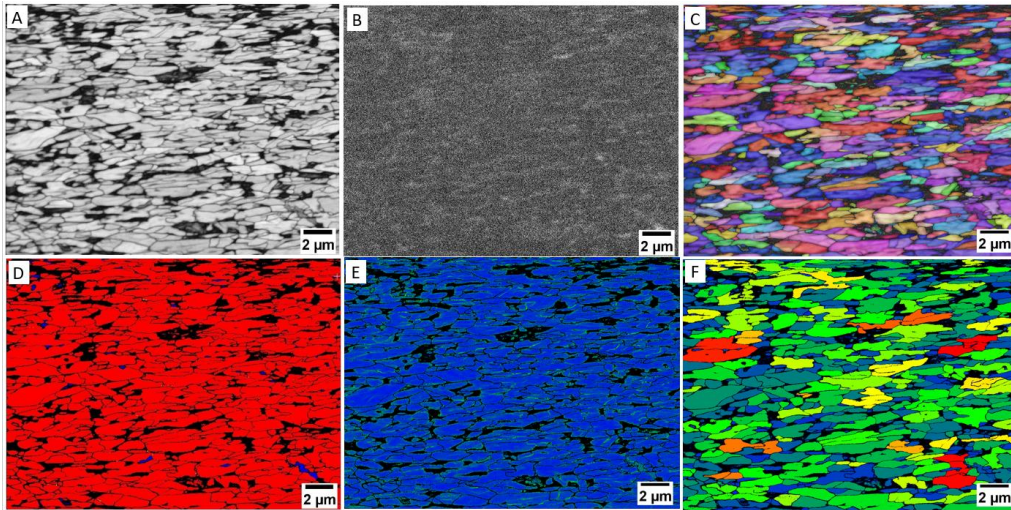


Figure 5.52 EBSD/EDS analysis of an industrially produced CP1100. A – Band contrast. B – Carbon EDS map. C – IPF z + Band contrast map. D – Phase ID map. E – KAM map. F – GOS map.

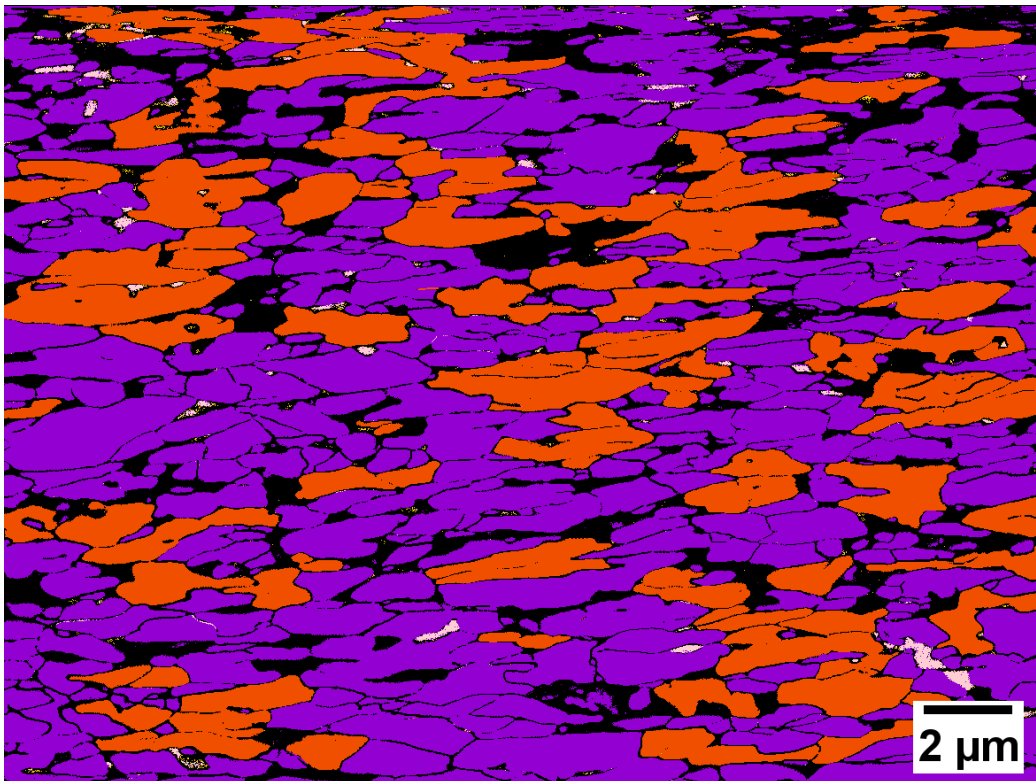


Figure 5.53 Fully identified EBSD map of industrially produced CP1100. Magenta ferrite, red bainite, black martensite, white retained austenite.

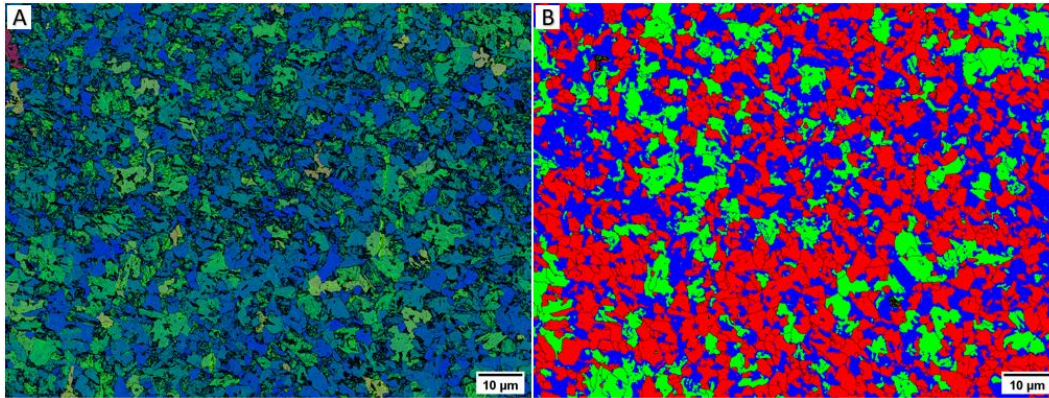


Figure 5.54 EBSD map of dilatometric treated CP1100. A – KAM + GOS. B – Segmented map, red ferrite, green bainite, blue martensite.

The sum of the EBSD maps results for the industrially produced CP1100 can be seen in Table 5.12. The EBSD quantification comparison for the industrially produced and dilatometric treated samples can be seen in Table 5.13.

Table 5.12 Sum of all the EBSD map microstructural quantification for the industrial CP1100

Sample	Ferrite %	Bainite %	Martensite %	RA %
Map 1	60,3	16,9	22,5	0,2
Map 2	55,6	20,7	21,4	2,4
Map 3	52,2	26,0	19,6	2,2
Map 4	61,3	15,5	22,6	0,7
Map 5	56,9	23,3	19,2	0,7
Map 6	51,5	24,1	22,1	2,4
Average	56,3	21,1	21,2	1,4

Table 5.13 EBSD quantification of CP1100 steel

Sample	Ferrite %	Bainite %	Martensite %	RA %
Industrial Produced	56.3 ± 4	21.1 ± 4.1	21.2 ± 1.5	1.4 ± 1
Dilatometric Treated	53.6 ± 7.6	19.1 ± 7.1	27,0 ± 0.1	0.1

5.8.3. CP1200

An example of the EBSD analysis done is shown in Figure 5.55. Some scratches can be seen in the EBSD map, but Figure 5.56 shows that in the secondary electron image the scratches cannot be easily seen. This illustrates that the EBSD is a very powerful characterization technique; and

how sensitive to the sample preparation the results are. Table 5.14 presents the sum of the phase quantification for the CP1200.

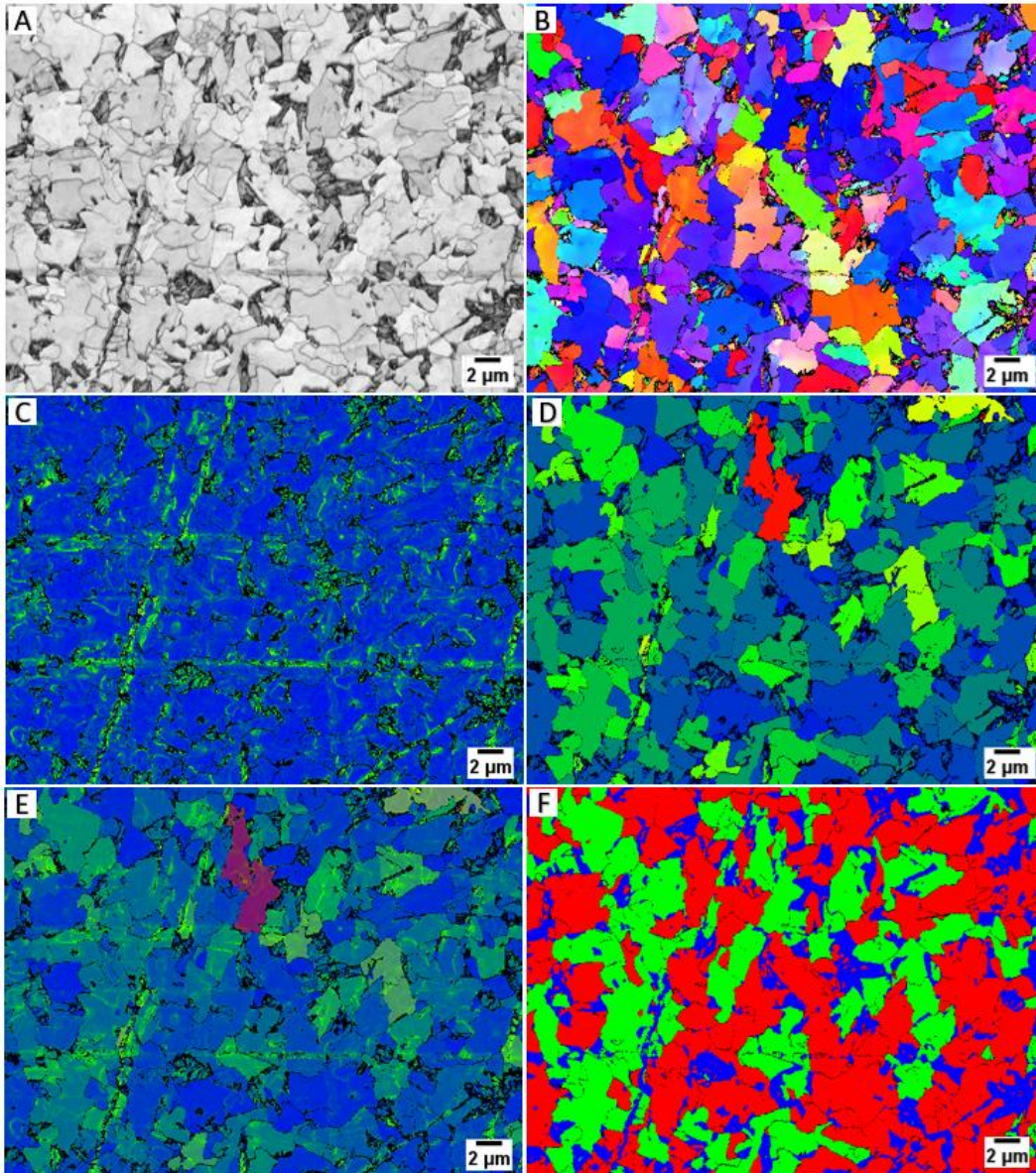


Figure 5.55 EBSD map for the steel CP1200. A – Band contrast map. B – IPF z map. C – KAM map. D – GOS map. E – KAM + GOS. F – Fully segmented map, red ferrite, green bainite, blue martensite.

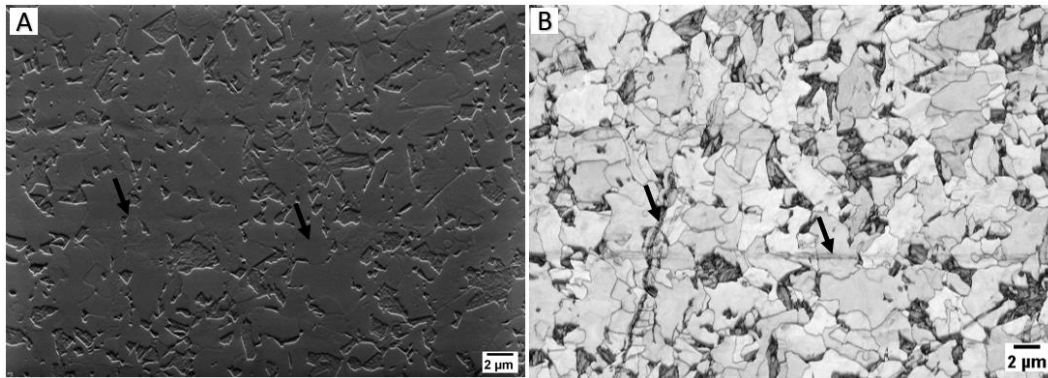


Figure 5.56 Comparison between the secondary electron image and the Band Contrast. A – SE image with channeling contrast. B – Band Contrast

Table 5.14 Sum of all the CP1200 EBSD maps microstructural quantification.

Sample	Ferrite %	Bainite %	Martensite %	RA %
Map 1	49,0	34,1	16,5	0,4
Map 2	43,1	36,7	19,5	0,7
Map 3	37,5	38,7	23,1	0,7
Map 4	49,2	35,4	15,1	0,3
Map 5	51,5	36,6	11,8	0,2
Map 6	50,8	36,4	12,1	0,2
Map 7	45,9	35,2	18,7	0,2
Average	46,7	36,2	16,7	0,4

5.9. TEM

TEM was used to confirm the presence of the phases and to take a closer look at the microstructure morphology. Figure 5.57 shows the microstructure found in the CP1100. From Figure 5.57 A to Figure 5.57C there is an increase in magnification. Figure 5.57D presents an enhance local contrast (CLAHE) filter. This filter allows, in some cases, the revelation of small details of the sample and was used when advantageous for the phase's identification. Figure 5.58 shows a relatively frequent plate like morphology; Figure 5.58B shows that the CLAHE filter allows an easier identification of a transformed retained austenite, similar to the findings of Sugimoto and associates [122]. Figure 5.59 shows a ferrite grain, with cementite intergranular precipitates. Figure 5.60 confirms the presence of

retained austenite in the CP1100. The morphology of this retained austenite is similar to that reported by Han and associates [46].

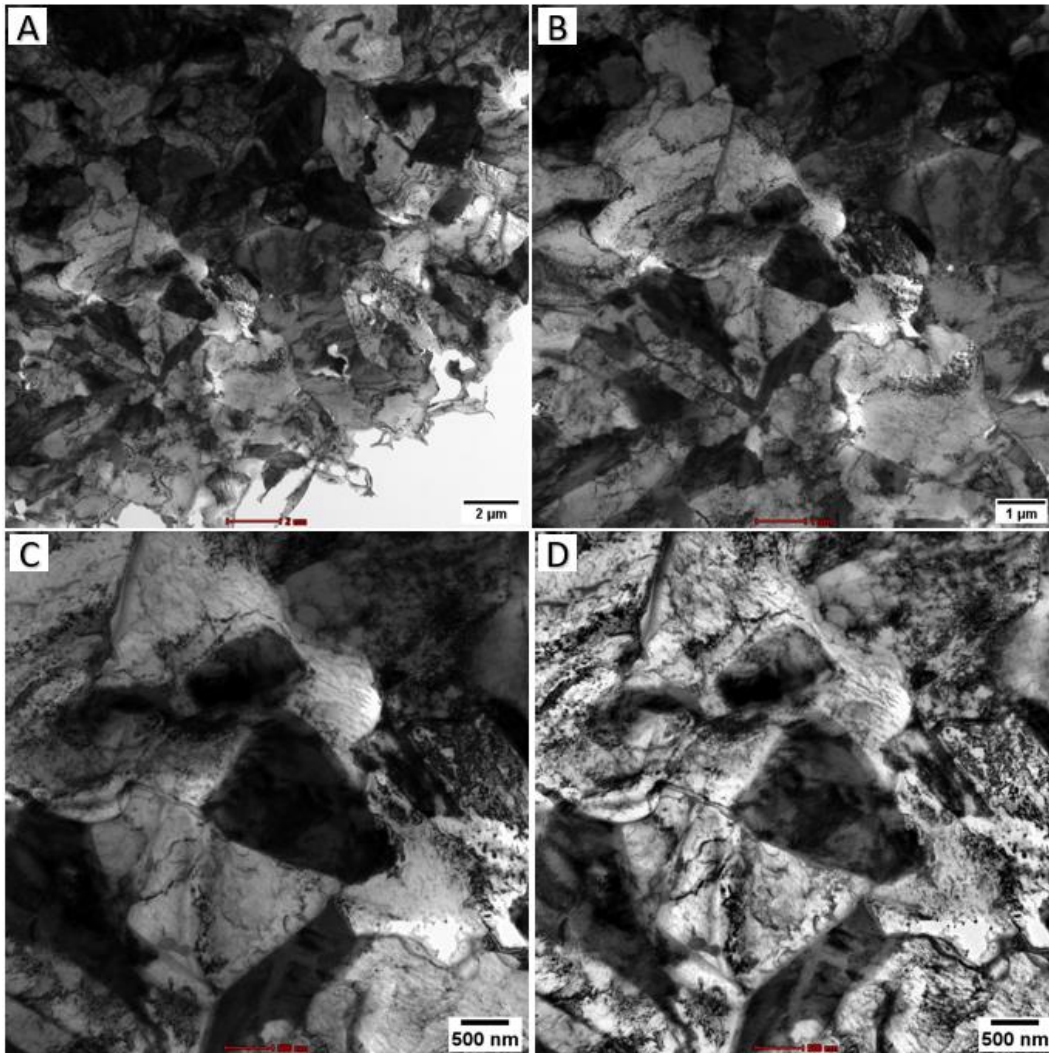


Figure 5.57 TEM imaging of CP1100. A, B and C – show the same region with increasing magnification. D – uses an image processing to reveal smaller details, such as the dislocations.

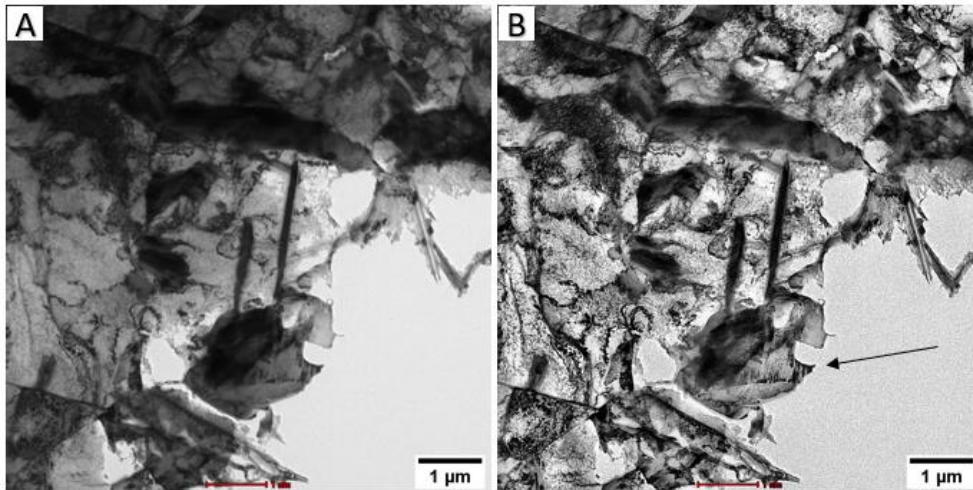


Figure 5.58 TEM image of CP1100. A – Interesting plate like morphology. B – Image enhanced contrast of the same regions reveals a martensitic transformed retained austenite (black arrow).

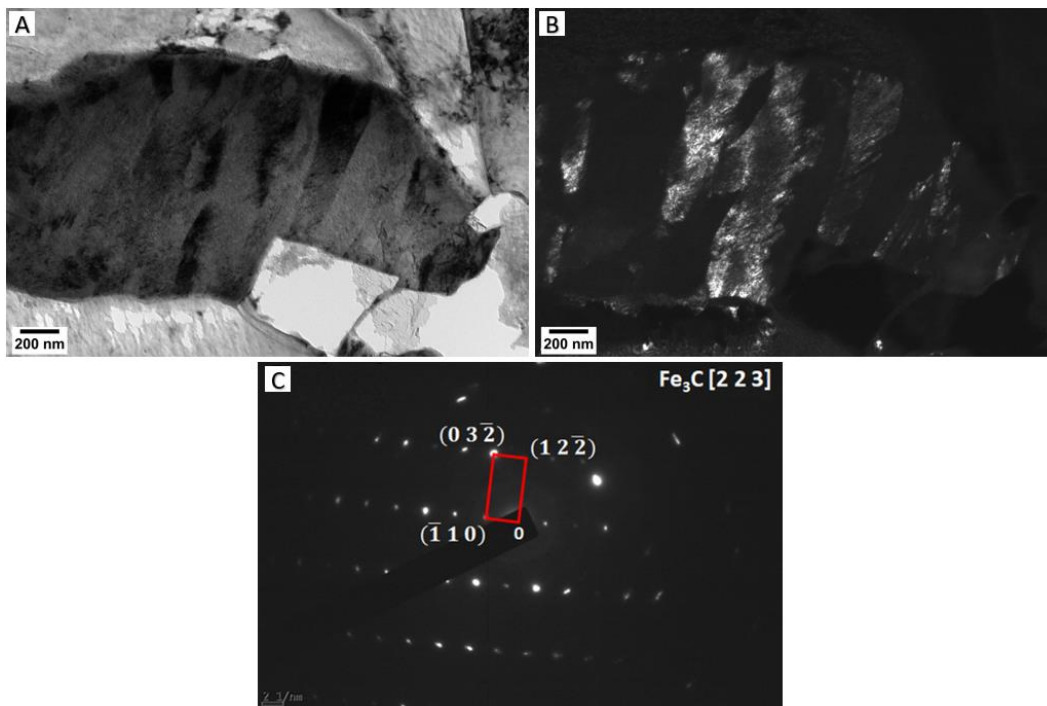


Figure 5.59 Ferrite grain with cementite plates. A – Bright field image of the ferrite grain. B – Dark field image. C – Indexed electron diffraction.

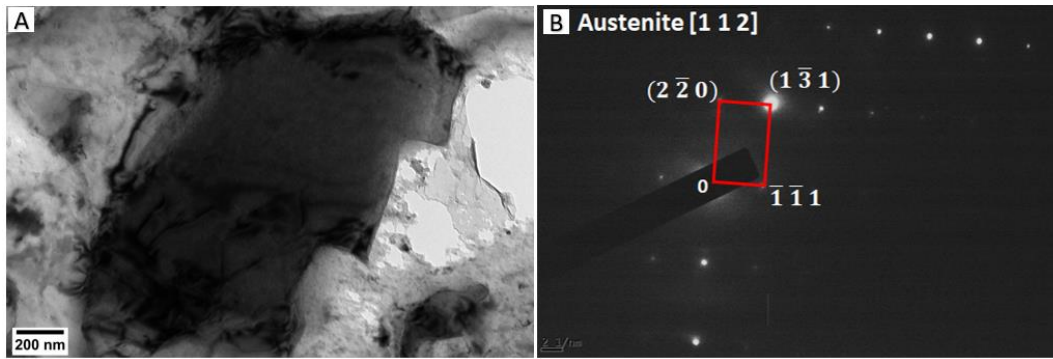


Figure 5.60 Bright field TEM image of austenite grain. A – Bright field image. B – Indexed electron diffraction.

As the CP1200 was produced in the dilatometer, its TEM samples were obtained as FIB lift-outs. Unfortunately, due to the pandemic, access to the TEM was restricted and only a single section could be done. Figure 5.61 shows some images from the CP1200 lift-out sample. Similar to the CP1100, plate like precipitates can be seen inside some grains Figure 5.61B, but diffraction could not be done to confirm them as cementite. Some regions (Figure 5.61C) also appear to be martensite transformed from retained austenite, like was seen in the CP1100.

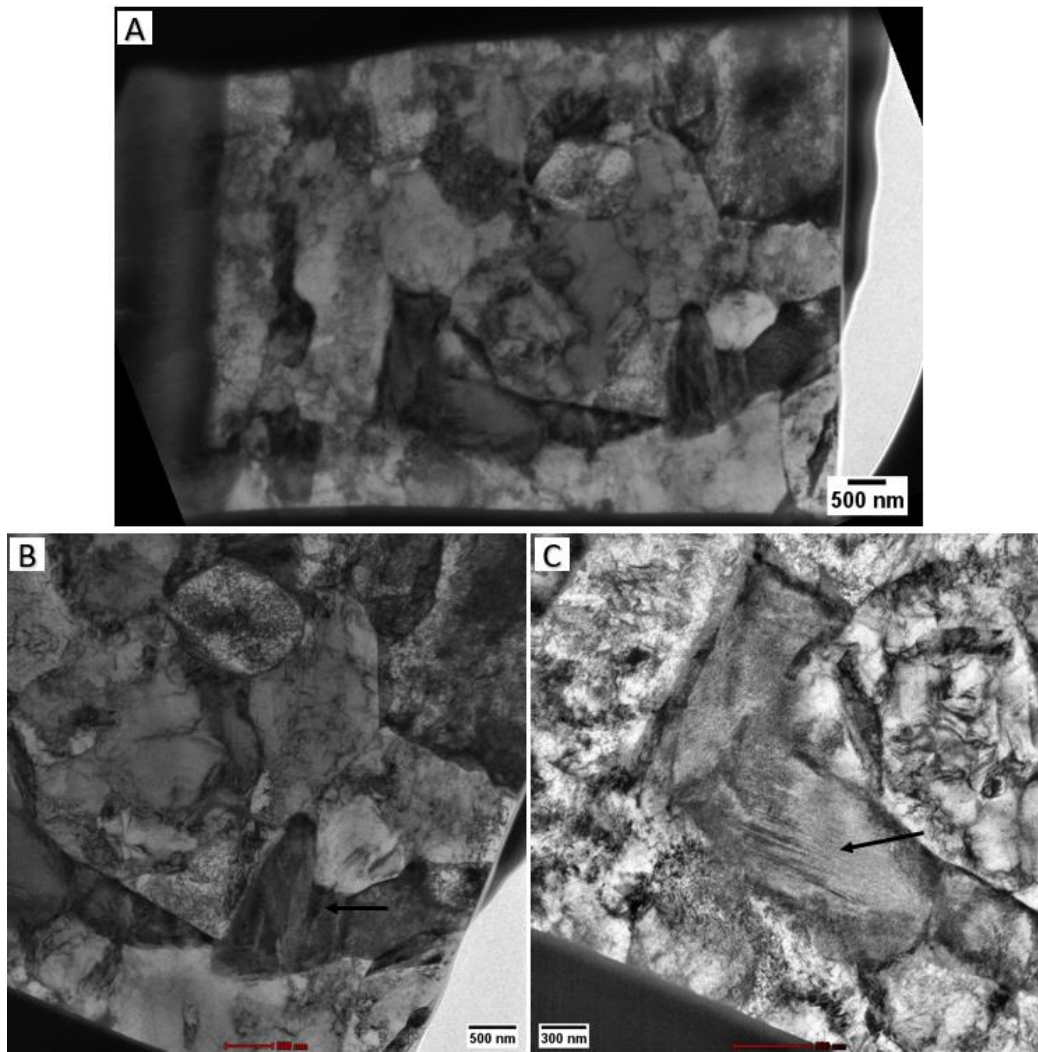


Figure 5.61 TEM images of CP1200. A – Low magnification image from the whole sample. B – region with plate like precipitates. C – region with transformed retained austenite.

5.10. Interface Quantification

5.10.1. CP1100

Interfaces of the samples were identified following the process presented in section 4.10.1. Figure 5.62 presents one example of bainite interface segmentation. Figure 5.63 shows an example of segmentation of all the interfaces following a RGB coloring system with red ferrite, green bainite and blue martensite. Table 5.15 presents a summary of the quantification of all the interfaces.

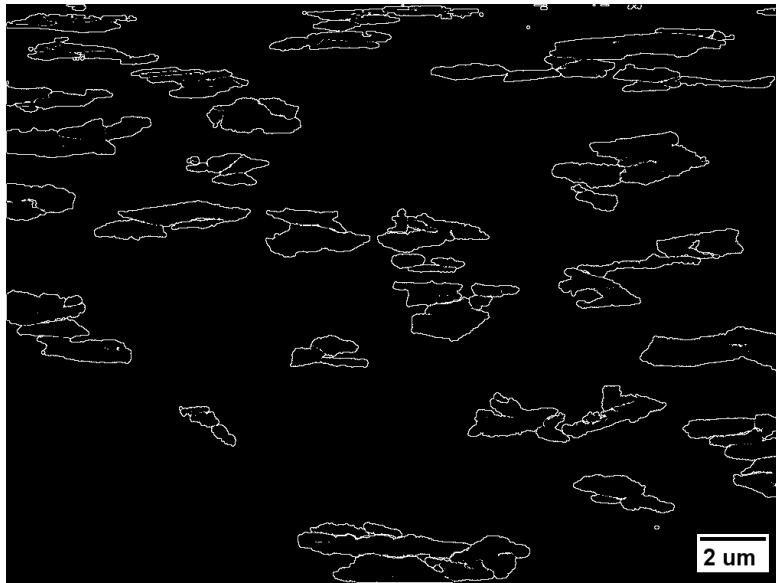


Figure 5.62 Interface of the bainite microconstituent of the CP1100 Steel.

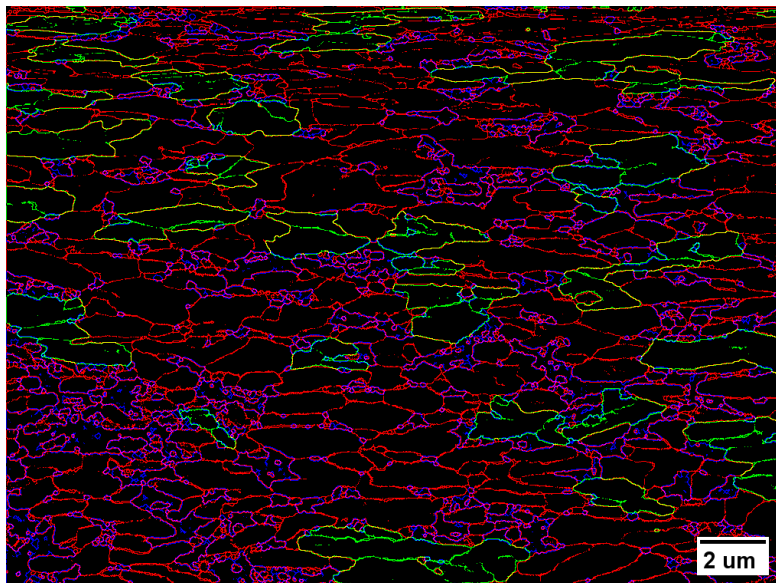


Figure 5.63 RGB color image of the CP1100 interface. Red ferrite, green bainite, blue martensite and their respective combinations.

Table 5.15 Interface quantification for the CP1100

Map	Interfaces Area %			Microconstituents Interface		
	Ferrite	Bainite	Martensite	F – M	B – F	B – M
CP1100 - Map 1	7.1	2.8	8.8	4.8	1.1	1.7
CP1100 - Map 2	8.3	4.2	7.6	4.6	1.9	1.6
CP1100 - Map 3	11.0	2.5	7.1	5.0	1.2	0.8
CP1100 - Map 4	11.0	6.0	7.9	4.7	2.2	1.7
CP1100 - Map 5	10.4	3.3	5.4	3.5	1.1	0.8
CP1100 - Map 6	11.2	2.7	5.9	4.0	1.3	0.6
Average area	9.8	3.6	7.1	4.4	1.5	1.2
Interface %	47.9%	17.4%	34.6%	62.5%	20.7%	16.9%

5.10.2. CP1200

Interface of the samples were identified following the process presented at section 4.10.1. Figure 5.64 presents one example of bainite interface segmentation. Figure 5.65 shows an example of segmentation of all the interfaces following a RGB coloring system with red ferrite, green bainite and blue martensite. Table 5.16 presents a summary of the quantification of all the interfaces.

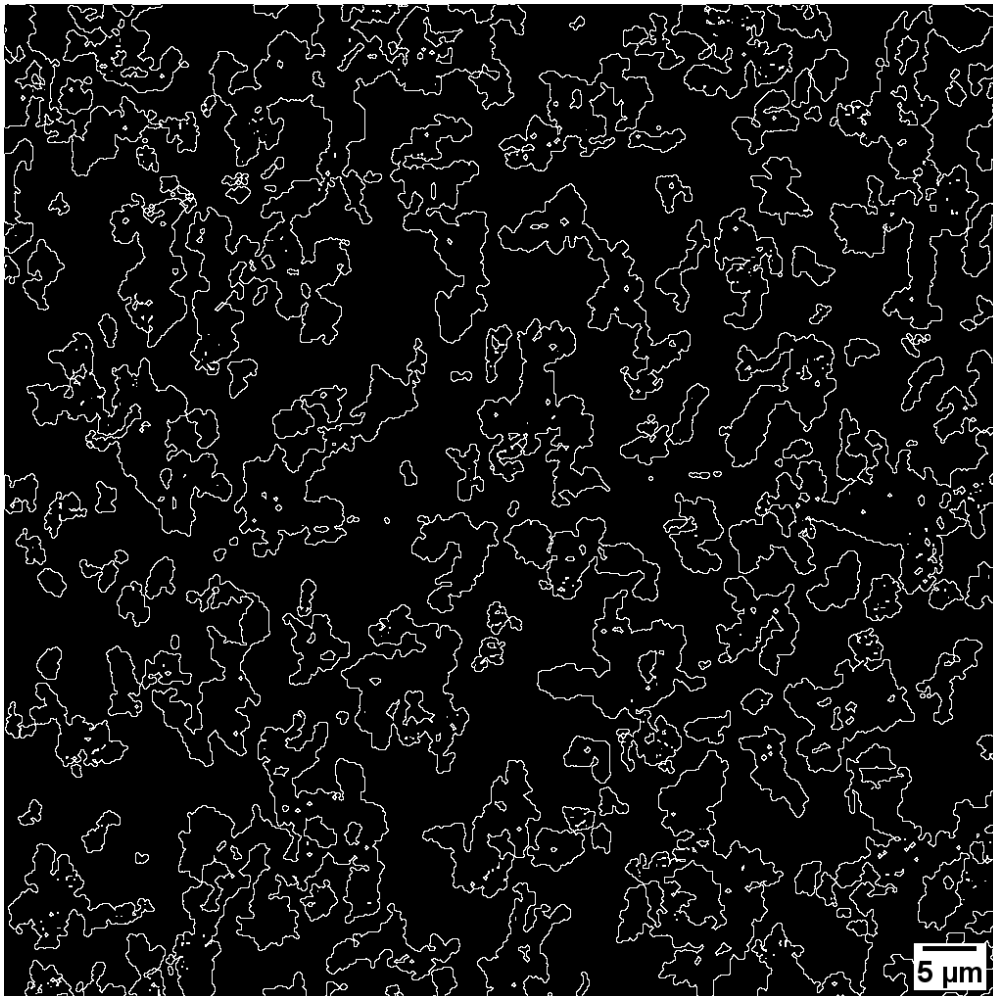


Figure 5.64 Interface of the bainite microconstituent of the CP1200 Steel.

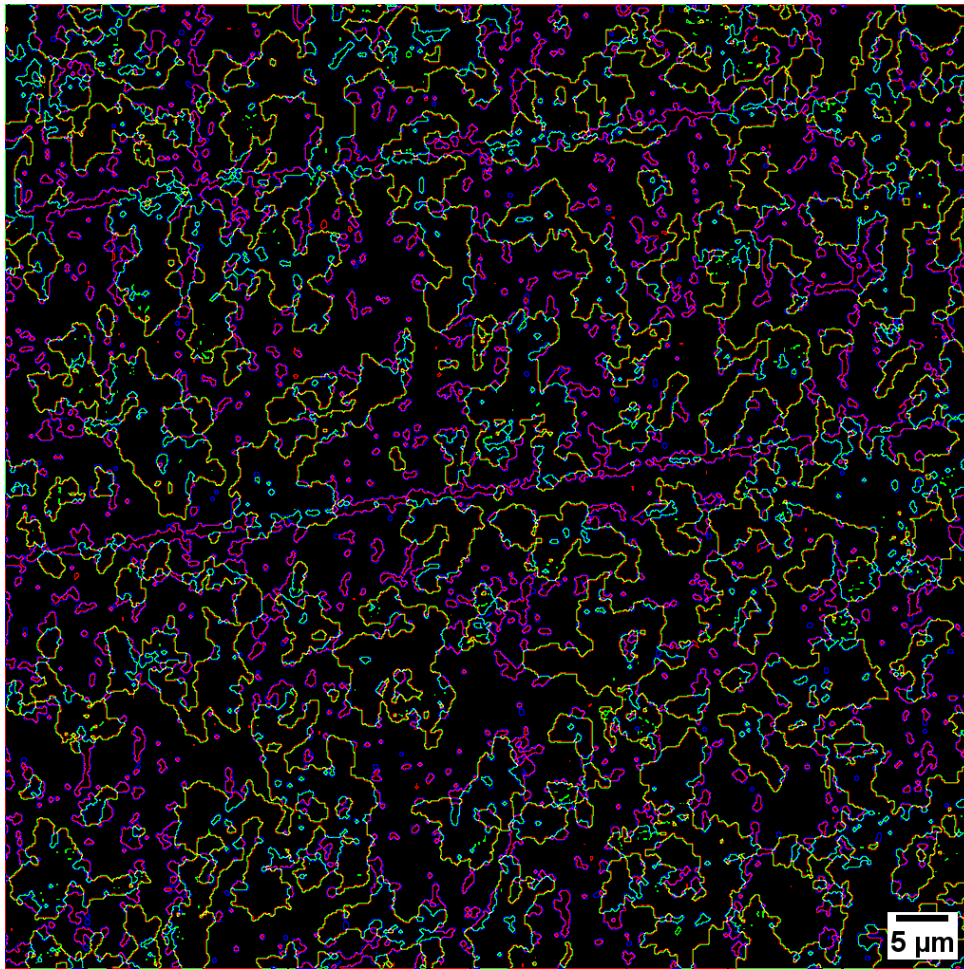


Figure 5.65 RGB color image of the CP1200 interface. Red ferrite, green bainite, blue martensite and their respective combinations.

Table 5.16 Interface quantification for the CP1200

Map	All interfaces %			Microconstituents Interface		
	Ferrite	Bainite	Ferrite	F - M	B - F	B - M
CP1200 - Map 1	7.7	5.4	7.4	4.4	2.2	2.6
CP1200 - Map 2	6.9	4.8	6.4	4.1	2.9	2.4
CP1200 - Map 3	8.0	5.9	9.6	5.5	2.8	4.4
CP1200 - Map 4	9.2	6.6	10.8	1.2	2.4	3.8
CP1200 - Map 5	8.1	6.7	7.4	4.1	4.2	3.0
CP1200 - Map 6	8.2	6.6	7.3	4.0	4.3	2.9
CP1200 - Map 7	11.5	8.2	11.7	5.8	3.3	3.9
Average area	8.5	6.3	8.7	4.1	3.1	3.3
Interface %	36.3%	26.9%	36.8%	39.2%	29.8%	31.0%

6 Discussion

The main goal of this thesis was the production of a CP1200 steel. The research approach was to improve an existing CP1100 steel towards the CP1200 by making changes in the heat treatment used in the last step of the complex-phase steel production. First, the continuous transformation diagram was obtained by means of dilatometry; then, based on the CCT data, a series of heat treatments were designed and conducted, combining theoretical concepts with empirical knowledge to attain the desired properties. A newly produced CP1200 was obtained and characterized. In this chapter, comparison will be made between the heat treatment and the final properties of both the CP1100 and CP1200 steels.

6.1. Mechanical Properties

The improvement of the mechanical properties from CP1100 to CP1200 was the initial objective of this thesis. The basic concept was that by reducing the amount of ferrite and increasing the bainite content the mechanical strength could be improved. The industrial CP1100 steel presented 1112MPa of UTS, 831 MPa of yield strength and 9% of total elongation. The newly produced CP1200 steel presented about 1270 MPa of UTS, 820 MPa of yield strength and 10.5% of total elongation, as can be seen in Table 6.1. An increase can be seen, not only in the ultimate tensile strength, but also on the total elongation.

Table 6.1 Comparison between CP1100 and CP1200 mechanical properties

Steel	YS(MPa)	UTS(MPa)	EI. (%)	HV10
CP1100	831	1112	9	323.8 ± 2.8
CP1200	820	1278	10.5	337 ± 2.3

Strictly speaking, the requirements for a steel to be considered a CP1200 is for it to present more than 1200 MPa of UTS with at least 8% of elongation and more than 800MPa of YS. Therefore, the initial goal of this thesis was satisfactorily fulfilled. The next step was to investigate how the microstructure affected the properties obtained. To accomplish this task, a detailed characterization the microstructure observed after the heat treatments of both steels was done.

6.2. Dilatometry

In Figure 6.1 the dilatometric results of the CP1100 and CP1200 are presented side by side. The first consideration is the intercritical temperature. The CP1200 was annealed at 825 °C, 25 degrees higher than the CP1100. This temperature was chosen with basis on the results of the CCT diagram, to increase the amount of intercritical austenite. This choice had three important effects: the austenite content of the CP1200 in that step is 89%, 13% more than the CP1100; the austenite of the CP1200 has lower carbon content and therefore is less stable; and the prior austenite grain size will be larger in the CP1200.

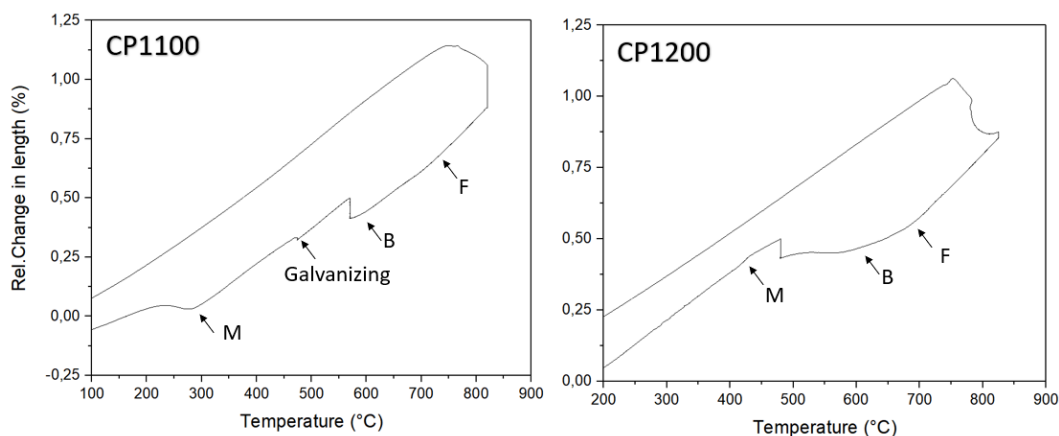


Figure 6.1 Side by side comparison of CP1100 and CP1200 dilatometric data

The behavior of both steels during the initial cooling is very similar, even with the slow start in the CP1200. Both have small deviation above 700 °C which indicates ferrite formation, either by nucleation of new grains

or growth of preexisting ones. The CP1200 presents between 700 °C and 600 °C a more intense ferrite transformation, that could be due to the smaller initial ferrite content. At about 600 °C bainite formation starts for both steels. Due to its lower holding temperature, the CP1200 seems to have a larger fraction of continuous cooled bainite, and less martensite. Although no distinction has been made between the continuous cooled and the isothermally nucleated bainite, the martensite content was found to be indeed smaller in the CP1200.

6.3. Microconstituents

In both the CP1100 and CP1200 a mixture of ferrite, bainite, martensite and retained austenite can be found. When looking at the microstructure by means of light optical microscopy, a reliable quantification of ferrite was attained. Besides that, the combined amount of bainite and martensite was also quantified. A direct comparison between the LOM results for both steels is shown in Table 6.2.

Table 6.2 LOM microstructural quantification for the CP1100 and CP1200 steels.

Steel	Ferrite %	Bainite/Martensite %	Retained Austenite%
CP1100	53.9 ± 3.7	45.3 ± 3.6	0.78 ± 0.25
CP1200	47.4 ± 1.97	50.34 ± 1.64	0.4 ± 0.18

Based only in the LOM quantification it would be reasonable to assume that the increase in about 5% of hard constituent (martensite/bainite) could justify the change in mechanical properties.

Later, with the use of EBSD, all four microconstituents were segmented and quantified. The CP1100 presented an average of 56% ferrite, 21% bainite, 21% martensite and 1.4% retained austenite. This has already been shown in Table 5.12. As for the CP1200, it presented 46% ferrite, 36% bainite, 17% martensite and 0.4% retained austenite, as shown in Table 5.14. Table 6.3 shows the EBSD results for both steels. An increase of the bainite content accompanied by a decrease in both ferrite and martensite was observed.

Table 6.3 Comparison between the CP1100 and CP1200 microstructural quantification

Steel	Ferrite %	Bainite %	Martensite %	RA %
CP1100	56.3 ± 4	21.1 ± 4.1	21.2 ± 1.5	1.4 ± 1
CP1200	46.7 ± 5	36.2 ± 1.5	16.7 ± 4.1	0.4 ± 0.2

The decrease in ferrite combined with the increase in bainite content is already possibly indicative for the increase in mechanical properties; but, other aspects need to be taken in account, such as the grain size and phase distribution. The difference in grain size, larger in the CP1200 than in CP1100, is evident when EBSD (Figure 6.2) maps and AFM (Figure 6.3) images for both steels are compared side by side. The measured average grain size by EBSD for each microconstituent can be seen in Table 6.4

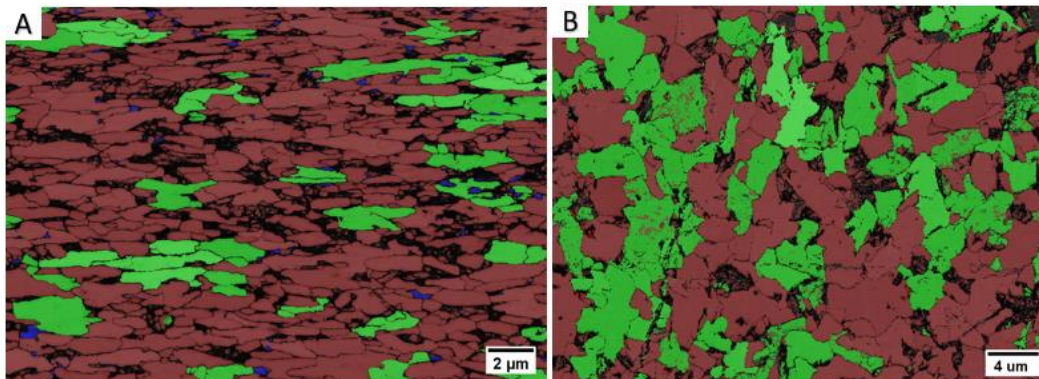


Figure 6.2 EBSD comparison between the CP1100 and CP1200 steel. A – CP1100. B – CP1200. Both images presents red ferrite, green bainite, blue retained austenite and black martensite.

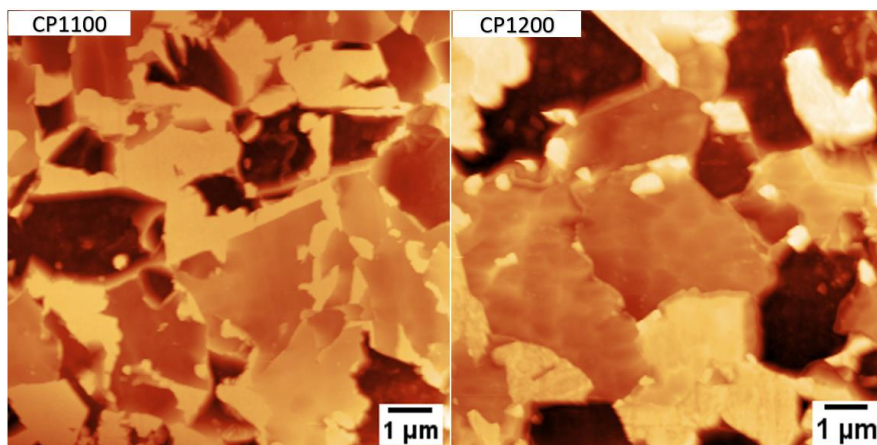


Figure 6.3 AFM comparison between the CP1100 and CP1200 microstructures

Table 6.4 Average grain size of each microconstituent obtained from EBSD maps.

Steel	Prior Austenite	Grain Size	Ferrite	Bainite	Martensite
CP1100	4.9 μm^2	1.3 μm^2	1.4 μm^2	1.7 μm^2	0.6 μm^2
CP1200	5.7 μm^2	2.9 μm^2	2.7 μm^2	4.2 μm^2	1 μm^2

One explanation for the difference in grain size can be derived from the prior austenite grain size. The CP1200 steel prior austenite grains were larger when compared to the CP1100 one. It should be noticed that the measured bainite grain size refers to an aggregate of bainitic ferrite and carbides.

Size and amount of the microconstituents is not the only consideration needed. The distribution of the microconstituents is also important. One way to analyze this distribution is to quantify the microconstituent interfaces. The importance of the kind of interface on the void nucleation was already discussed in the literature [26], [33], [71], [73], [123]. Table 6.5 shows the percentage of ferrite-martensite, bainite-ferrite and bainite-martensite interfaces for both steels.

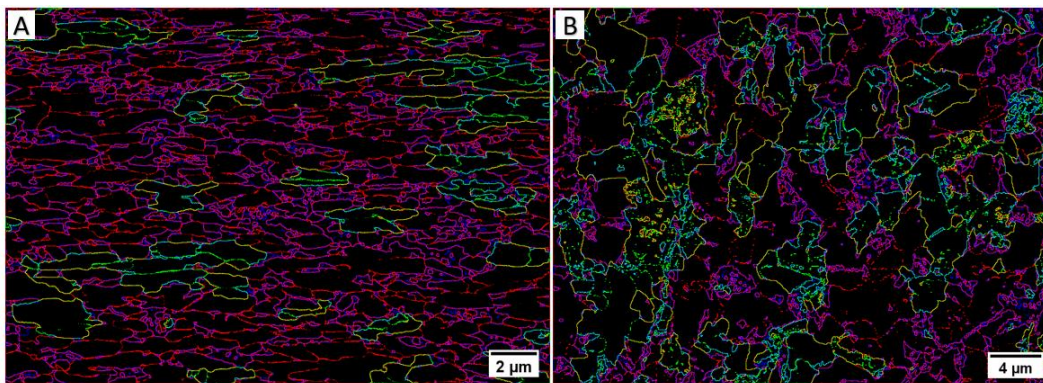


Figure 6.4 Side by side comparison of the segmented interfaces. A – CP1100. B – CP1200.

Table 6.5 Comparison between the interface quantification of CP1100 and CP1200

Interface	CP1100	CP1200
Ferrite - Martensite	62.5%	39.2%
Bainite - Ferrite	20.7%	29.8%
Bainite - Martensite	16.9%	31%

Void nucleation experiments remain a topic for future research efforts. The simple average decrease in ferrite-martensite interfaces of more than

20% is a good indication that the void nucleation may have been minimized on the new CP1200 steel. This, together with the increase in bainite content, can explain the increase in mechanical properties, despite the presence of larger grains.

Considering this, the increase in the mechanical properties of the CP1200 when compared to the CP1100 can be attributed to the increase in bainite content and the decrease in ferrite/martensite interfaces. Additional testing should be conducted in order to confirm these findings.

7 Conclusion

Commercial demand for Complex-Phase steel with 1200 MPa of tension strength, 800 MPa of yield Strength, and at least 8% of total elongation was the main goal of this thesis. Based on all the presented results, some conclusions can be summarized:

- Through dilatometry, the CCT diagram for this steel composition was developed. Due to its alloying elements, there is a shift in the ferrite formation curve, considering this, some heat treatments that avoid the ferrite formation, such as the Complex-Phase heat treatment, can be designed.
- The formation of martensitic bands was observed at holding temperatures of 500 °C. Lower temperatures of 450 °C did not presented the same undesirable aspect, but low hardness values were observed. Therefore, an intermediary holding temperature was chosen as the best choice for the heat treatments.
- The CP1100 steel microstructure was quantified, presenting 56% ferrite, 21% bainite, 21% martensite, and 1.4% retained austenite. The microconstituents interface distribution was measured, presenting 62.5% ferrite/martensite interfaces, 20.7% bainite/ferrite interfaces, and 16.9% bainite/martensite interfaces.
- Taking the microstructure of the CP1100 into account, a new heat treatment was designed, aiming to reduce the ferrite content and increase the bainite one. Higher annealing and lower holding temperatures were chosen for this heat treatment.
- The new CP1200 mechanical properties were measured, presenting up to 1270 MPa of ultimate tensile strength, 820 MPa of yield strength, and 10.5% of total elongation. The bending test also showed satisfactory results for the bending at 90°, and only above

105° signals of crack formation were seen. The hole expansion test presented a λ value of 120%.

- The microstructural quantification for the CP1200 presented 46% ferrite, 36% bainite, 17% martensite, and 0.4% retained austenite. The microconstituents interface distribution was measured, presenting of 39.2% ferrite/martensite interfaces, 29.8% of bainite/ferrite interfaces, and 31% of bainite/martensite interfaces.
- The increase in the mechanical properties between the CP1100 and CP1200 was attributed to the increase in the bainite content and the decrease in ferrite/martensite interfaces, considering that ferrite/martensite interfaces are more prone to void nucleation, but further work is needed to confirm this hypothesis.

8 Suggestions for Future Work

Due to the COVID19 pandemic, some of the planned treatments and tests could not be performed in time. That happened either due to the early return to Brazil by the student or by several months of closed laboratories. A list of suggestions for future work is presented below.

8.1. Gleeble

A Gleeble could be used for pilot scale tests. Initially a Gleeble 3500 was planned to be used to for thermal treatments and tensile testing. These tests would be an interesting bridge between the dilatometer tests and the industrial scale production.

8.2. Salt Pots

Similar to the Gleeble, salt pots are an alternative for treatments at the pilot scale. They would help to link the dilatometry results with the industrial scale. Colorado School of Mines has 3 salt pots baths for treatments that can be used to do these experiments.

8.3. X-Ray Tomography

X-ray tomography has been used in the literature to observe void nucleation in both dual- and complex-phase steels [124], [125]. The DEQM possess an X-ray microtomograph XRadia 510 VERSA from Zeiss. The sample conditions for microtomography have already been discussed, but Gleeble treatments need to be conducted prior to the analysis.

8.4. Mössbauer Effect

Mössbauer spectroscopy is a good alternative for a precise quantification of retained austenite and precipitates. It has been used in the literature [95], [126] for this application. The CBPF owns a Mössbauer spectrometer and that can be used after the COVID-19 pandemic is under control.

8.5. Modelling of Phase Transformation

There are modeling methods to predict the kinetic paths, and the final microstructures, for the different processing routes and temperatures that can be used. An example is the Rios method, proposed in 2005. This method uses data from transformation curves in continuous cooling (CCT) conditions to predict isothermal transformations results. According to the author, continuous heating data can also be used for the same purpose [127]. Application of modelling methods over the CCT diagram data can be a path to better control the final microstructure and, thereby the final mechanical properties.

9 Bibliography

- [1] D. Bhattacharya, “Microalloyed Steels for the Automotive Industry,” *Tecnol. em Metal. Mater. e Mineração*, vol. 11, no. 4, pp. 371–383, 2014.
- [2] M. Singh, “Application of Steel in Automotive Industry,” 2016.
- [3] R. Kuziak, R. Kawalla, and S. Waengler, “Advanced high strength steels for automotive industry,” *Arch. Civ. Mech. Eng.*, vol. 8, no. 2, pp. 103–117, 2008.
- [4] D. V. Edmonds, K. He, F. C. Rizzo, B. C. De Cooman, D. K. Matlock, and J. G. Speer, “Quenching and partitioning martensite-A novel steel heat treatment,” *Mater. Sci. Eng. A*, vol. 438–440, no. SPEC. ISS., pp. 25–34, 2006.
- [5] M. De Meyer, J. Mahieu, and B. C. De Cooman, “Empirical microstructure prediction method for combined intercritical annealing and bainitic transformation of TRIP steel,” *Mater. Sci. Technol.*, vol. 18, no. 10, pp. 1121–1132, 2003.
- [6] J. Sojka, P. Váňová, V. Vodárek, and M. Sozańska, “Diffusion of Hydrogen in the TRIP 800 Steel,” *Procedia Mater. Sci.*, vol. 12, pp. 66–71, 2016.
- [7] J. G. Speer, E. De Moor, K. O. Findley, D. K. Matlock, B. C. De Cooman, and D. V. Edmonds, “Analysis of microstructure evolution in quenching and partitioning automotive sheet steel,” *Metall. Mater. Trans. A Phys. Metall. Mater. Sci.*, vol. 42, no. 12, pp. 3591–3601, 2011.
- [8] H. Aydin, E. Essadiqi, I. H. Jung, and S. Yue, “Development of 3rd generation AHSS with medium Mn content alloying compositions,” *Mater. Sci. Eng. A*, vol. 564, pp. 501–508, 2013.
- [9] W. A. Steel, “Chevrolet Cruze 2016-17 HSS Global Platform,” 2021. [Online]. Available: <https://www.worldautosteel.org/why-steel/steel-muscle-in-new-vehicles/2016-chevy-cruze-hss-global-platform/>. [Accessed: 31-Aug-2021].
- [10] H. K. D. H. Bhadeshia and J. W. Christian, “Bainite in steels,” *Metall. Trans. A*, vol. 21, no. 3, pp. 767–797, 1990.

- [11] G. Krauss, “Bainite—An Intermediate Temperature Transformation Product of Austenite,” in *Steels-Processing, Structure, and Performance, Second Edition*, 2015, pp. 99–112.
- [12] S. Zajac, V. Schwinn, and K. H. Tacke, “Characterisation and Quantification of Complex Bainitic Microstructures in High and Ultra-High Strength Linepipe Steels,” *Mater. Sci. Forum*, vol. 500–501, no. November, pp. 387–394, 2005.
- [13] F. G. Caballero, M. K. Miller, C. Garcia-Mateo, C. Capdevila, and C. Garcia de Andrés, “Phase transformation theory: A powerful tool for the design of advanced steels,” *Jom*, vol. 60, no. 12, pp. 16–21, 2008.
- [14] B. L. Bramfitt and J. G. Speer, “A perspective on the morphology of bainite,” *Metall. Trans. A*, vol. 21, no. 3, pp. 817–829, 1990.
- [15] V. Biss and R. L. Cryderman, “Martensite and retained austenite in hot-rolled, low-carbon bainitic steels,” *Metall. Mater. Trans. B*, vol. 2, no. 8, pp. 2267–2276, 1971.
- [16] G. J. P. Buchi, J. H. R. Page, and M. P. Sidey, “No Title,” *JISI*, pp. 291–298, 1965.
- [17] Y. Tomita and K. Okabayashi, “Modified heat treatment for lower temperature improvement of the mechanical properties of two ultrahigh strength low alloy steels,” *Metall. Trans. A*, vol. 16, no. 1, pp. 83–91, 1985.
- [18] E. De Moor and J. G. Speer, *Bainitic and quenching and partitioning steels*. Elsevier Ltd, 2017.
- [19] R. L. Bodnar, J. R. Michael, S. S. Hansen, and R. I. Jaffee, “Progress in the design of an improved high-temperature 1 percent CrMoV rotor steel,” *J. Eng. Mater. Technol. Trans. ASME*, vol. 112, no. 1, pp. 99–115, 1990.
- [20] A. Gorni, *Heat treating*, 23rd ed., vol. 60, no. 4. 2019.
- [21] T. Kunitake and Y. Okada, “The estimation of bainite transformation temperatures in steels by the empirical formulas,” *Tetsu-To-Hagane/Journal Iron Steel Inst. Japan*, vol. 84, no. 2, pp. 53–57, 1998.
- [22] Y. K. Lee, “Empirical formula of isothermal bainite start temperature of steels,” *J. Mater. Sci. Lett.*, vol. 21, no. 16, pp. 1253–1255, 2002.
- [23] M. Victor Li, D. V. Niebuhr, L. L. Meekisho, and D. G. Atteridge, “A computational model for the prediction of steel hardenability,” *Metall. Mater. Trans. B Process Metall. Mater. Process. Sci.*, vol. 29, no. 3, pp. 661–

- 672, 1998.
- [24] M. Suehiro, T. Senuma, H. Yada, Y. Matsumura, and T. Ariyoshi, “Kinetic Model for Phase Transformations of Low Carbon Steels During Continuous Cooling.,” *Tetsu-To-Hagane/Journal Iron Steel Inst. Japan*, vol. 73, no. 8, pp. 1026–1033, 1987.
- [25] C. C. Tasan *et al.*, “An Overview of Dual-Phase Steels: Advances in Microstructure-Oriented Processing and Micromechanically Guided Design,” *Annu. Rev. Mater. Res.*, vol. 45, pp. 391–431, 2015.
- [26] N. Pathak, C. Butcher, M. J. Worswick, E. Bellhouse, and J. Gao, “Damage evolution in complex-phase and dual-phase steels during edge stretching,” *Materials (Basel)*, vol. 10, no. 4, pp. 1–29, 2017.
- [27] M. Sarwar, R. Priestner, M. Materials, and S. Centre, “Influence of ferrite-martensite microstructural morphology on tensile properties of dual-phase steel,” vol. 31, pp. 2091–2095, 1996.
- [28] C. C. Tasan, J. P. M. Hoefnagels, M. Diehl, D. Yan, F. Roters, and D. Raabe, “Strain localization and damage in dual phase steels investigated by coupled in-situ deformation experiments and crystal plasticity simulations,” *Int. J. Plast.*, vol. 63, pp. 198–210, 2014.
- [29] N. Yoshinaga, H. Kawata, and K. Hikida, “Recent topics on development of automotive high-strength sheet steels,” *Lecture Notes in Mechanical Engineering*, vol. PartF2, pp. 21–26, 2018.
- [30] Y. Mazaheri, A. Kermanpur, and A. Najafizadeh, “Strengthening Mechanisms of Ultrafine Grained Dual Phase Steels Developed by New Thermomechanical Processing,” *ISIJ Int.*, vol. 55, no. 1, pp. 218–226, 2015.
- [31] N. Fonstein, *Advanced high strength sheet steels: Physical metallurgy, design, processing, and properties*. 2015.
- [32] A. Karellova, C. Kremaszky, E. Werner, P. Tsipouridis, T. Hebesberger, and A. Pichler, “Hole Expansion of Dual-phase and Complex-phase AHS Steels - Effect of Edge Conditions,” *Steel Res. Int.*, vol. 80, pp. 71–77, 2009.
- [33] P. Martin, K. Unruh, J. Chottin, and E. Hug, “Damage mechanisms in multiphased steels with a bainitic matrix under various mechanical loading paths,” *Procedia Manuf.*, vol. 15, pp. 1557–1564, 2018.
- [34] C. C. Tasan, J. P. M. Hoefnagels, and M. G. D. Geers, “Microstructural banding effects clarified through micrographic digital image correlation,”

- Scr. Mater.*, vol. 62, no. 11, pp. 835–838, 2010.
- [35] E. Billur, *Hot formed steels*. Elsevier Ltd, 2016.
- [36] J. N. Hall and J. R. Fekete, *Steels for auto bodies: A general overview*. Elsevier Ltd, 2017.
- [37] T. B. Hilditch, T. de Souza, and P. D. Hodgson, *Properties and automotive applications of advanced high-strength steels (AHSS)*. Elsevier Ltd, 2015.
- [38] C. D. Horvath, *Advanced steels for lightweight automotive structures*. LTD, 2021.
- [39] P. K. Mallick, “Advanced materials for automotive applications: an overview,” *Adv. Mater. Automot. Eng.*, pp. 5–27, 2012.
- [40] M. Shome and M. Tumuluru, *Introduction to welding and joining of advanced high-strength steels (AHSS)*. Elsevier Ltd, 2015.
- [41] K. Sugimoto and M. Mukherjee, *TRIP aided and complex phase steels*. Elsevier Ltd, 2016.
- [42] M. C. Theyssier, *Manufacturing of advanced high-strength steels (AHSS)*. Elsevier Ltd, 2015.
- [43] X. Wu, “Advanced high-strength steel tailor welded blanks (AHSS-TWBs),” in *Tailor Welded Blanks for Advanced Manufacturing*, 2011, pp. 118–163.
- [44] A. L. V. da Costa e Silva and P. R. Mei, *Aços e Ligas Especiais*, 2nd ed. Villares Metals, 2006.
- [45] B. Dutta, E. Valdes, and C. M. Sellars, “Mechanism and kinetics of strain induced precipitation of Nb(C, N) in austenite,” *Acta Metall.*, vol. 40, no. 4, pp. 653–662, 1992.
- [46] G. Han, Z. J. Xie, L. Xiong, C. J. Shang, and R. D. K. Misra, “Evolution of nano-size precipitation and mechanical properties in a high strength-ductility low alloy steel through intercritical treatment Materials Science & Engineering A Evolution of nano-size precipitation and mechanical properties in a high strength,” *Mater. Sci. Eng. A*, vol. 705, no. August, pp. 89–97, 2017.
- [47] W. B. Lee, S. G. Hong, C. G. Park, K. H. Kim, and S. H. Park, “Influence of Mo on precipitation hardening in hot rolled HSLA steels containing Nb,” vol. 43, pp. 319–324, 2000.
- [48] R. Zubialde and B. López, “Analysis of the influence of rolling conditions and Nb microalloying on the final ferrite microstructure in steels processed

- by TSDR route,” pp. 171–180.
- [49] J. G. Speer, F. C. R. Assunção, D. K. Matlock, and D. V. Edmonds, “The ‘quenching and partitioning’ process: background and recent progress,” *Mater. Res.*, vol. 8, no. 4, pp. 417–423, 2005.
- [50] H. L. Yi *et al.*, “A novel design: Partitioning achieved by quenching and tempering (Q-T & P) in an aluminium-added low-density steel,” *Scr. Mater.*, vol. 68, no. 6, pp. 370–374, 2013.
- [51] T. Réti, “Residual Stresses in Carburized , Carbonitrided , and Case-Hardened,” in *Handbook of Residual Stress and Deformation of Steel*, G. Totten, M. Howes, and T. Inoue, Eds. 2002, pp. 189–208.
- [52] W. Bleck and K. Phiu-on, “Effects of Microalloying in Multi Phase Steels for Car Body Manufacture,” *Microstruct. Texture Steels*, pp. 145–163, 2009.
- [53] H. Mohrbacher, *Synergies of niobium and boron microalloying in molybdenum based bainitic and martensitic steels*, vol. 1. 2011.
- [54] J. F. Da Silva Filho *et al.*, “Effect of Cr additions on ferrite recrystallization and austenite formation in dual-phase steels heat treated in the intercritical temperature range,” *Mater. Res.*, vol. 19, no. 1, pp. 258–266, 2016.
- [55] Y. Sakuma, O. Matsumura, and H. Takechi, “Mechanical properties and retained austenite in intercritically heat-treated bainite-transformed steel and their variation with Si and Mn additions,” *Metall. Trans. A*, vol. 22, no. 2, pp. 489–498, 1991.
- [56] O. Grässel, L. Krüger, G. Frommeyer, and L. W. Meyer, “High strength Fe-Mn-(Al, Si) TRIP/TWIP steels development - properties - application,” *Int. J. Plast.*, vol. 16, no. 10, pp. 1391–1409, 2000.
- [57] R. C. Giacomini and B. A. Webler, “Effect of Silicon on AHSS As-Cast Microstructure Development and Properties,” *ISIJ Int.*, vol. 59, no. 5, pp. 858–864, 2019.
- [58] K. Cho, C. I. Garcia, H. Shu, T. R. Chen, and A. J. Deardo, “Development of the 590 - 780 - 980 Nb-bearing dual-phase steels for production on continuous galvanizing lines,” *2007 Int. Conf. Microalloyed Steels Process. Microstruct. Prop. Perform. Proc.*, pp. 313–323, 2007.
- [59] K. I. Sugimoto, T. Muramatsu, S. I. Hashimoto, and Y. Mukai, “Formability of Nb bearing ultra high-strength TRIP-aided sheet steels,” *J. Mater. Process. Technol.*, vol. 177, no. 1–3, pp. 390–395, 2006.

- [60] G. Y. Perez Medina, E. Hurtado Delgado, A. F. Miranda Perez, and H. Lopez Ferreira, “Phases quantification in DP600 steel welded by GTAW process using SEM and atomic force microscopy,” *Mater. Res.*, vol. 20, no. 5, pp. 1–5, 2017.
- [61] P. Tsipouridis, E. Werner, C. Kremaszky, and E. Tragl, “Formability of high strength DP steels,” *Steel Res. Int.*, vol. 77, no. 9, pp. 654–667, 2006.
- [62] I. Gutierrez *et al.*, *Mechanical property models for high-strength complex microstructures*, no. March. 2010.
- [63] N. Pottore, N. Fonstein, I. Gupta, and D. Bhattacharya, “A Family of 980MPa Tensile Strength Advanced High Strength Steels with Various Mechanical Property Attributes,” *AHSS Proc*, no. February, pp. 119–129, 2004.
- [64] W. Woo, V. T. Em, E. Y. Kim, S. H. Han, Y. S. Han, and S. H. Choi, “Stress-strain relationship between ferrite and martensite in a dual-phase steel studied by in situ neutron diffraction and crystal plasticity theories,” *Acta Mater.*, 2012.
- [65] S. C. Simões, “Caracterização experimental e não-destrutiva de aços de alta resistência , DP1000 e DP1200,” 2017.
- [66] E. Cadoni, N. K. Singh, D. Forni, M. K. Singha, and N. K. Gupta, “Strain rate effects on the mechanical behavior of two Dual Phase steels in tension,” *Eur. Phys. J. Spec. Top.*, vol. 225, no. 2, pp. 409–421, 2016.
- [67] T. Jia, M. Militzer, and Z. Y. Liu, “General Method of Phase Transformation Modeling in Advanced High Strength Steels,” *ISIJ Int.*, vol. 50, no. 4, pp. 583–590, 2010.
- [68] S. Salari, A. Saeed-Akbari, M. Naderi, and W. Bleck, “Martensitic transformation behavior of b-bearing steel during isothermal deformation,” *Steel Res. Int.*, vol. 83, no. 8, pp. 733–742, 2012.
- [69] F. Hairer, A. Karellová, C. Kremaszky, E. Werner, T. Pichler, and A. Hebesberger, “Etching techniques for the microstructural characterization of complex phase steels by light microscopy,” *Int. Dr. Semin.*, pp. 50–54, 2008.
- [70] F. Hairer, C. Kremaszky, and U. München, “Effects of Heat Treatment on Microstructure and Mechanical Properties of Bainitic Single- and Complex-Phase Steel,” *Mater. Sci. Technol.*, no. June 2018, pp. 1391–1401, 2009.
- [71] N. K. Singh, E. Cadoni, M. K. Singha, and N. K. Gupta, “Quasi-static and

- dynamic tensile behavior of CP800 steel,” *Mech. Adv. Mater. Struct.*, vol. 21, no. 7, pp. 531–537, 2014.
- [72] N. K. Singh, E. Cadoni, M. K. Singha, and N. K. Gupta, “Dynamic tensile behavior of multi phase high yield strength steel,” *Mater. Des.*, vol. 32, no. 10, pp. 5091–5098, 2011.
- [73] X. Li, A. Ramazani, U. Prahl, and W. Bleck, “Quantification of complex-phase steel microstructure by using combined EBSD and EPMA measurements,” *Mater. Charact.*, vol. 142, no. May, pp. 179–186, 2018.
- [74] A. Grajcar, W. Zalecki, P. Skrzypczyk, A. Kilarski, A. Kowalski, and S. Kołodziej, “Dilatometric study of phase transformations in advanced high-strength bainitic steel,” *J. Therm. Anal. Calorim.*, vol. 118, no. 2, pp. 739–748, 2014.
- [75] R. f. Speyer, *Thermal Analysis of Materials*. 1994.
- [76] C. Mesplont, S. Vandeputte, and B. C. De Cooman, “Dilatometric study of the effect of soluble boron on the continuous and isothermal austenite decomposition in 0.15C-1.6Mn steel,” *Zeitschrift fuer Met. Res. Adv. Tech.*, vol. 93, no. 11, pp. 1108–1118, 2002.
- [77] J. Z. Zhao, C. Mesplont, and C. De Cooman, “Calculation of the phase transformation kinetics from a dilatation curve,” *J. Mater. Process. Technol.*, vol. 129, no. 1–3, pp. 345–348, 2002.
- [78] J. R. Yang and H. K. D. H. Bhadeshia, “Continuous heating transformation of bainite to austenite,” *Mater. Sci. Eng. A*, vol. 131, no. 1, pp. 99–113, 1991.
- [79] H. S. Yang and H. K. D. H. Bhadeshia, “Uncertainties in dilatometric determination of martensite start temperature,” *Mater. Sci. Technol.*, vol. 23, no. 5, pp. 556–560, 2007.
- [80] A. J. Schwartz, M. Kumar, and B. L. Adams, *Electron Backscatter Doffraction in Materials Science*, vol. 2. 2009.
- [81] L. Ryde, “Application of EBSD to analysis of microstructures in commercial steels,” *Mater. Sci. Technol.*, vol. 22, no. 11, pp. 1297–1306, 2006.
- [82] J. Y. Kang *et al.*, “Phase analysis of steels by grain-averaged EBSD functions,” *ISIJ Int.*, vol. 51, no. 1, pp. 130–136, 2011.
- [83] Y. Peng, M. P. Oxley, A. R. Lupini, M. F. Chisholm, and S. J. Pennycook, “Icroscopy Icroanalysis,” pp. 36–47, 2008.
- [84] P. T. Pinard, A. Schwedt, A. Ramazani, U. Prahl, and S. Richter,

- “Characterization of dual-phase steel microstructure by combined submicrometer EBSD and EPMA carbon measurements,” *Microsc. Microanal.*, vol. 19, no. 4, pp. 996–1006, 2013.
- [85] N. M. Lopez Granados and A. Salinas Rodriguez, “EBSD Investigation on Effect of Cooling Rate on Microstructure and Transformation Textures of High Strength Hot-rolled Steel Plates,” *J. Iron Steel Res. Int.*, vol. 23, no. 3, pp. 261–269, 2016.
- [86] S. Nishikawa and S. Kikuchi, “Diffraction of Cathode Rays by Calcite,” *Nature*, vol. 122, no. 3080, p. 726, 1928.
- [87] Oxford Instruments, “AZtec ® Reclassify Phase: Discriminating phases in steels,” p. 4, 2016.
- [88] S. Preparation and E. Conditions, “Identifikation of Martenzite in Steel by EBSD,” *Oxford instruments*, pp. 1–3, 2013.
- [89] A. Note, “High Resolution EBSD Mapping of Martensitic Steel,” pp. 2–4.
- [90] O. Nstruments, “AZtec Grain Analysis,” vol. 1, pp. 9–11.
- [91] C. I. Garcia, M. Hua, K. Cho, and A. J. DeArdo, “New method of characterizing and quantifying complex microstructures in steels,” in *Materials and Manufacturing Processes*, 2010, vol. 25, no. 1–3, pp. 33–40.
- [92] H. Zhao, B. P. Wynne, and E. J. Palmiere, “A phase quantification method based on EBSD data for a continuously cooled microalloyed steel,” *Mater. Charact.*, vol. 123, pp. 339–348, 2017.
- [93] J. Kadkhodapour, S. Schmauder, D. Raabe, S. Ziaei-Rad, U. Weber, and M. Calcagnotto, “Experimental and numerical study on geometrically necessary dislocations and non-homogeneous mechanical properties of the ferrite phase in dual phase steels,” *Acta Mater.*, vol. 59, no. 11, pp. 4387–4394, 2011.
- [94] G. M. McClelland, R. Erlandsson, and S. Chiang, “Atomic Force Microscopy: General Principles and a New Implementation,” *Rev. Prog. Quant. Nondestruct. Eval.*, pp. 1307–1314, 1987.
- [95] T. Ros-Yáñez, Y. Houbaert, and A. Mertens, “Characterization of TRIP-assisted multiphase steel surface topography by atomic force microscopy,” *Mater. Charact.*, vol. 47, no. 2, pp. 93–104, 2001.
- [96] B. Voigtlande, *Scanning probe microscopy: Atomic Force Microscopy and Scanning Tunneling Microscopy*. 2019.

- [97] P. Eaton and P. West, *Atomic Force Microscopy*, vol. 9780199570. 2010.
- [98] N. C. Santos and F. A. Carvalho, *Atomic Force Microscopy: Methods and Protocols*. 1886.
- [99] G. Haugstad, *Atomic force microscopy: Understanding Basic Modes and Advanced Applications*. Wiley, 2012.
- [100] T. F. A. Santos, E. A. Torres, J. M. C. Vilela, M. S. Andrade, and A. B. Cota, “Microstructural characterization of low carbon steels by atomic force microscopy,” *Rev. Latinoam. Metal. y Mater.*, vol. 35, no. 1, pp. 118–133, 2014.
- [101] N. Sathirachinda, R. Gubner, J. Pan, and U. Kivisäkk, “Characterization of phases in duplex stainless steel by magnetic force microscopy/scanning Kelvin probe force microscopy,” *Electrochem. Solid-State Lett.*, vol. 11, no. 7, pp. 41–45, 2008.
- [102] W. S. McCulloch and W. Pitts, “A logical calculus nervous activity,” *Bull. Math. Biol.*, vol. 52, no. 1, pp. 99–115, 1990.
- [103] F. Rosenblatt, “The Perceptron - A Perceiving and Recognizing Automaton,” *Report 85, Cornell Aeronautical Laboratory*. pp. 460–1, 1957.
- [104] M. Egmont-Petersen, D. De Ridder, and H. Handels, “Image processing with neural networks- A review,” *Pattern Recognit.*, vol. 35, no. 10, pp. 2279–2301, 2002.
- [105] Andrew Glassner, “Deep Learning, Vol. 1: From Basics to Practice; Vol. 2: From Basics to Practice,” vol. 2, p. 914, 2018.
- [106] J. Zupan, “Introduction to artificial neural network (ANN) methods: what they are and how to use them,” *Acta Chim. Slov.*, vol. 41, no. September, pp. 327–327, 1994.
- [107] S. Skansi, *Guide to Deep Learning Basics*. 2020.
- [108] J. Zupan, “Neural networks in chemistry,” no. March, pp. 469–470, 2008.
- [109] A. Glassner, “Deep Learning: From Basics to Practice Volume 2,” vol. 2, p. 914, 2018.
- [110] F. T. Tolomelli, “Private Communication,” 2019.
- [111] M. M. Nowell, R. A. Witt, and B. True, “EBSD Sample Preparation: Techniques, Tips, and Tricks,” *Microsc. Microanal.*, vol. 11, no. S02, pp. 504–505, 2005.
- [112] L. A. Pinto, D. Pérez Escobar, O. S. H. Santos, N. I. A. Lopes, J. R. G.

- Carneiro, and R. Ribeiro-Andrade, “Influence of surface preparation method on retained austenite quantification,” *Mater. Today Commun.*, vol. 24, no. May, 2020.
- [113] S. I. Wright, “Random thoughts on non-random misorientation distributions,” *Mater. Sci. Technol.*, vol. 22, no. 11, pp. 1287–1296, 2006.
- [114] L. N. Brewer and J. R. Michael, “Risks of ‘Cleaning’ Electron Backscatter Diffraction Data,” *Microsc. Today*, vol. 18, no. 2, pp. 10–15, 2010.
- [115] A. Laureys, T. Depover, R. Petrov, and K. Verbeken, “Microstructural characterization of hydrogen induced cracking in TRIP-assisted steel by EBSD,” *Mater. Charact.*, vol. 112, pp. 169–179, 2016.
- [116] R. Petrov, L. Kestens, A. Wasilkowska, and Y. Houbaert, “Microstructure and texture of a lightly deformed TRIP-assisted steel characterized by means of the EBSD technique,” *Mater. Sci. Eng. A*, vol. 447, no. 1–2, pp. 285–297, 2007.
- [117] Oxford Instruments, “Grain size characterisation of a steel sample using the AZtec HKL EBSD system.”
- [118] I. Oxford, “Rapid Clasification of Advanced High Strength Steels using EBSD,” 2020.
- [119] T. N. Lomholt, Y. Adachi, A. Bastos, K. Pantleon, and M. A. J. Somers, “Partial transformation of austenite in Al-Mn-Si TRIP steel upon tensile straining: An in situ EBSD study,” *Mater. Sci. Technol. (United Kingdom)*, vol. 29, no. 11, pp. 1383–1388, 2013.
- [120] K. Zhu, D. Barbier, and T. Iung, “Characterization and quantification methods of complex BCC matrix microstructures in advanced high strength steels,” *J. Mater. Sci.*, vol. 48, no. 1, pp. 413–423, 2013.
- [121] L. E. Samuels, “Light Microscopy of Carbon Steels,” *Light Microsc. Carbon Steels*, 1999.
- [122] K. I. Sugimoto, M. Kobayashi, and S. I. Hashimoto, “Ductility and strain-induced transformation in a high-strength transformation-induced plasticity-aided dual-phase steel,” *Metall. Trans. A, Phys. Metall. Mater. Sci.*, vol. 23 A, no. 11, pp. 3085–3091, 1992.
- [123] N. Saeidi and A. Ekrami, “Comparison of mechanical properties of martensite/ferrite and bainite/ferrite dual phase 4340 steels,” *Mater. Sci. Eng. A*, vol. 523, no. 1–2, pp. 125–129, 2009.

- [124] C. Landron, E. Maire, J. Adrien, and O. Bouaziz, “Damage characterization in dual-phase steels using X-ray tomography,” *Conf. Proc. Soc. Exp. Mech. Ser.*, vol. 5, pp. 11–18, 2011.
- [125] D. Seo, H. Toda, M. Kobayashi, K. Uesugi, A. Takeuchi, and Y. Suzuki, “In situ observation of void nucleation and growth in a steel using X-ray tomography,” *ISIJ Int.*, vol. 55, no. 7, pp. 1474–1482, 2015.
- [126] D. T. Pierce *et al.*, “Quantitative investigation into the influence of temperature on carbide and austenite evolution during partitioning of a quenched and partitioned steel,” *Scr. Mater.*, vol. 121, pp. 5–9, 2016.
- [127] P. R. Rios, “Relationship between non-isothermal transformation curves and isothermal and non-isothermal kinetics,” *Acta Mater.*, vol. 53, no. 18, pp. 4893–4901, 2005.